UNIVERSITY OF CALIFORNIA,
IRVINE

Label-free fluorescence lifetime imaging microscopy (FLIM) to study metabolism and oxidative stress in biological systems

DISSERTATION

submitted in partial satisfaction of the requirements
for the degree of

DOCTOR OF PHILOSOPHY

in Biomedical Engineering

by

Rupsa Datta

Dissertation Committee:
Professor Enrico Gratton, Chair
Associate Professor Eric O. Potma
Assistant Professor Michelle A. Digman

2016

DEDICATION

To

my parents

TABLE OF CONTENTS

LIST OF FIGURES

LIST OF TABLES

ACKNOWLEDGMENTS

I would like to express my sincere gratitude to the committee chair and my advisor Professor Enrico Gratton for his patience, continuous help and support, and his immense knowledge. Enrico's enthusiasm and dedication towards science was a great motivation for me and his encouragement and belief in my abilities lead me on to paths I never imagined I could tread. I had the opportunity to learn from his unique problem solving skills, which applies beyond academia. I am truly grateful to be Enrico's student

I would like to extent my acknowledgement to rest of my committee members Dr. Michelle Digman and Dr. Eric Potma for their insightful comments, guidance and support.

I would like to express my deepest appreciation to Luca Lanzano, my mentor, who took me under his wing when I first joined the Laboratory for Fluorescence Dynamics (LFD) as a clueless graduate student. He was patient, supportive and a great teacher.

LFD has been a unique experience for me and played a great part in shaping who I am today. The lab always had an environment, rich is science and culture. I am thankful to all the LFD members/visitors present, and past. I would like to thank LFD lab manager and my friend Milka Titin for teaching me cell culture and help with sample preparation; Suman Ranjit for valuable discussion in science and general knowledge; Ylenia Santoro for always being encouraging and a great fellow mentor in LFD workshops; Sasha (Alexander Dvornikov) for helping me with imaging on DIVER and sharing his insights on science and life; Hongtao Chen for always being available to fix microscope/electronics related problems and teaching me optics; Christoph Gohlke for maintaining the LFD server and all the data so meticulously; Tracey Scott for helping with the complicated administrative paperwork; Carmine de Rienzo for all the science he taught me, I will always remember him. I have to thank the members of the Digman group, Andrew, Michael and others for making everyday life in the lab more interesting! I would also like to extend my gratitude to the former LFD members Ilaria Altamore, Chiara Stringari, Liz Hinde, Paolo Annibale, Andrea Anzalone, Cosimo Arnesano, Ottavia Golfetto, and Sohail Jahid, an eclectic mix of scientist and great friends. A special thanks to Chi-Li Chiu and Francesco Cutrale for always being encouraging, supportive and just for being there!

I want to take this chance to acknowledge all my collaborators from whom I learned a lot, including Chris Heylman, David Tran and the list goes on. I had the opportunity to collaborate and publish with my friends Arunima Bhattacharjee, Alba Alfonso-Garcia and Aggie Fielder Szymanska which I absolutely enjoyed and am thankful for.

I would like to thank Jenu Chacko for all the help and support, especially through the last two years of my PhD.

And last but not the least my precious parents Dr. Jyotirmoy Datta and Madhumita Datta and my brother Kaustav Datta for all the support and love and for being so near to me even from oceans apart.

CURRICULUM VITAE

Rupsa Datta

EDUCATION

Doctor of Philosophy in Biomedical Engineering **2016**
University of California, Irvine *Irvine, CA, USA*

Master of Biomedical Engineering **2010**
Jadavpur University *Kolkata, India*

Bachelor of Technology in Biomedical Engineering **2008**
West Bengal University of Technology *Kolkata, India*

RESEARCH EXPERIENCE

Graduate Student Researcher **2011-2016**
University of California, Irvine *Irvine, CA, USA*

Master Student Researcher **2010**
Jadavpur University *Kolkata, India*

Undergraduate Student Researcher **2008**
West Bengal University of Technology *Kolkata, India*

PUBLICATIONS

- **Label-free imaging of metabolism and oxidative stress in human induced pluripotent stem cell-derived cardiomyocytes**
  Biomedical Optics Express, 2016

- **Fluorescence lifetime imaging of endogenous biomarker of oxidative stress**
  Scientific Reports, 2015

- **3D microtumors in vitro supported by perfused vascular network**
  Scientific Reports, 2016

- **Metabolic changes associated with methionine stress sensitivity in MDA-MB-468 breast cancer cells**
  Cancer Metabolism, 2016

- **Supervised machine learning for classification of the electrophysiological effects of chronotropic drugs on human induced pluripotent stem cell-derived cardiomyocytes**
  PLoS One, 2015

- **Automated detection and analysis of depolarization events in human cardiomyocytes using MaDEC**
  Computers in Biology and Medicine, 2016

- **Label-free identification of macrophage phenotype by fluorescence lifetime imaging microscopy** Journal of Biomedical Optics, 2016

CONFERENCE PAPERS

- **Label - free fluorescence lifetime imaging of microfluidic device based three-dimensional cardiac tissue metabolism**
  OSA Frontiers in Optics, 2014

- **Advancement in OCT and Image-processing techniques for automated ophthalmic diagnosis**
  IEEE Students' Technology Symposium, Indian Institute of Technology, Kharagpur, 2010

INVITED TALKS AND CONFERENCE ORAL PRESENTATIONS

- **Fluorescence lifetime imaging microscopy to study metabolism in a microfluidic device based tumor microenvironment**
  Oral presentation at Biomedical Optics Congress, Cancer Imaging and Therapy, Fort Lauderdale, FL, 2016

- **Metabolic imaging of tumor microenvironment in a microfluidic device using fluorescence lifetime imaging microscopy**
  Oral presentation at SPIE Photonics Europe, Session- Biophotonics: Photonic Solutions for Better Health Care, Brussels, Belgium, 2016

- **Oxidative stress detection by FLIM**
  10th LFD Workshop in Advanced Fluorescence Imaging and Dynamics, University of California, Irvine, CA, 2015

- **Label–free fluorescence lifetime imaging microscopy (FLIM) of endogenous fluorophore by phasor approach**
  Invited talk at Weekly Summer Research Seminar Series, California State Polytechnic University, Pomona, CA, 2015

- **Endogenous probe for oxidative stress detection by FLIM**
  Oral presentation at Optics in Lifesciences Congress, Vancouver, British Columbia, Canada, 2015

- **Label – free fluorescence lifetime imaging microscopy of endogenous fluorophore**
  Biomedical Engineering Seminar Series - student presentation, University of California, Irvine, CA, 2014

- **FLIM in cardiomyocytes**
  9th LFD Workshop in Advanced Fluorescence Imaging and Dynamics, University of California, Irvine, CA, 2014

CONFERENCE POSTER PRESENTATIONS

- **Intrinsic biomarker for oxidative stress by FLIM**
  60th Annual Meeting of the Biophysical Society, Los Angeles, CA, 2016

- **Label free detection of oxidative stress by fluorescence lifetime imaging microscopy**
  Biomedical Engineering Society Annual Meeting 2015, Tampa, FL, 2015

- **Label - free fluorescence lifetime imaging of microfluidic device based three-dimensional cardiac tissue metabolism**
  Frontiers in Optics, Tuscon, AZ, 2014

- **Metabolic imaging of cardiac tissue model developed in a microfluidic device employing endogenous fluorophore**
  Second international conference on Fluorescent Biomolecules and their Building Blocks: Design and Applications (FB3), La Jolla, CA, 2014

- **Fluorescence lifetime imaging of endogenous fluorophores in iPS derived cardiomyocytes under hypoxia**
  Gordon Research Conference (Lasers in Medicine & Biology), Holderness School, Holderness, NH, 2014

- **Non-invasive optical metabolic imaging of three-dimensional cardiac tissue model in a polydimethylsiloxane microfluidic device**
  15th Annual UC System-wide Bioengineering Symposium, University of California, Irvine, CA, 2014

- **Subcellular level optical metabolic imaging of induced pluripotent stem cells using endogenous fluorophore**
  58th Annual Meeting of the Biophysical Society, San Francisco, CA, 2014

TEACHING AND MENTORSHIP EXPERIENCE

- **Medical Techniques II** Spring 2013
  Teaching assistant for undergraduate course
  Instructor: Dr. Gultekin Gulsen
- **Engineering optics for medical application** Winter 2013
  Teaching assistant for undergraduate and graduate course
  Instructor: Dr. Bruce J. Tromberg
- **LFD Workshop in Advanced Fluorescence Imaging and Dynamics** 2013 - 2015
  Technical instructor for hands on laboratory training in fluorescence lifetime imaging microscopy (3 consecutive years).
- **Undergraduate Student Initiative for Biomedical Research (USIBR) at UC Irvine** 2013 - 2015
  Trained undergraduate and high school students on fluorescence microscopy techniques (3 consecutive years).
- **California State Summer School for Math & Science (COSMOS)** 2013 - 2015
  CLUSTER 7: Clinical Translational Science: The Next Generation of Biomedical Research. Instructor

LEADERSHIP EXPERIENCE

- **Vice President** of Photonics@UCI (OSA & SPIE student chapter at UCI) 2014 - 2016
- **Secretary** of Photonics@UCI (OSA & SPIE student chapter at UCI) 2012 - 2014
- Presented at the OSA Student Leadership Conference, Tucson, AZ. 2014
- Attended SPIE Student Chapter Leadership workshop, Brussels, Belgium 2016

ABSTRACT OF THE DISSERTATION

Label-free fluorescence lifetime imaging microscopy (FLIM) to study metabolism and oxidative stress in biological systems

By

Rupsa Datta

Doctor of Philosophy in Biomedical Engineering

University of California, Irvine, 2016

Professor Enrico Gratton, Chair

Study of cellular metabolism and its influence on physiological functions and pathology along with investigation of oxidative stress in pathogenesis are essential for fundamental biology as well as biomedical research. Optical imaging offers the opportunity to assess these indices non-invasively. In this work we apply two-photon fluorescence lifetime imaging microscopy (FLIM) of intrinsic fluorophores for label-free metabolic and oxidative stress imaging in a wide range of biological samples. Analysis of FLIM data was performed by applying the 'fit-free' phasor approach where each pixel of the image is transformed to its corresponding phasor on the phasor plot. Biological systems are a rich resource of autofluorescent biomolecules. Their fluorescence lifetimes are sensitive to alteration of normal physiology, making them attractive endogenous probes. We discovered one such endogenous fluorophore with characteristic long fluorescent lifetime. We hypothesized these long lifetime species (LLS) to be fluorescent products of lipid oxidation by reactive oxygen species (ROS), rendering them biomarkers of oxidative stress. To correlate the long lifetime species (LLS) with lipid droplets, we performed simultaneous FLIM and two coherent nonlinear

microscopy techniques: third harmonic generation (THG) imaging microscopy and coherent anti-Stokes Raman scattering (CARS) microscopy that are sensitive to lipids. We went one step further to characterize the chemical nature of this discovered species by classical Raman spectral analysis. We show application of this technique in cancer, induced pluripotent stem cell derived cardiomyocytes, as well as in freshly excised mice adipose tissue. The identified endogenous biomarker unfolds opportunities of performing non-invasive measurements of oxidative stress in vivo.

We also exploited the autofluorescent coenzyme reduced nicotinamide adenine dinucleotide (NADH), an endogenous probe extensively used for metabolic imaging. We performed NADH-FLIM to study the metabolic status of a vascularized three-dimensional tumor microenvironment in a microfluidic based platform. We could identify metabolically dissimilar regions, as well as identify metabolic response to anticancer drug.

Finally, we explored NADH-FLIM of a different class of organisms – bacteria. We show for the first time, FLIM-phasor fingerprint of clinically important bacteria. We discovered interesting bacterial phasor trajectories at different growth phases as well as response to antibiotics, all at single cell resolution.

Chapter 1

Introduction

Chapter overview: In this thesis we demonstrate the applications of two-photon fluorescence lifetime imaging microscopy in assessment of metabolism in normal health and pathology, in a wide range of biological samples - 2D cell cultures, fresh tissue as well as tissue engineered microphysiological models. Furthermore, we establish a novel technique for oxidative stress detection employing endogenous fluorophore. This chapter discusses basics of metabolism and oxidative stress and their significance in biomedical research along with current techniques available for their measurement. The chapter concludes with establishing the importance of label-free medical imaging.

1.1 Metabolism and oxidative stress

Research in metabolism has been propelled by the fact that metabolic activity of cells plays a pivotal role in normal cell physiology, influences all cellular functions and dictates cell fate. Its perturbation is associated with human diseases. An increasing number of researches are dedicated to unravel the influences of metabolic pathway in cell growth, proliferation, cell differentiation and cell death. Metabolism involves several biochemical pathways catalyzed by a sequence of enzymes which results in either consumption or production of energy. The core metabolic pathways can be divided into three main groups[1]:

Anabolism – synthesis of small molecules and their polymerization into complex macromolecules. These processes require energy.

Catabolism – degradation of large molecules (polysaccharides, lipids, nucleic acids and proteins) into smaller subunits (monosaccharides, fatty acids, nucleotides, and amino acids) with the release of energy.

Toxic waste removal

While metabolism encompasses myriad of complex biochemical pathways, oxidative phosphorylation, anaerobic glycolysis, and aerobic glycolysis (Warburg effect) are three important processes of cellular respiration (Fig 1.1). Mature, differentiated cells metabolize glucose to pyruvate through glycolysis in the cytosol. Subsequently, in presence of oxygen, pyruvate is decarboxylated to produce acetyl-CoA in the mitochondrial matrix which then enters the Krebs cycle. Reduced nicotinamide adenine dinucleotide (NADH) and reduced flavin adenine dinucleotide ($FADH_2$) created in all the above steps donate electrons to the electron transport chain (ETC) and this oxidative phosphorylation produces energy. Oxygen is the final electron acceptor in this pathway and hence is an essential metabolite. Oxidative phosphorylation also produces reactive oxygen species (ROS). During scarcity of oxygen, the cells might shift to anaerobic glycolysis where pyruvate is converted to lactate. The adenosine triphosphate (ATP) generated by anaerobic glycolysis is significantly lower than oxidative phosphorylation and hence is less efficient in ATP production. Highly proliferating cancer cells perform aerobic glycolysis, that is, glycose is converted to lactate even in presence of oxygen. This process, also known as the 'Warburg effect', is also less efficient in ATP production in comparison to oxidative phosphorylation[2,3].

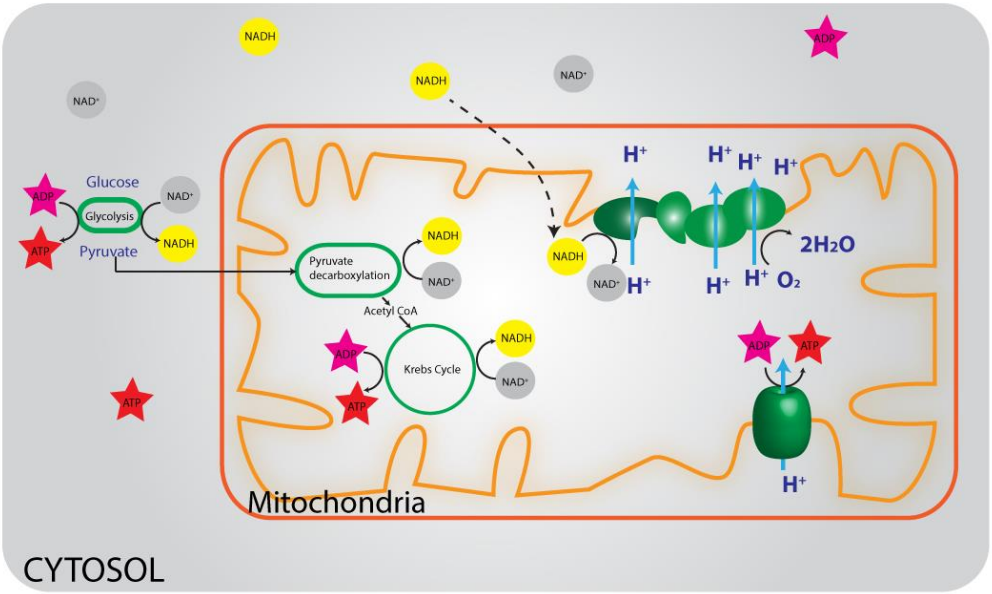

Fig 1.1 Simplified schematic of glucose metabolism

Although the basic players of metabolism like ATP, acetyl-CoA, NADH, and reduced nicotinamide adenine dinucleotide phosphate (NADPH) are universal among all mammalian cells, their metabolic activity are dependent on the microenvironment (for example, availability of nutrients, oxygen gradient) and physiological function of the tissue[4]. For example, mature cardiomyocytes have a high ATP demand and hence they employ oxidative phosphorylation for efficient ATP generation[5]. On the other hand, embryonic stem cells (ESCs) show high glycolytic rates, and highly proliferative cancer cells show aerobic glycolysis even in presence of oxygen[2,6].

Metabolic alteration is considered as one of the hallmarks of cancer along with others such as sustained proliferative signals, ability to evade growth suppressors, immune evasion, promotion of inflammation, replicative immortality, increased motility, metastatic ability, angiogenic potential, increased genomic instability, resistance to cell death' [7,8]. Hence study of cancer metabolism yields powerful insights into disease development.

Another closely related phenomena that has been implicated in a wide range of diseases is oxidative stress. These include inflammation, diabetes mellitus, cancer, atherosclerosis, other cardiovascular diseases, and numerous neurodegenerative disease[9]. Furthermore, oxidative stress has been linked to the process of aging[10]. As mentioned previously, ROS are created as byproducts of aerobic respiration. These are small molecules derived from oxygen including superoxide radical ($O_2^{\bullet -}$), hydrogen peroxide (H_2O_2), hydroxyl radicals ($OH\bullet$) and so on. At physiological levels, ROS are involved in intracellular signaling pathways, inflammatory response generation, and redox regulation[11–13]. However, these species are highly reactive and when present in excess amount can cause oxidative damages to biomacromolecules leading to oxidative stress.

Hence understanding cellular metabolism, its regulation, and its influence on normal and pathological cell physiology coupled with investigation of oxidative stress in pathogenesis of these human disease takes an important place biomedical research.

1.2 Techniques to study metabolism and oxidative stress

The close relationship of metabolism and oxidative stress and their link to pathology has led to wide variety research techniques that are currently used to comprehend and study these indices. Analytical biochemistry approach include several "omics"-based strategies[7]. Metabolomics entails comprehensive study of metabolites that are present in the biological sample of interest like tissue or cell extract, culture media or biofluids. This can be accomplished through the use of techniques like NMR spectroscopy and mass spectrometry coupled with chromatography techniques including high performance liquid chromatography (HPLC), ultra performance liquid chromatography (UPLC), gas

chromatography (GC) or capillary electrophoresis (CE) followed by multivariate statistical analysis for pattern-recognition and biological interpretation[14] . Other spectroscopic tools employed for metabolomics include Fourier-transform infrared (FT-IR) spectrometry, Raman spectroscopy, metabolite arrays and thin- layer chromatograph (TLC)[15]. However, these techniques produce bulk measurements and hence do not allow assessment of metabolic activity at single cell level. Also, most of these methods are invasive. Non-invasive and partially invasive metabolic imaging have also been explored. Some of them include auto radiography to study metabolite 2-deoxyglucose and positron emission tomography (PET) scanning to study Fluorodeoxyglucose (FDG-PET). FDG-PET has been employed in clinical diagnostic imaging of various kinds of tumors[2,16,17]. Some studies reported use of 4-fluoro-glutamines PET for metabolic imaging[18]. Magnetic resonance (MR) spectroscopy employing nuclei like 1H, 13C, 31P, and 19F is also used for metabolic imaging[19]. Potential limitation of these techniques is the requirement of radiolabeling. Analysis of extracellular flux to measure oxygen consumption rate (OCR) and extracellular acidification rate (ECAR) to evaluate mitochondrial respiration and glycolysis respectively using the Seahorse technology has been gaining popularity over the past decade[20,21]. However, these techniques analyze the media over monolayer of cells or extracted tissue within a microplate, thus lacking in spatial information and cannot be translated to *in vivo* measurements.

Detecting ROS itself is a direct measure for identifying the presence of oxidative stress. Due to their high reactivity and instability, very low steady-state concentrations (picomolar or very low nanomolar)[22] of ROS exists in biological systems. Hence ROS measurement requires rapid interaction of sensors and the species. Indirect techniques for detecting ROS utilize the more stable ROS oxidation products. These identify damage to biomolecules by ROS or

quantify levels of antioxidants or redox molecules. Substantial progress has been achieved in developing techniques to detect ROS. These include chemiluminescent imaging with probes like L-012, an analog of luminol or chemiluminescent nanoparticles[23,24]. Imaging oxidative stress by electron paramagnetic resonance (EPR) requires injection of redox-sensitive spin probes like nitroxide which is reduced to EPR-silent hydroxylamine by ROS, causing a decrease in EPR signal[25,26]. Not only does this technique require administration of an external agent, the data interpretation can be difficult as decrease in EPR signal can also be attributed to removal of the probe due to absorption into tissues, or excretion through kidney or liver. PET/SPECT in vivo imaging techniques have also been employed to indirectly detect oxidative stress by using radiotracers to image correlated events like consumption of glucose and radiotracers that bind to ROS scavengers or mitochondrial complexes[26].

Optical imaging using exogenous fluorophores have also been employed to study metabolic activity and ROS. Small molecule fluorescent indicators of reactive oxygen species (ROS) include 2′-7′- dichlorodihydrofluorescein (DCFH), dihydroethidium (DHE), and mitochondrial-targeted DHE (mitoSOX)[27]. These probes are usually nonspecific and compete with antioxidant systems to get oxidized by endogenous ROS. This oxidation results in a fluorescent product which can be detected by fluorescence microscopy. However, potential limitation of these probes are the possibility of them reacting with other biological oxidizing or reducing agents. Also the reactions with ROS might produce intermediate probe radicals. Further, additional ROS might be generated. For example, one of the popular ROS probe DCSF is oxidized to 2′-7′-dichlorofluorescein (DCF) which if fluorescent. However, cytochrome c and heme peroxidases could also bring about DCFH oxidation. Moreover, DCF radical can react with oxygen to produce $O_2^{\bullet -}$ and subsequently H_2O_2[27].

Another class of optical probes consist of genetically encoded fluorescent proteins for metabolic biosensing and ROS detection. Hung et al. created a circularly permuted fluorescent proteins (cpFPs), Peredox, is a biosensor for cytosolic NADH-NAD+ redox ratio in mammalian cells[28]. Other FPs include reduction-oxidation-sensitive green fluorescent proteins (roGFPs) for redox potential measurement[29], mitochondrially targeted circularly permuted fluorescent proteins (mt-cpYFP) for superoxide flashes[30], circularly permuted yellow fluorescent protein (cpYFP) HyPer, HyPer-3, and roGFP2-Orp1 to detect H_2O_2[31] and recently reported sensors for NADP+ (Venus-tagged Apollo- $NADP^+$)[32] and mitochondrial NAD^+[33] . However, these require creation of specific gene constructs, transfection of these constructs into cells or creating transgenic mice for study in metabolic and ROS imaging of tissue. Also the genetically encoded proteins might alter the redox homeostasis.

In this work we apply label-free optical microscopy techniques to assess metabolism and oxidative stress in a wide range of biological samples. Optical imaging provides the opportunity to non-invasively probe living samples without perturbing the natural physiology.

1.3 Label free fluorescence imaging

Biological systems are a rich resource of endogenous fluorophores that are extensively employed to study and assess physiological functions like metabolism in a convenient and label-free manner. The emission properties of these intrinsic biomolecules are often influenced by their microenvironment, morphology, metabolic state and pathological conditions of the cells or tissue, hence rendering them powerful biomarkers. Some of the significant intrinsic fluorophores with their one photon excitation and emission wavelengths

have been listed in table 1.1. One of the earliest employed intrinsic fluorophores to assess tissue health was porphyrins, vitamins and lipofuscins. However, after the seminal research by Chance et al., NADH fluorescence has been widely used to study metabolism both in vitro and in vivo[34,35]. The advantage of employing endogenous fluorophores to probe biological systems is its non-invasiveness. Use of intrinsic fluorophores avoids administration of external fluorescent dyes, thus circumventing associated nonspecific binding, toxicity, and interference with the biochemical and physiological functions of the biological system being imaged. Furthermore, the technique can be translated to in vivo monitoring of pathological condition and fast clinical diagnosis.

Table 1.1 Spectral characteristics of endogenous fluorophores

Endogenous fluorophore	Excitation(nm)	Emission (nm)	Reference
Metabolic coenzymes			
NADH	340 (max)	470 (max)	Scott et al[36]
NADPH	336 (max)	464 (max)	Ramanujam[37]
FAD,flavin	450 (max)	535 (max)	Ramanujam[37]
Flavin mononucleotide (FMN)	444 (max)	558 (max)	Leenders et al.[38]
Structural proteins			
Collagen	325,360 (max)	400, 405 (max)	Ramanujam[37]
Elastin	290, 325 (max)	340, 400 (max)	Ramanujam[37]
Vitamins			
retinol	327 (max)	510 (max)	Ramanujam[37]
riboflavin	420-500	520 -750	Berezin et al[39]
Vitamin K	335 (max)	480 (max)	Ramanujam[37]
Vitamin D	390 (max)	480 (max)	Ramanujam[37]
Vitamin B12	275 (max)	305 (max)	Ramanujam[37]
Pigments			
Melanin	300 -800	440,520,575	Berezin et al[39]
Eumelanin	355	520	Chorvatova[40]
Phorphyrins	400-450	630,690	Ramanujam[37]
Lipofuscin	340 - 395	540, 430 - 460	Berezin et al[39]
Bilirubin	350–520	480–650	Zucker et al[41]
Amino acids			
phenylalanine	258 (max) 240-270	280 (max)	Berezin et al[39]
tryptophan	280 (max)	250 - 310	Berezin et al[39]
tyrosine	275 (max)	300 (max)	Berezin et al[39]

1.4 NADH, a biomarker for metabolic imaging

Nicotinamide adenine dinucleotide (NAD) is a metabolic coenzyme that plays a myriad of roles in cellular oxidation and reduction reactions. The reduced form NADH and oxidized form NAD+ takes part in mitochondrial function, energy metabolism, calcium homeostasis, gene expression, oxidative stress, aging and apoptosis. The reduced NADH phosphate (NADPH) is associated with reductive fatty acid biosynthesis and steroids, oxidative stress, anti-oxidation and the oxidized form, NADP+, is involved with calcium homeostasis[42]. Real time monitoring cellular metabolism during pathophysiological changes is possible by of the measuring the redox ratio (NADH:NAD+). NADH is the principal electron acceptor in glycolysis which results in two NADH molecules per glucose molecule. Subsequently pyruvate is decarboxylation and Kerbs cycle also reduces NAD+ to NADH molecules. During oxidative phosphorylation, it is oxidized to NAD+ by donating electrons to the electron transport chain, which are ultimately accepted by oxygen[42,43]. In the case of anaerobic glycolysis, NAD+ is converted to NADH and oxidative phosphorylation is diminished. This decreases the oxidation of NADH, resulting in an overall increase of free NADH. Thus, the reduction-oxidation pair NADH:NAD+ serves as an indicator of balance between oxidative phosphorylation and glycolysis. Bird, et al. demonstrated a correlation between the redox ratio NADH:NAD+ and the ratio of free to protein bound NADH, which is advantageous in fluorescent based technique because unlike NADH, NAD+ is not fluorescent[44]

On the basis of the pivotal role of NADH in cell biology and metabolism, it has the potential to be employed as an endogenous biomarker for cellular redox reactions, energy metabolism and mitochondrial anomalies under different pathophysiological conditions. The most

important property of NADH that makes it an attractive biomarker in optical imaging is its autofluorescence with absorption maximum of 340nm and emission maximum of 470nm[36]. More importantly, its fluorescence is affected by local environment and protein binding which is dependent on metabolism. This allows non-invasive metabolic imaging of cells and tissue in their native physiological environment avoiding perturbation of the biological system.

Early work on use NADH fluorescence in bioscience and its link to metabolism were conducted by Chance and his collaborators. In 1956 Boyer and Theorell showed that the intensity of fluorescence NADH (then referred to as diphosphopyridine nucleotide, DPNH) increased when it binds to liver alcohol dehydrogenase[45]. Further, the fluorescence emission maxima wavelength decreased upon this combination. Similar spectral blue shifts were also observed upon binding with yeast alcohol dehydrogenase, lactic dehydrogenase, beef liver glutamic dehydrogenase and lactate dehydrogenase[36,46]. Using this difference in spectroscopic properties, correlation between mitochondrial metabolic states and NADH redox states were established using spectral fluorometric study of isolated rat liver[35,47]. These preliminary studies showed association of bound NADH to the mitochondrial respiratory chain. The first in vivo monitoring of NADH in kidney and brain of anesthetized rat, employing two microfluorometers simultaneously was reported by Chance et al in 1962[48]. This study showed increase in NADH fluorescence indicating increase of free NADH when the animals were respiring nitrogen and carbon monoxide (anoxia) or when treated with respiratory inhibitors like hydrogen sulphide.

Following these initial results, endogenous NADH fluorescence has been used extensively to study metabolism. Combination of NADH and FAD fluorescence intensity in form of the redox ratio FAD/(NADH+FAD) had been proposed in late 1960s[49]. This ratiometric approach, where an increase in the ratio indicated lower metabolic activity, has also been widely employed to explore metabolic activity[50–54].

In this work we exploit the fluorescence lifetime properties of NADH for metabolic imaging. Free NADH exists in a folded configuration [Fig 1.2(a)]. This causes quenching of the reduced nicotinamide (which is the fluorescent group) by the adenine group. On the contrary, upon binding to proteins, NADH is in extended configuration as shown in [Fig 1.2 (b)], causing this quenching to decrease. Fig 1.2 (c) shows schematic diagram of NADH in open configuration when bound to L-lactate dehydrogenase of *trichomonas vaginalis*. Due to this self-quenching, the lifetime of free NADH is significantly lower (~0.4ns) compared to protein bound NADH[36,55]. For example, the lifetime of NADH bound to lactate dehydrogenase (LDH) is 3.4ns[9,56]. Hence the two forms can be distinguished by fluorescence lifetime imaging microscopy (FLIM). FLIM of autofluorescent NADH can serve as a powerful tool to study metabolism due to the extreme sensitivity of fluorescence lifetime to molecular conformations and the fluorophore's surrounding environment. Also, unlike intensity based imaging, lifetime measurements are independent of concentration. Hence, NADH FLIM is extensively employed as an endogenous biomarker for metabolic imaging in cancer, stem cell differentiation and so on [42–44,56–60].

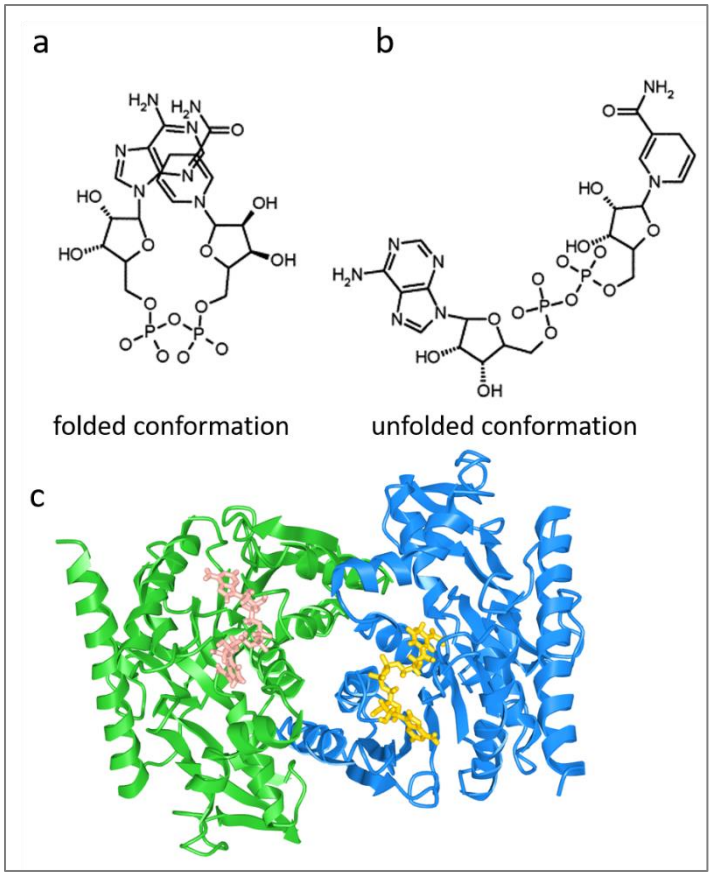

Fig 1.2 NADH conformations. (a) folded conformation of NADH as it eminently exists in free state. (b) extended conformation of NADH. a and b are adopted from Hull et al (c) Schematic diagram showing chain A of L-lactate dehydrogenase of Trichomonas vaginalis (green ribbon) in complex with NADH (pink stick representation) and chain B of L-lactate dehydrogenase (blue ribbon) in complex with NADH (yellow stick representation). 'c' was created using iCn3D web-based software (www.ncbi.nlm.nih.gov)

1.5 Chapter Summary

In this thesis, two-photon fluorescence lifetime imaging microscopy (FLIM) was employed for metabolic imaging and detection of oxidative stress in a wide range of biological samples. In this chapter we briefly introduce the basics of cell metabolism and oxidative stress. We establish the motivation to study these parameters by discussing their significance in regulating normal physiology and pathogenesis. Next we consider some of the alternative techniques currently employed for metabolism and oxidative stress measurements and their shortcomings. We also introduce the importance of label-free imaging and enlist some endogenous fluorophores currently employed as biomarkers of different physiological functions. We conclude the chapter by discussing autofluorescence of an important metabolic coenzyme reduced nicotinamide adenine dinucleotide (NADH) which will be employed extensively as a biomarker for label free metabolic imaging throughout the work presented in this thesis.

Chapter 2

Methods

Chapter overview: In this thesis we exploit frequency domain fluorescence lifetime imaging microscopy (FLIM) of endogenous fluorophores as a powerful biomedical optics tool. This chapter serves to briefly explain the theory behind FLIM technique employed for the work presented in this thesis. Further, this chapter also includes detailed explanation of the phasor approach to FLIM data analysis and interpretation. In certain projects, we have also employed additional optical microscopy techniques like third harmonic generation, CARS (Coherent Anti-Stokes Raman Scattering) microscopy and so on, details of which will be explained in the 'Materials and methods' section of the respective chapters.

2.1 Fluorescence lifetime and its measurement

When a fluorophore is excited by a short pulse of light, its fluorescence lifetime (τ) is the time it takes for the intensity, $I(t)$, to decrease to $1/e$ or 36.8% of original value (Fig 2.1). The intensity at time t is given by:

$$I(t) = \alpha e^{-t/\tau} \quad (1)$$

where, α is the pre-exponential factor.

In case of a population of excited fluorophores, the fluorescence lifetime is the time it takes for the number of excited molecules, $n^*(t)$, to decrease to $1/e$ or 36.8% of original population $n^*(0)$. The number of excited molecules at a time t is given by:

$$n^*(t) = n^*(0)e^{-t/\tau} \quad (2)$$

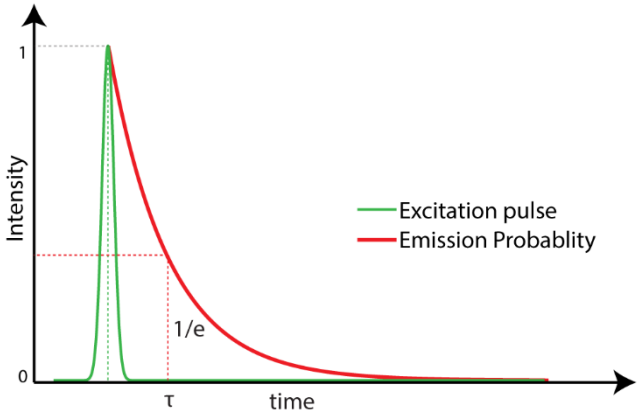

Fig 2.1 Schematic of excitation, single exponential fluorescence decay curve and lifetime

If the decay is single exponential, it can be described by equation (1). However, if the decay is multi-exponential, the decay equation takes the form

$$I(t) = \sum_i \alpha_i \, e^{-t/\tau_i} \tag{3}$$

For example, if a decay has two lifetimes, it can be expressed as:

$$I(t) = \alpha_1 e^{-t/\tau_1} + \alpha_2 e^{-t/\tau_2} \tag{4}$$

From the days of its inception, two alternative methods for fluorescence lifetime measurement have been employed – the frequency domain method and time domain method[61–66]. Detailed explanation of the techniques is beyond the scope of this thesis. Very briefly, in time domain method, the sample is illuminated by a short pulse of light (short relative to the lifetime (τ) of the fluorophore) and the corresponding intensity decay is measured. The fluorescence lifetime can be calculated from the amount of time the signal decreases to $1/e$ of its initial value, i.e., at time t=0. Currently, time-correlated single-photon counting (TCSPC) technique is largely employed for time domain measurement which involves construction of photon delay histogram. [64,66–69].

In this work, we employed the frequency domain method for fluorescence lifetime measurement. This technique, also referred to as phase-modulation domain, dates back to 1926 when, for the first time, lifetime was measured by Gaviola[70]. Venetta in 1959 demonstrated lifetime measurement by coupling a phase fluorometer to a microscope, one of the seminal works leading to the present day fluorescence lifetime imaging microscopy (FLIM)[71].

In frequency domain method, the sample is excited by a modulated light source at high frequencies and the harmonic response of the system is measured. The equation of this modulated excitation signal for a given frequency of modulation can be written as:

$$E(t) = E(0)[1 + M_E \sin(\omega t)] \quad (5)$$

where $E(t)$ is intensity at time t and $E(0)$ is intensity at time 0. M_E is the excitation modulation factor and ω is the angular frequency and is given by $\omega = 2\pi f$, f is the linear modulation frequency.

With a sinusoidally modulated excitation, the emission signal will also be modulated sinusoidally[63,66]. However, emission signal will be phase shifted with respect to the excitation due to delay between absorption and emission. Also, the peak to peak amplitude of the emission will be decreased. This can be written as[66]:

$$F(t) = F(0)[1 + M_F \sin(\omega t + \phi)] \quad (6)$$

where $F(t)$ is the fluorescence intensity at time t and $F(0)$ is that at time $t = 0$. M_F is the emission modulation factor and ϕ is the phase delay between excitation and emission. The

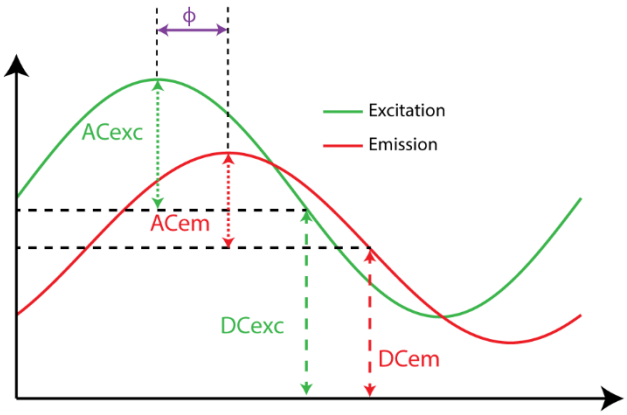

Fig 2.2 Schematic diagram of sinusoidally modulate excitation and the resulting phase shifted emission signal in frequency domain measurement. The AC and DC components of each signal are also indicated.

modulation and phase shift of the emission is dependent on relative values of frequency of modulation, f, and lifetime τ.

In case of single exponential decays, we can obtain the phase lifetime (τ_P) as the following:

$$\tan\phi = \omega\tau_P \tag{7}$$

The modulation factors can be expressed as the ratio of AC to DC components of the respective signals (Fig 2.2):

$$M_E = \frac{AC_{EX}}{DC_{EX}} \qquad M_F = \frac{AC_{EM}}{DC_{EM}} \tag{8}$$

From this, we can estimate the relative modulation M as:

$$M = \frac{AC_{EM}}{DC_{EM}} \Big/ \frac{AC_{EX}}{DC_{EX}} \tag{9}$$

The relative modulation (M) and modulation lifetime (τ_M) are related as:

$$M = \frac{1}{\sqrt{1+(\omega\tau_M)^2}} \tag{10}$$

In case of a single exponential decay, lifetimes from phase and relative modulation are equal, i.e., $\tau_P = \tau_M$ for all ω, However, for a multi-exponential decay, $\tau_P < \tau_M$ and will depend on modulation frequency[72]. Usually phase measurements are more preferred than modulation.

The modulation frequency used for the measurement should be chosen by keeping in mind the lifetime scale of fluorophore being measured. Having the angular modulation frequency set to roughly the inverse of the lifetime (i.e., $\omega\tau = 1$) gives maximum sensitivity. Linear modulation frequencies in the order of 100MHz to 1GHz, gives picoseconds temporal resolution appropriate for fluorescence lifetime measurement. In this work frequency of 80MHz is used. Instead of a sinusoidally intensity modulated source, a pulse source can be employed that according to Fourier theory, is equivalent to a sum of sinusoids.

Since the modulation frequencies are very high, it is technically difficult to measure the phase shifts and demodulations directly[73]. For frequency domain fluorescence lifetime detection, we employed the FLIMbox coupled with laser scanning microscope[61,74,75]. This detection scheme has undergone a massive advancement, the details of which are once again outside the scope of this thesis. Following is a brief retrace of FLIMbox development. One of the earlier methods used was the analog frequency domain detection which was advantageous in case of heterogeneous sample with multi-exponential decays[72]. This was pursued by cross-correlation or heterodyning scheme of frequency domain detection as described by Spencer and Weber and entails modulation of detector (photomultiplier tube) gain with a frequency close by not equal to the frequency of laser modulation[61,63,72]. This low frequency signal at the detector carrying the phase and modulation information of the original signal can be digitized and subsequently analyzed using Fourier Transformation (FT)[63,73]. Moving

forward from analog to digital frequency domain detection, the first parallel multifrequency fluorometer was described in 1989 where pulsed light source was employed[76]. Further, the detector gain was modulated by a pulse rather than a sinusoid. In 2007, the digital frequency domain FLIM (DFD-FLIM) system or the First FLIMbox for FLIM was implemented at the Laboratory for Fluorescence Dynamics (LFD) in 2007 which employed a field programmable gate array (FPGA) chip for digital heterodyning[61,75,77]. This was followed by the Parallel digital frequency FLIMbox construction (2009)[61]. In this digital frequency domain lifetime measurement, instead of modulating the detector gain, the analog signal is digitally modulated by data collection circuitry. The FLIMbox creates photon counting phase histograms where the laser repetition rate is divided into a number of phase intervals (for example 256) and the arriving photons are phase tagged[74]. The photons representing the lifetime decay are spread among these phase bins and are efficiently collected. This increases the time resolution which essentially depends on the photons collected[61].

2.2 Phasor Approach to Fluorescence Lifetime Imaging Microscopy (FLIM)

2.2.1 Advantage of the phasor analysis

Fluorescence lifetime data, especially while measuring intrinsic fluorescence from heterogeneous samples like cells or tissue are often very complex and the decay profiles are no longer single exponentials. Moreover, for time domain measurements, the intensity decay is convolved with the instrument response function (IRF). For such data analysis the IRF is deconvolved from the measured decay using methods like non-linear least square followed single exponential function or multi-component exponential fitting[39,53,57,64,67]. Some alternative data analysis techniques reported include Laplace transform method, global

fitting algorithm by image segmentation or stretched exponential fitting and Laguerre deconvolution technique have also been suggested[78–81]. All these approaches, however, become more complicated in heterogeneous samples with multiexponential decay. Also, calculation of the decay lifetime at each individual pixel of a FLIM image further increases the complexity and tend to be computationally expensive. In this work, we employ the phasor approach to FLIM which circumvents all these problems by avoiding fitting of the measurements[82,83]. Importantly, it works on the unbiased raw data without any approximation. The method does not require a priori knowledge of the sample being imaged and gives instantaneous results. By this method, we can obtain decay information at each pixel of the image. If a single pixel contains more than one fluorescent molecular species, these can be easily identified. Another benefit of the phasor approach is the instantaneous visualization of the spatial location of the identified molecular species in the image.

Fluorescence lifetime analysis by phasor approach was first introduced for single point measurements in 1984[84]. More than a decade later it was implemented for the analysis of heterogeneous multi-exponential systems[85,86]. In 2008, phasor approach was applied to FLIM and the concept of phasor fingerprinting of molecular species on the phasor plot was introduced along with creation of FLIM map[82].

Following this, FLIM-phasor analysis has been successfully employed to study autofluorescence, FLIM-FRET analysis, polarity and dipolar relaxation effects of laurdan and so on[83,87–93]. Recently phasor approach was exploited beyond FLIM[94,95].

2.2.2 The phasor transformation

In the phasor analysis, the fluorescence decay information each pixel in the FLIM image is transformed into a point in the phasor plot[82]. The 2-D histogram of the phasors is plotted on the phasor plot to create the phasor distribution of the image. This allows analysis of different lifetime phasor clusters which can be can be mapped back onto the image to create the FLIM map.

This method of analysis can be applied to both time domain and frequency domain FLIM measurements. Let $P(i,j)$ be a pixel in the FLIM image with coordinates (i,j). Let $I_{i,j}(t)$ be the fluorescence intensity decay at that pixel. In case of time-domain, the corresponding coordinates in the phasor plot (g, s) is given by[89]:

$$g_{i,j}(\omega) = \frac{\int_0^T I_{i,j}(t)\cos(\omega t)dt}{\int_0^T I_{i,j}(t)dt} \tag{11}$$

$$s_{i,j}(\omega) = \frac{\int_0^T I_{i,j}(t)\sin(\omega t)dt}{\int_0^T I_{i,j}(t)dt} \tag{12}$$

where $\omega = 2\pi f$, and $f = 1/T$ is the laser repetition rate. $f = 80MHz$ in our case.

In case of frequency domain measurement, the coordinates are given by:

$$g_{i,j}(\omega) = \mathrm{M_{i,j}}\cos(\phi_{\mathrm{i,j}}) \tag{13}$$

$$s_{i,j}(\omega) = \mathrm{M_{i,j}}\sin(\phi_{\mathrm{i,j}}) \tag{14}$$

where relative modulation $\mathrm{M_{i,j}}$ is the modulation and $\phi_{\mathrm{i,j}}$ is the phase shift of the emission signal with respect to the excitation, at pixel $P(i,j)$. The phasor coordinates can also be

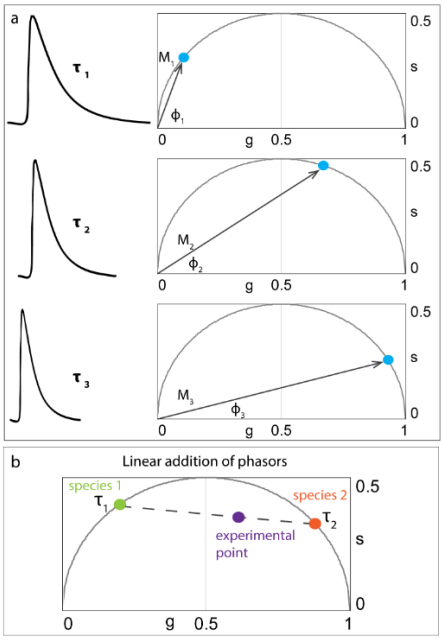

Fig 2.3 The phasor transformation. (a) Schematic representation to showing the shift of phasor along the universal circle with changes in single exponential lifetime. In this representation $\boldsymbol{\tau_1} > \boldsymbol{\tau_2} > \boldsymbol{\tau_3}$. Longer lifetime falls near the coordinates (0, 1) while shorter are nearer to (0, 0). (b) Rule of linear addition of phasors

expressed in term of lifetime and angular laser repetition frequency. In the case of single exponential decay the g and s coordinates are given by the equations:

$$g_{i,j}(\omega) = \frac{1}{1+(\omega\tau)^2} \tag{15}$$

$$s_{i,j}(\omega) = \frac{\omega\tau}{1+(\omega\tau)^2} \tag{16}$$

From the equations of phasor coordinates, (g, s), i.e., equations (15) and (16), we can derive:

$$s_{i,j}{}^2 + (g_{i,j} - {}^1/_2)^2 = {}^1/_4 \tag{17}$$

From this equation, we can deduce that all single exponential lifetimes will fall on a semi-circle of radius ${}^1/_2$ and center $({}^1/_2, 0)$. Since all possible single exponentials lie on this circle, it is referred to as the *Universal Circle.* A short lifetime having smaller phase will lie near the

point (1,0) which corresponds to $\tau = 0$, while a long lifetime will fall on the Universal circle coordinates (0,0) which corresponds to $\tau = \infty$. This has been schematically shown in Fig 2.3(a).

If a pixel in the FLIM image consists of multiple single lifetime components in, the phasor coordinates are given by:

$$g_{i,j}(\omega) = \sum_k \frac{h_k}{1+(\omega\tau_k)^2} \tag{18}$$

$$s_{i,j}(\omega) = \sum_k \frac{h_k \omega\tau_k}{1+(\omega\tau_k)^2} \tag{19}$$

where h_k is the intensity weighted fractional contribution of the single-exponential component with lifetime τ_k. The location of phasor of a system with multiple single exponential species will be the intensity – weighted average of contribution of each single exponential species, that would individually fall on the Universal circle. Another important feature of phasor is the rule of linear addition and is represented in Fig 2.3 (b). The phasor of a system of mixtures of two different pure single exponential species will fall on a straight line joining the phasor location of the individual species on the semicircle[82,86]. The phasor distribution of possible linear mixture of the two chemical species (species 1 and 2 in Fig 2.3 (b)) will fall along the line connecting the two components, the positions of which will be determined by the relative fractional contributions. Hence the phasor of a heterogeneous sample will have a position inside the Universal circle.

In a biological system like tissue which contains a number of fluorescent molecules, the phasor will be given by sum of each individual phasor component (g_n, s_n) weighted by their respective fractional contribution (f_n). The overall coordinates in this case is given by:

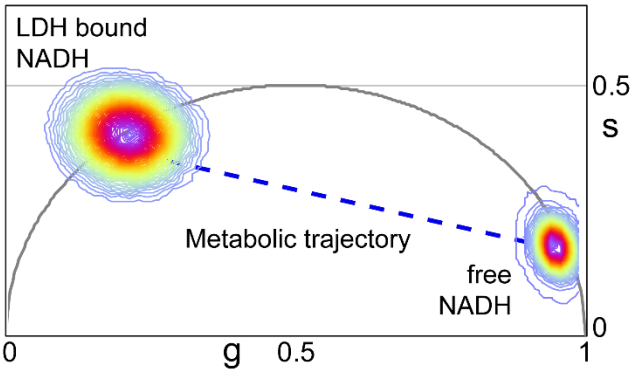

Fig 2.4 Phasor fingerprint position of free NADH (~0.38ns) and lactate dehydrogenase bound NADH (~3.4ns) with laser repetition rate of 80MHz. The line joining these position is referred to as the metabolic trajectory (blue dashed line).

$$G(\omega) = \sum_n f_n g_n(\omega) \tag{20}$$

$$S(\omega) = \sum_n f_n s_n(\omega) \tag{21}$$

2.3 NADH FLIM phasor

One of the prominent applications of the phasor approach that has been employed in this thesis is analysis of NADH FLIM. Fig 2.4 shows the phasor positions of free and enzyme lactate dehydrogenase (LDH) bound NADH that falls close to the universal circle. Any possible mixture of these decays will fall in the line joining these two phasors. This has been referred to as the metabolic trajectory by Stringari et al. and the free/bound NADH ratio decrease linearly along this line from the position of 100% free NADH to 100% bound NADH (Fig 2.4)[96]. Biological samples like cells and tissues contain different mixtures of free and bound form of NADH, depending on the location inside the cell (cytoplasm vs. nucleus) and the metabolic state of the cell. If we analyze the NADH FLIM data from such a sample using the phasor approach, it would result in phasors distributed along the line joining the pure single exponentials. From this plot we can identify fraction of free and bound NADH ratio in

our sample. By mapping the phasor points back onto the image, we can create an NADH distribution map.

NADH FLIM phasor technique have been previously employed for metabolic imaging of human embryonic stem cell, neural stem cell differentiation and progenitor stem cells[58,89,97]. NADH free/bound ratio in the nucleus in myoblast cell line have been also probed[97]. Along with monolayer cell culture sample, the NADH FLIM phasor have been extended to live tissue imaging, including live mice. These include metabolic fingerprinting of small intestine crypts, and detection of metabolic oscillation following circadian rhythm in epidermal basal layer stem cell[96,98]. Pate et al. employed NADH FLIM phasor to discover reduction of colon cancer cell glycolytic metabolism upon interference of Wnt signaling, an important pathway in tumorigenesis[99].

2.4 FLIM map representation

In this thesis we have used two FLIM map representation – the cursor selection method and the pseudo-colorscale. Both are essentially the same concept but have different visual impact. In the cursor selection method, the FLIM map is created by placing circular or square cursors on the phasor plot. The idea is to select the phasor cluster of interest with the cursor [Fig 2.5(a)]. The pixels in the image that have their phasor inside the cursor will be color coded to match the color of the cursor. Multiple cursors can be used to select multiple phasor clusters within the phasor plot, thus allowing visualization of spatial locations of these selections. The size and placement position of the cursors depends on the specific phasor distribution being analyzed. Furthermore, for quantitative analysis, the fraction of pixels in an image within a specific cursor can be calculated.

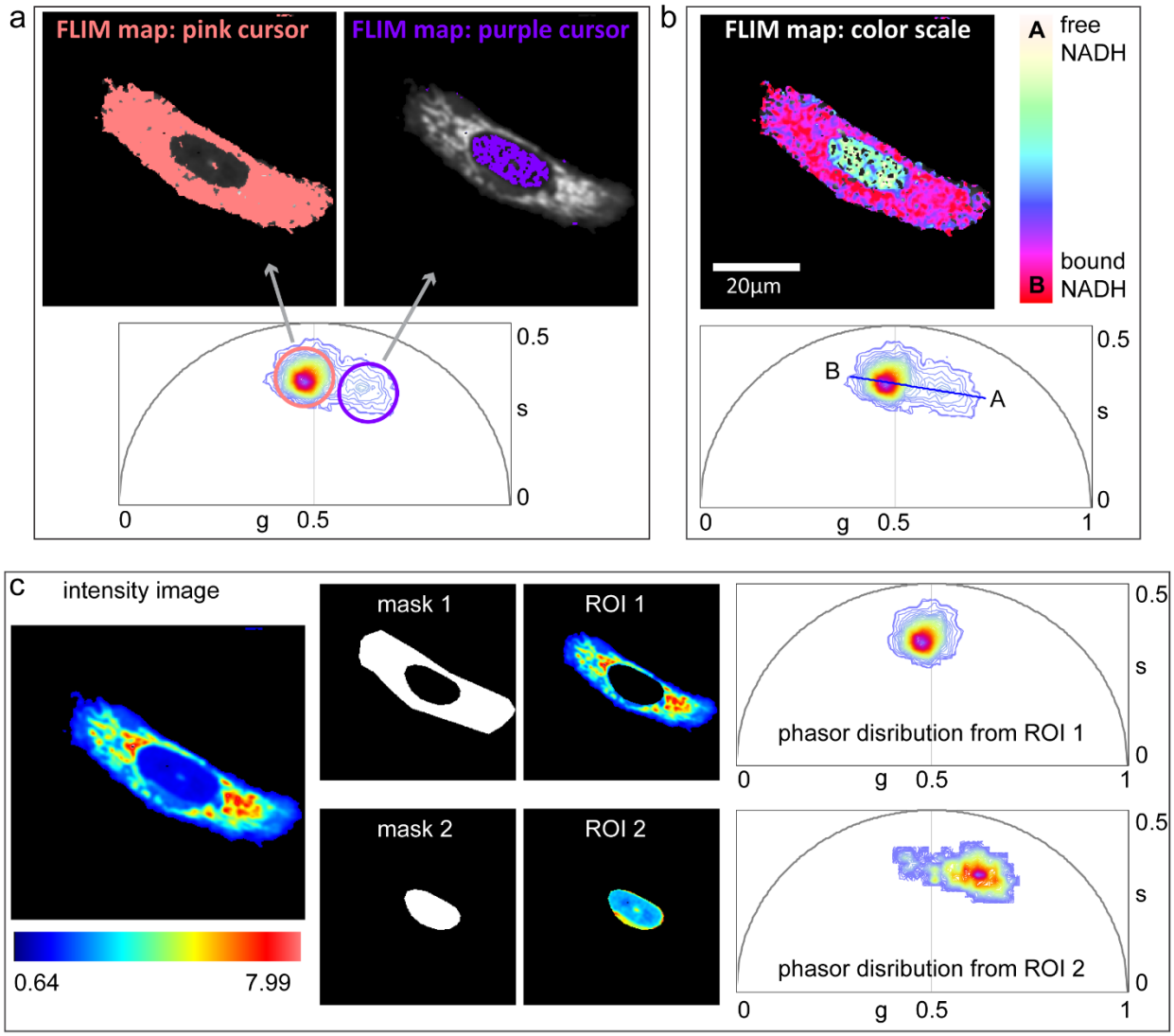

Fig 2.5 FLIM map by phasor analysis. (a) FLIM map by cursor selection method. (b) NADH FLIM map created by colorscale white/yellow to red/pink applied between positions A and B on the phasor distribution, representing linear decrease of free to protein bound NADH ratio. (C) Masking to obtain phasor distributions of separate region of interest (ROI) with the image. Left panel shows the average fluorescence intensity image. Middle panel shows two manually drawn masks (1 and 2) and the corresponding intensity image after application of masks. Right panel shows the phasor distribution from ROI 1 and ROI 2.

The second FLIM map representation, essentially used to create 'NADH FLIM map' in this thesis, takes advantage of the linear addition property of phasor. To color code the linear decrease in free to protein bound NADH ratio along metabolic trajectory, as defined in the previous section, a continuous color scale can be applied. This will create a free to bound

NADH FLIM map according to the color scale. For example, in Fig 2.5(b), the color scale white/yellow to red/pink represents linear decrease of free to protein bound NADH ratio. To create the NADH FLIM map, this color scale was applied between the extreme ends of the phasor distribution, dividing it into 32 levels. Throughout the thesis this color scale will be maintained.

It is important to note that this analysis technique is reciprocal, i.e., if we select a region of interest manually or by feedback from other known fluorophores, the corresponding phasor distribution of only the masked segment of the image can be obtained Fig 2.5 (c).

2.5 Spectral phasor analysis in brief

Spectral phasor analysis is a simple graphical technique for spectral unmixing[100,101]. This entails Fourier transformation of fluorescence spectrum in each pixel to obtain the g (x-coordinate) and s (y-coordinate) using the following equations:

$$g_{i,j}(\lambda) = \frac{\sum_\lambda I_{i,j}(\lambda) \cos\frac{2\pi\lambda}{L}}{\sum_\lambda I_{i,j}(\lambda)} \tag{22}$$

$$s_{i,j}(\lambda) = \frac{\sum_\lambda I_{i,j}(\lambda) \sin\frac{2\pi\lambda}{L}}{\sum_\lambda I_{i,j}(\lambda)} \tag{23}$$

Where $I_{i,j}$ is the intensity at pixel (i, j) at each channel step of the spectrum (32 channels). L is the total wavelength range (416-728 nm). The g and s coordinates vary between 1 and -1. The position of the spectral phasor on the spectral polar plot depends on the center of mass and the full width of the half maximum (FWHM) of the spectrum. The angular position of the

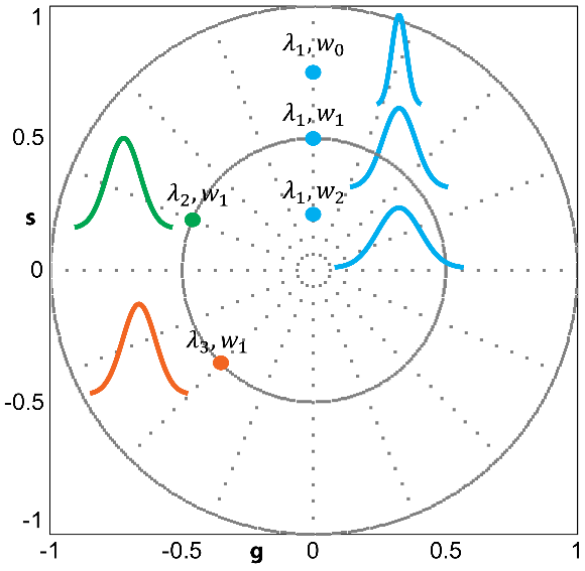

Fig 2.6 Schematic of spectral phasor representation. The angular position of the phasor gives the center of mass of the spectrum ($\lambda_1 < \lambda_2 < \lambda_3$) while the radial position is defined by the spectrum's FWHM ($w_0 < w_1 < w_2$).

phasor gives the center of mass of the spectrum while the radial position is defined by the spectrum's FWHM (Fig 2.6). phasor gives the center of mass of the spectrum while the radial position is defined by the spectrum's FWHM (Fig 2.6).

2.6 FLIM instrumentation

The FLIM frequency domain measurement was collected on Zeiss LSM 710 microscope (Carl Zeiss, Jena, Germany). For excitation, 80MHz multiphoton excitation laser source, Titanium:Sapphire MaiTai laser (Spectra-Physics, Mountain View, CA) was used with excitation at 740nm. Image scan speed was 25.21 µs/pixel and image size is 256 × 256 pixels. For separating excitation from emission signal a dichroic filter at 690 nm was employed. A bandpass emission filter 460/80nm (Semrock, Rochester, NY) coupled to a photomultiplier tube (H7422P-40, Hamamatsu, Japan) was used as the microscope external detector port photo-sensor unit. FLIM data was acquired using A320 FastFLIM FLIMbox (ISS, Champaign,

IL). For acquisition and FLIM data processing the SimFCS software developed at the Laboratory of fluorescence dynamics (LFD, UC Irvine) was used. For calibrating the FLIM system, Rhodamine 110 with known lifetime of 4.0 ns was measured for every experiment. All the (g, s) coordinate systems in this this thesis employ the fundamental frequency of the laser at 80MHz (repetition rate of the laser).

2.7 Chapter Summary

In this chapter the methods employed in this thesis was discussed. In the first part of the chapter the different techniques to measure fluorescence lifetime imaging microscopy was explained. Specifically, frequency domain method was elaborated, followed by discussion on the detection schemes with a brief history about the FLIMbox development. The second part of the chapter focused on phasor approach of FLIM data analysis and its advantages followed by a brief discussion on NADH FLIM -phasor technique to study cell and tissue metabolism that were previously reported.

Chapter 3

A new approach to label-free detection of oxidative stress

Chapter overview: In this chapter, we establish for the first time, a novel oxidative stress detection technique by FLIM of an endogenous fluorophore. In this work, FLIM-phasor serves discovery tool of this intrinsic species with characteristic fluorescence lifetime signature. This technique, coupled with metabolic imaging using NADH lifetime, could have tremendous potential to study pathological response of cells and tissues. The most attractive feature is its non-invasiveness, which unveils opportunities for in vivo animal studies.

This work has been published in the following papers:

Datta, R., Alfonso-Garcia, A., Cinco, R., and Gratton, E. Fluorescence lifetime imaging of endogenous biomarker of oxidative stress. Scientific Reports, 5, 9848 (2015).

Borrego, S. L., Fahrmann, J., Datta, R., et al. Metabolic changes associated with methionine stress sensitivity in MDA-MB-468 breast cancer cells. Cancer & Metabolism, 4:9 (2016).

3.1 Introduction

Reactive oxygen species (ROS) are intrinsic free radicals produced as a result of normal cellular metabolism. As discussed in Chapter 1, ROS concentration at moderate level plays a role in signaling pathways of physiological processes and in maintaining redox homeostasis[11–13]. However, increased concentration of ROS causes oxidative stress. This is detrimental to the cellular components because of several biochemical processes including

lipid peroxidation and proteins and DNA damage[13]. Modifications of these biomolecules could ultimately lead to a number of human diseases such as inflammation, diabetes mellitus, atherosclerosis, cancer, and neurodegenerative disease[102–108]. Therefore, biomarkers of oxidative stress play an important role in understanding the pathogenesis and treatment of these diseases.

Detecting ROS itself is a direct measure for identifying the presence of oxidative stress. ROS-specific fluorescent indicators are available commercially. However, the use of these indicators requires administration of a foreign material to the physiological environment. Moreover, there are a number of concerning factors which might influence the measurement. These include its solubility in lipid versus aqueous environment, ability to cross biological membranes, sample preparation and required time for incubation, influences of physiological conditions like temperature and pH, and so on[109]. Instability of ROS molecules and further perturbation of biological systems by the current invasive ROS detection techniques make this a difficult task. Indirect techniques for detecting ROS utilize the more stable ROS oxidation products. These identify damage to biomolecules by ROS or quantify levels of antioxidants or redox molecules. A detailed account of the current techniques for ROS detection was described in Chapter 1, section 1.2. In this work, we show label-free detection of oxidative stress by fluorescence lifetime measurement of intrinsic fluorescent species using multiphoton fluorescence microscopy. These species with granular appearance co-localize with lipid droplets. We hypothesize that the identified species are products of lipid oxidation by ROS. A similar preliminary observation was reported previously in human embryonic stem cells[58]. The identified endogenous biomarker unfolds opportunities of performing non-invasive measurements of oxidative stress in vivo.

Multiphoton fluorescence microscopy (MPM) has been employed previously to perform label free fluorescence lifetime imaging (FLIM) of intrinsic fluorophores like reduced nicotinamide adenine dinucleotide (NADH), collagen, retinol, retinoic acid and melanin[58,90,110]. The main advantages of MPM are reduced phototoxicity and higher penetration depth, needed for in vivo measurements especially in tissue samples. Endogenous fluorophores enable non-invasive imaging of biological samples, minimizing the perturbation of normal physiological conditions. For example, autofluorescent metabolic coenzymes flavin adenine dinucleotide (FAD) and NADH are frequently employed as probes of metabolism for label-free imaging[54,111]. For analyzing the fluorescent decay in FLIM images, we employed the phasor approach. This method simplifies and speeds up the analysis as it works on the raw data without the need to perform a fit of the fluorescence decay at each point of an image[82]. Moreover, it does not require a priori knowledge of the fluorescence lifetime components in the imaged sample and gives instantaneous results. Details of the phasor method has been discussed it chapter 2. However, to recapitulate briefly, the data from each pixel of the image is subjected to a Fourier transformation to obtain the corresponding phasor as previously described[58,82]. In the phasor approach we can identify separate clusters of species with different lifetimes on the phasor plot, and map them back to the image to resolve the spatial location of these species.

To validate the concurrence of lipid droplets with the identified oxidative stress biomarkers, we combined the FLIM approach with two coherent nonlinear microscopy techniques: third harmonic generation (THG) imaging microscopy and coherent anti-Stokes Raman scattering (CARS) microscopy. It is known that a strong THG signal is generated at the interface between media with difference in third order nonlinear susceptibility, refractive index and

dispersion. In particular it has been shown that the interface between a lipid droplet and its surrounding produces a strong THG contrast[112]. Hence, the technique can be employed to selectively identify lipid bodies in biological samples. CARS is another label-free technique used for imaging neutral lipid droplets. The contrast of the CARS signal in the lipid droplets arises from the Raman response of the abundant C-H bonds in lipid molecules[113]. Thus, laser scanning CARS microscopy is applied to visualize lipid droplets in cells and tissues. Both of these techniques have the advantage of being label-free and non-invasive while they can still be correlated to the results of FLIM imaging.

To further investigate the chemical nature of the observed species, we performed classical Raman spectral analysis. Raman spectroscopy has the advantages of providing high molecular selectivity[114], and non-invasiveness especially compared to techniques like mass spectroscopy. We employed a confocal Raman microscope where we could select specific locations on the biological sample, and acquire Raman spectra from these areas. For identifying lipids on our samples, we looked at the fingerprint region and the C-H stretching vibration region. Characteristic spectra of lipid droplets have previously been identified in these Raman bands[115,116].

In this work, we establish a non-invasive, label-free MPM method to identify biomarker of oxidative stress. We found the identified endogenous fluorescent species to have a characteristic fluorescence lifetime distribution on the phasor plot. MPM imaging provided high resolution imaging and by phasor analysis of FLIM, this biomarker could be easily identified in live cells and ex-vivo tissues and correlated to lipid droplet locations. We hypothesize that the fluorescent species is a product of lipid oxidation by ROS. We show co-

localization of the spectroscopic signals to lipid droplets by combining FLIM with THG and CARS microscopy, techniques employed for selective lipid body imaging. Raman spectral analysis on the regions with this characteristic lifetime provided additional evidence of molecular vibrations arising from oxidized lipids. Finally, we show application of this technique in cancer.

3.2 Materials and methods

3.2.1 FLIM and THG instrument

Fluorescence lifetime imaging measurements of HeLa cells were performed on Zeiss LSM 710 microscope (Carl Zeiss, Jena, Germany) using a 40x water immersion objective, 1.2 N.A. (Carl Zeiss, Oberkochen, Germany). For the 2-Photon excitation laser source, Titanium:Sapphire MaiTai laser (Spectra-Physics, Mountain View, CA) was used with excitation at 740nm. Image scan speed was 25.21 µs/pixel and image size is 256 × 256 pixels. For separating excitation from emission signal a dichroic at 690 nm was employed. The emission filter used was a bandpass 460/80 nm and photomultiplier tube (H7422P-40, Hamamatsu, Japan) was used for detection. FLIM data was acquired using A320 FastFLIM FLIMbox (ISS, Champaign, IL).

FLIM and third harmonic generation imaging of tissue sample was acquired using a custom-built upright deep tissue imaging microscope. The operation principle has been discussed previously[117]. For FLIM measurements, tissue sample was excited at 740nm and emission filter employed was bandpass 405 - 590 nm. For THG, excitation of 1038nm was used and signal was collected with bandpass filter 320-390 nm. Both FLIM and THG signals were collected in transmission geometry on the same sample.

For FLIM and THG data acquisition and processing, the SimFCS software developed at the Laboratory of Fluorescence Dynamics (LFD, UC Irvine) was used.

3.2.2 CARS instrument

Coherent anti-Stokes Raman scattering (CARS) images were obtained by combining a 1064nm, 76MHz mode-locked Nd:Vanadate laser (Picotrain, High-Q, Hohenems, Austria) and a 817nm beam tuned from a MIRA 900 (Coherent, Santa Clara, California). The two beams were overlapped both temporally and spatially, and sent into a laser scanner (Fluoview 300, Olympus, Center Valley, PA), attached to an inverted microscope (IX71, Olympus). The combined beams were then focused through a 20x 0.75 NA objective lens (UPlanSApo, Olympus) onto the sample. The CARS signal was collected through the transmission channel by a photomultiplier tube (Hamamatsu, Japan) after passing through a 625/50 filter.

3.2.3 Raman spectroscopy

Spontaneous Raman spectra from the lipid droplets present in the cells were acquired with a commercial Raman microscope (InVia Confocal; Renisahw, Wotton-under-Edge, Gloucestershire, UK). The excitation wavelength at 523nm was focused into the sample with a 50x objective, and the scattered light was sent into the spectrometer that contained a 2400 l/mm grating. The autofluorescent lipid droplets are identified based on morphology. The Raman spectrum is then taken with 10s integration time, and the baseline was estimated by minimizing a non-quadratic cost function.

3.2.4 Adipose tissue

White adipose tissue was obtained from 5 month old adult female mice. Approximately 3mm diameter portions of fat from perigonadal white adipose tissue, flank white adipose tissue and intracapsular brown adipose tissue depots were freshly excised from the mice and subsequently embedded in 1% low melt agarose in HBSS heated to 37˚C between coverslips separated by 0.2mm spacers. All images were acquired strictly within 1 hour of tissue extraction. All animal procedures were performed with strict adherence to NIH OLAW and institutional IACUC guidelines.

3.2.5 HeLa cell culture and oleic acid treatment

HeLa cells were grown in Dulbecco's Modified Eagle Medium (D-MEM) (1X), liquid (high glucose) supplemented with 10% Fetal Bovine Serum, and 1% penicillin streptomycin (100IU/ml) at 37^0C in a 5% CO_2 incubator. For oleic acid treatment, the cells were cultured in 5% lipoprotein deficient serum, LPDS (Intracel, Frederick, Maryland) and 95% D-MEM for 24 hours. Fatty acid free bovine serum albumin was prepared by dissolving BSA powder (Sigma-Aldrich, St. Louis, Missouri) in 5% LPDS media. 400μM oleic acid was prepared as a complex with BSA (OA/BSA) at molar ratio of 2:1. Cells were treated with OA/BSA complex overnight. For controls, three different dishes of HeLa cells were cultured in normal media and 5% LPDS media. For imaging, the cells were plated in glass bottom dishes (Matek Corporation, Ashland, Massachusetts). Prior to FLIM imaging, the oleic acid fed cells were washed with 1X Dulbecco's Phosphate Buffered Saline, DPBS (Sigma-Aldrich). For CARS imaging, media was replaced with DPBS. 4% Paraformaldehyde (Sigma-Aldrich) solution was prepared to fix the cells for Raman spectroscopy measurements.

3.2.6 Solution preparation

For pure free and protein bound NADH FLIM measurements, 2.5 μM NADH were diluted in 10mM $NaH_2PO_4*H_2O$ at pH=7.4. For bound, it was mixed with 0.75U/ml Lactate dehydrogenase (LDH). For lifetime measurement of retinoid in bovine serum albumin (BSA), retinol (Sigma-Aldrich) was dissolved in dimethyl sulfoxide, DMSO (EMD Millipore, California) and added to BSA (Sigma-Aldrich) in buffer.

3.2.7 Melanoma cells

Melanoma cell line SkMel28 and normal melanocyte were obtained from Liu-Smith lab, Chao Family Comprehensive Cancer Center, University of California Irvine.

3.2.8 Breast cancer cells

MDA-MB-468 were maintained in DMEM (Sigma-Aldrich, D0422) supplemented with 10% dialyzed FBS (Gemini Bio-Products), 1.5 μM cyanocobalmin (vitamin B12), 4 mM L-glutamine, 100 μM L-cysteine (Fisher Scientific), and 100 μM L-methionine (Sigma-Aldrich). In the case of methionine-free media, 370 μM DL-homocysteine (Sigma-Aldrich) or 370 μM DL-homocysteine-$^2H_4$ (13C Molecular, 12714-158) was added in the absence of methionine.

Resistant cell lines were isolated as described in Hoffman, *et al* (1979). Briefly, MDA-MB- 468 resistant clones were isolated after prolonged culturing in methionine-free media. The majority of MDA-MB-468 cells detach; however, resistant clones begin to appear after two weeks. Clones were isolated and proliferation rates were measured using CellTiter-Glo luminescent cell viability assay (Promega).

For FLIM, MDA-MB-468 and MDA-MB-468res-R8 cells were cultured in methionine or homocysteine media. To inhibit oxidative phosphorylation, cells were treated with 4 mM potassium cyanide (KCN) for 5 minutes before imaging.

3.3 Results

3.3.1 Identification of unique a long lifetime species in white adipose tissue by FLIM

We performed fluorescence lifetime imaging (FLIM) measurements on freshly excised perigonadal white adipose tissue (WAT). We identified a long lifetime distribution cluster in the phasor plot shown in Fig 3.1 (a), encircled with red cursor, by phasor analysis of the acquired FLIM data. This phasor distribution of the long lifetime species (LLS) has a distinct position on the phasor plot separate from the NADH-FLIM signature, Fig 3.1(a), encircled with yellow cursor. The LLS and NADH FLIM phasor clusters are mapped back onto the intensity image, Fig 3.1(b). The tissue regions exhibiting the long lifetime component are colored red. These pixels correspond to the areas within the large lipid droplets present in the adipocytes. The NADH-FLIM cluster is chosen by the yellow cursor on the phasor plot, and this selection corresponds to regions surrounding the lipid droplet: adipocyte cytoplasm, nuclei, and the extracellular regions.

To further ascertain that the pixels selected by the red cursor are associated to lipids, we performed THG imaging on the same region. We found a strong THG signal arising from the periphery of lipid droplets[112] [Fig 3.1 (c)]. The LLS FLIM map overlaid on the THG image reveals the periphery of regions with long fluorescence lifetime have strong THG signal as shown in Fig 3.1(d) with regions of overlap in pink. This is consistent with our hypothesis

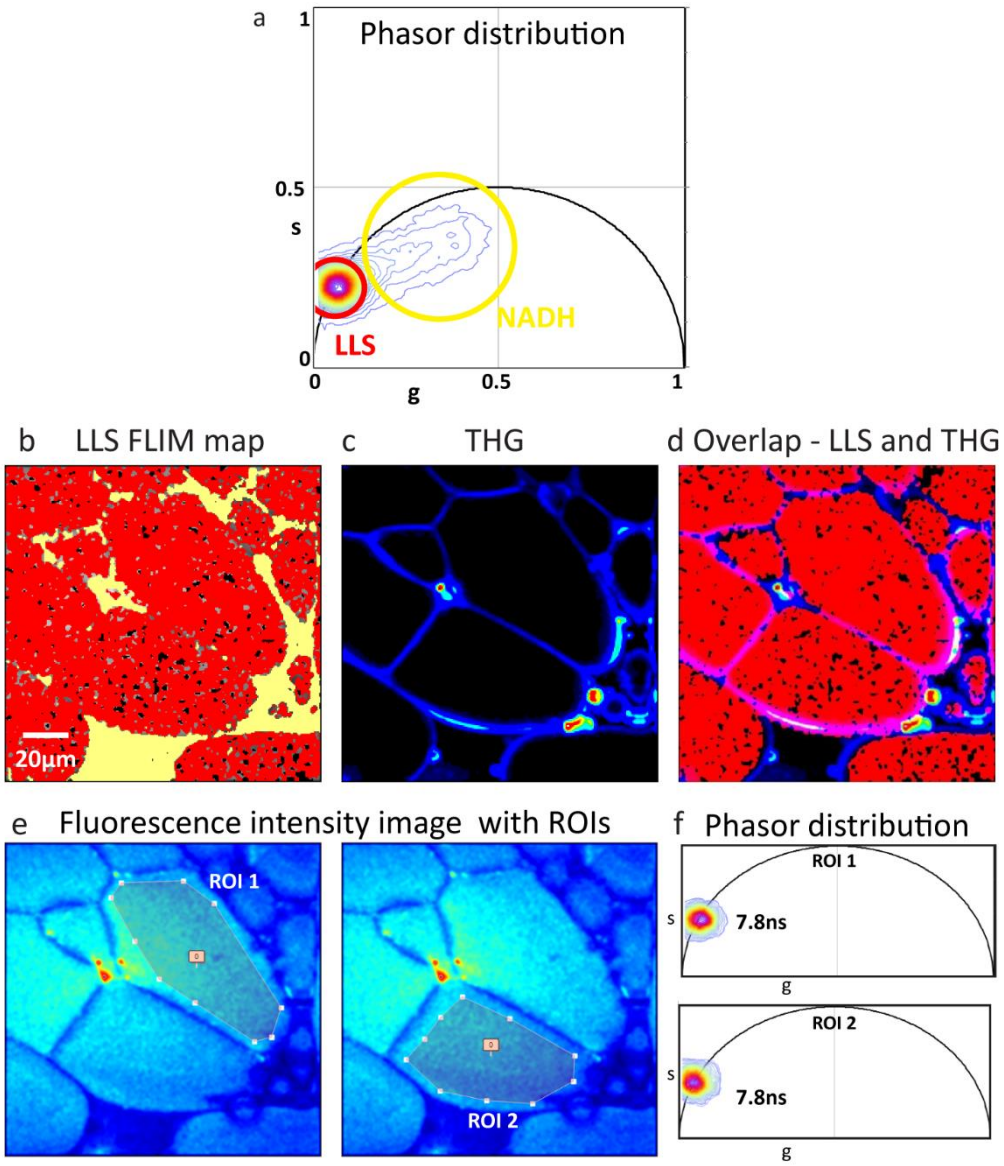

Fig 3.1 Unique fluorescence long lifetime signature (LLS) in white adipose tissue and correlation with THG image. (a) Phasor distribution of white adipose tissue excited at 740nm. The red circular cursor selects the long lifetime distribution cluster while yellow cursor chooses the NADH phasor distribution. (b) FLIM pseudo-color map with red and yellow regions corresponding to the two identified phasor clusters selected with red and yellow cursors respectively. Scale bar is 20µm. (c) THG intensity image with the sample excited at 1038nm. (d) composite image of LLS FLIM map and THG image. Pink areas are regions of overlap. (e) Phasor plots showing the corresponding phasor distributions of the ROIs.

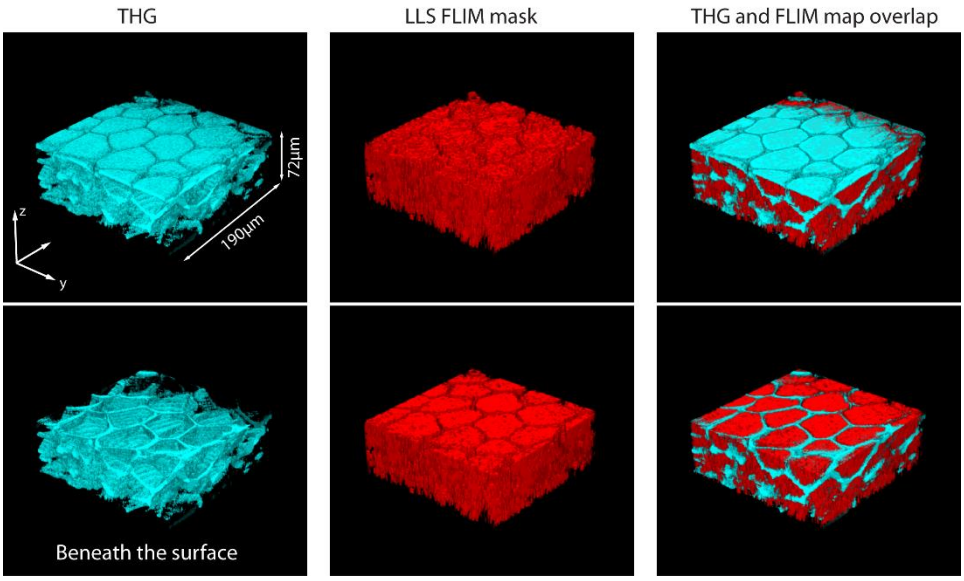

Fig 3.2 Simultaneous THG and FLIM in WAT reconstructed from 25 z – slices at every 3µM of the tissue. Top row shows 3D reconstructed THG signal (left panel in cyan), 3D FLIM map of long lifetime species (middle panel in red) and overlay of THG on LLS map 3D reconstruction (right panel) of white adipose tissue. Bottom row shows the THG, LLS FLIM map and their overlay from the same tissue sample reconstructed from below the top surface

that we are observing lipid droplet associated autofluorescence. Based on FLIM and THG results, we manually drew region of interests (ROI) in two different lipid droplets of the average fluorescence intensity image [Fig 3.1 (e)]. The phasor distribution associated to these ROIs [Fig 3.1 (f)] shows a unique lifetime that represents a fingerprint on the universal circle of the phasor (7.8ns).

To verify presence of this LLS signal throughout the adipocytes, we acquired FLIM and THG of 25 z-slices at every 3µm of the visceral white adipose tissue from surface to a depth of 72µm. Fig 3.2 shows the 3-D reconstruction of THG (cyan), LLS FLIM map (in red), and their overlap. Fig 3.2, bottom row shows the 3-D reconstruction beneath the surface of the tissue.

To investigate the differences of the long lifetime species in visceral versus subcutaneous WAT, we performed FLIM on visceral fat depot (perigonadal WAT) and subcutaneous fat

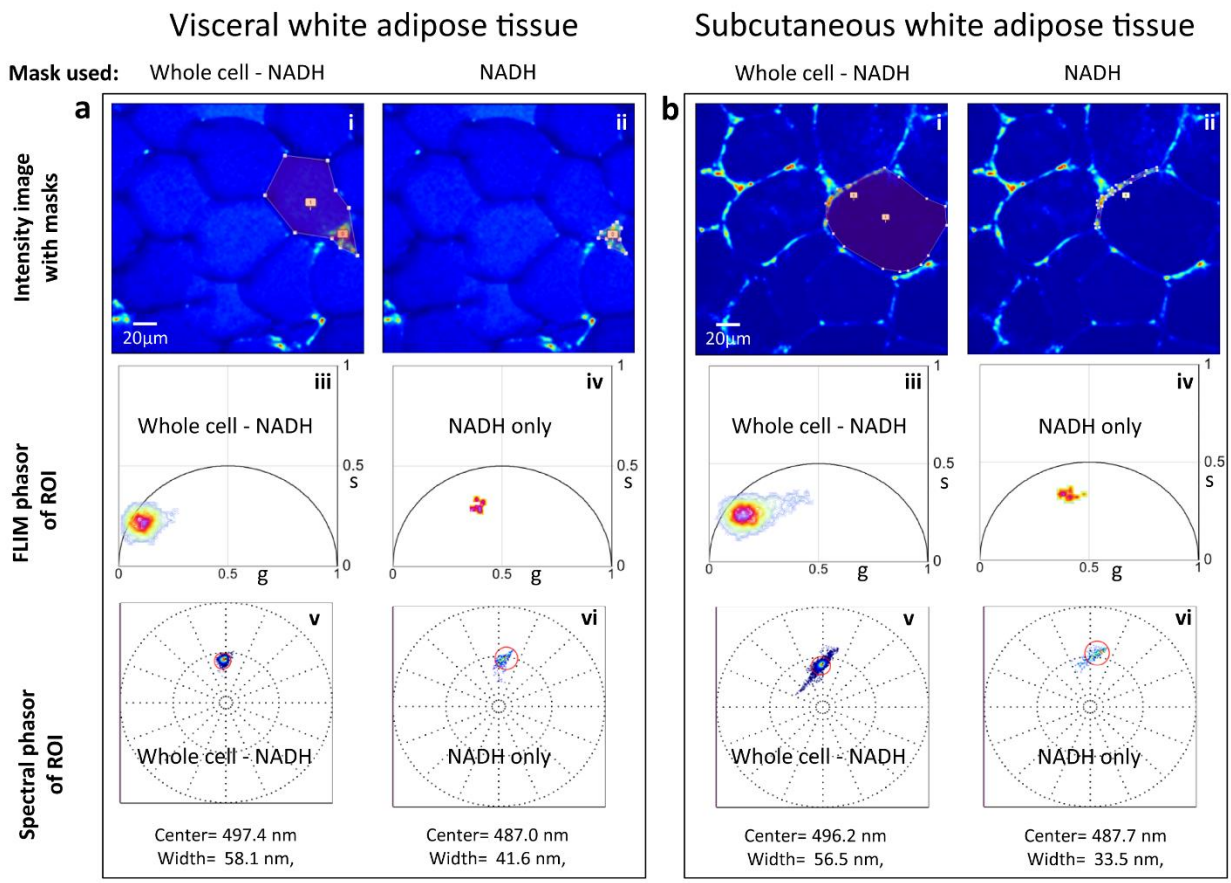

Fig 3.3 FLIM and spectral phasor distribution of visceral and subcutaneous white adipose tissue. (a) Top panel are fluorescence intensity images of visceral white adipose tissue with the ROI masks [Whole cell – NADH] (a i) and [NADH] (a ii). Middle panel are FLIM phasor distribution from the masks. a iii shows FLIM phasor distribution form mask in (a i) while (a iv) shows FLIM phasor distribution form mask in (a ii). Bottom panels are spectral phasor distribution from the masks. (a v) shows FLIM phasor distribution from mask in (a i) and (a vi) shows FLIM phasor distribution from mask in (a ii). (b) Top panel are fluorescence intensity images of visceral white adipose tissue with the ROI masks [Whole cell – NADH] (b i) and [NADH] (b ii). Middle panel are FLIM phasor distribution from the masks. (b iii) shows FLIM phasor distribution from mask in (b i) while (b iv) shows FLIM phasor distribution from mask in (b ii). Bottom panels are spectral phasor distribution from the masks. (b v) shows FLIM phasor distribution from mask in (b i) and (b vi) shows FLIM phasor distribution from mask in (b ii).

depot (flank area) of the same animal. We also collected spectral emission data from the same tissue area and analyzed the emission characteristics using the spectral phasor approach method described previously[93]. Fig 3.3 shows the FLIM phasor and spectral phasor (discussed in Chapter 2) analysis in the field of view for the two kinds of WATs. Separate

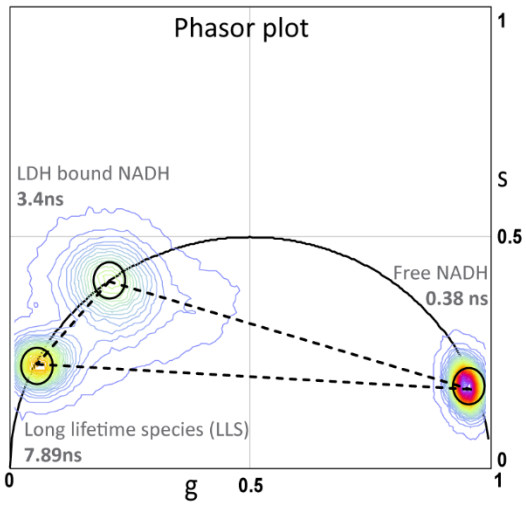

Fig 3.4 Phasor fingerprint. Phasor plot showing triangle formed by FLIM fingerprints of free 2.5 µM NADH in solution, NADH bound to 0.75U/ml Lactate dehydrogenase (LDH) enzyme and unique LLS from lipid droplets in perigonadal WAT of female mouse. From the law of phasor addition, a system containing mixtures of these three species will fall within the triangle joining the three phasors

masks were applied manually to select the whole cell (Mask 1) and the region with NADH FLIM signature (Mask 2) within the selected cell. For generating Mask 2 we were guided by the FLIM phasor distribution where the decay of NADH can be distinguished. The Boolean XOR operation was performed between Mask 1 and Mask 2 to obtain the resulting *Whole cell–NADH* mask. The FLIM phasor distribution (Fig 3.3(a iii), visceral WAT and Fig 3.3(b iii), subcutaneous WAT) and the spectral distribution, Fig 3.3(a v), visceral WAT and Fig 3.3(b v), subcutaneous WAT) were mapped back onto the phasor plot after application of *Whole cell–NADH* mask on the imaged area. The FLIM phasor distribution (Fig 3.3(a iv), visceral WAT and Fig 3.3(b iv), subcutaneous WAT) and the spectral phasor distribution (Fig 3.3(a vi), visceral WAT and Fig 3.3(b vi), subcutaneous WAT) were mapped back onto the phasor plot, after application of the *Whole cell–NADH* mask. The spectral phasor method was employed together with lifetime measurements to determine the characteristic emission average spectrum of the areas that correspond to long lifetime species (LLS) and those with

NADH FLIM signature. The spectral phasor distribution of the LLS was centered on 497.4 nm for visceral WAT and 496.2 nm for subcutaneous WAT. NADH spectral phasor distribution was centered at 487nm for both the WATs.

3.3.2 FLIM phasor signature of long lifetime species

In the phasor approach to FLIM, according to the vector law of phasor addition, if a pixel contains a mixture of two molecular species, the corresponding phasor will be distributed along a line joining the two pure species phasors[82]. Here we have a system of three molecular species, namely free NADH, protein bound NADH, and oxidized lipid associated fluorescent species (LLS). The line joining the free and protein bound NADH, which is from 0.4ns to 3.4ns in the phasor plot, has been previously named the "metabolic trajectory"[58,90] on the phasor plot. From Fig 3.1, the FLIM signature of pure LLS can be established to be 7.8ns. The phasor of a pixel in the image containing a mixture of the three species will lie inside the triangle whose vertices are formed by the phasors of the three pure species on the phasor plot (Fig 3.4). For the NADH lifetime signature, FLIM of pure free NADH and NADH bound to lactate dehydrogenase was used to locate the extremes of the bound and free NADH trajectory. The distribution of LLS was obtained from the WAT in Fig 3.1.

3.3.3 Long lifetime species in brown adipose tissue

We further investigated FLIM signature from brown adipose tissue (BAT), the second type of fat present in the body. These have functions complimentary to WAT. While WAT is specialized for storing energy in large lipid droplets, BAT has much smaller lipid droplets and functions to burn fat. Most importantly, it has been shown that ROS induced oxidative

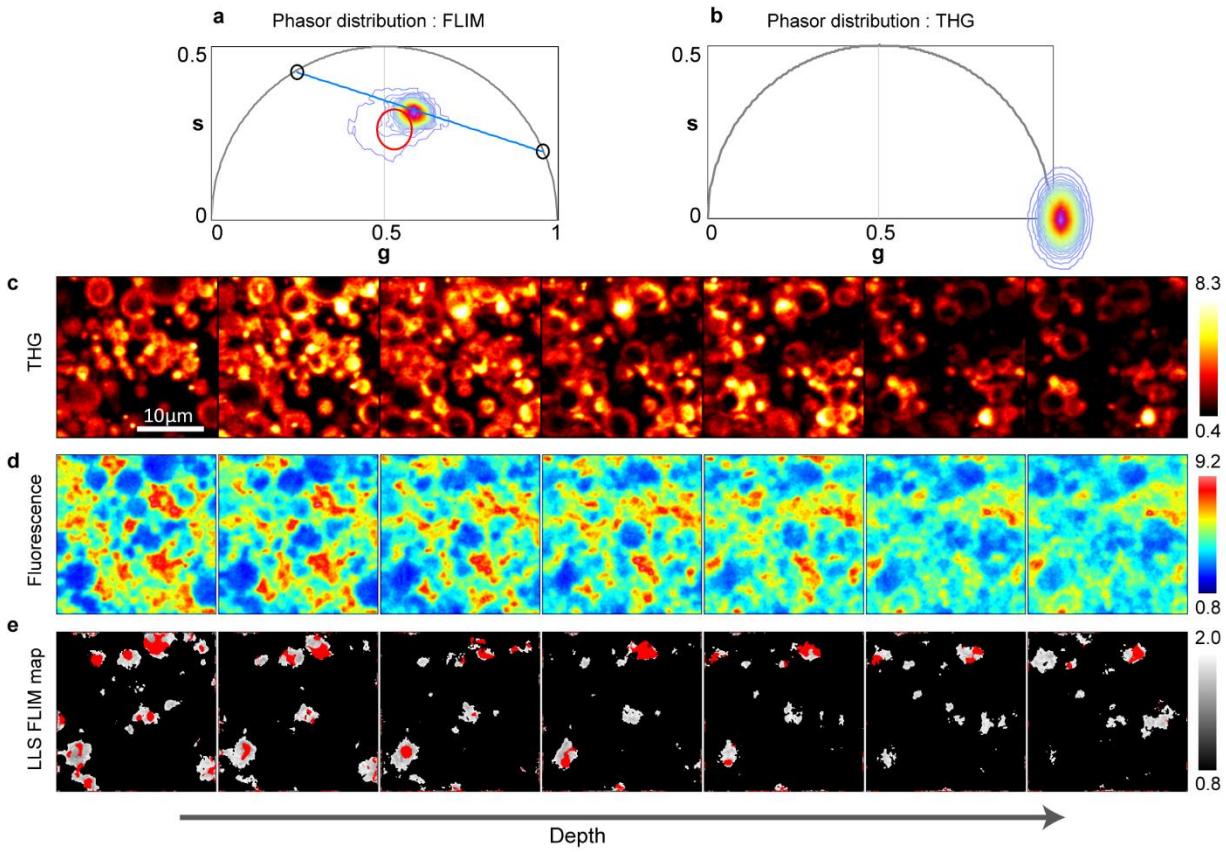

Fig 3.5 FLIM and THG from 7 z-slices of intracapsular brown adipose tissue (BAT) at every 1µM of the tissue (a) Phasor distribution of BAT excited at 740nm. Blue line indicates metabolic trajectory (b) corresponding THG phasor plot of the BAT z-slices excited at 1038nm. (c) THG images of 7 z-slices, 1µM apart. (d) Corresponding fluorescence intensity images. (e) LLS FLIM map in red selected by red cursor in (a) overlaid on fluorescence intensity images thresholded to remove high intensity pixels.

stress associated with accumulated fat occurs in WAT whereas BAT burns excess fat as a protection against obesity. Simultaneous FLIM and THG of intracapsular BAT were acquired from the same animal as Fig 3.2. LLS phasor cluster is not highly prominent as that observed in WAT and is shifted towards the NADH FLIM phasor cluster, Fig 3.5 (a). Fig 3.5(c) shows the THG of 7 z-slices, 1µM apart through BAT. As expected, THG images revealed much smaller and larger quantity of lipid droplets in BAT compared to unilocular WAT cells. Since the brown adipocytes are smaller cells, we acquired images with smaller field of view

compared to WAT of the same animal. Fig 3.5(e) shows the corresponding LLS FLIM map in red.

3.3.4 Long lifetime species in HeLa cells treated with oleic acid

For characterizing the biochemical origin of the LLS associated with lipid and oxidative stress, we treated HeLa cells with oleic acid to stimulate lipid droplet formation in the cells. Oleic acid supplementation often results in increased neutral lipid accumulation in form of lipid droplets [118,119]. Additionally, it has been reported that oleic acid increases ROS generation and oxidative stress [120,121]. For control study, we cultured HeLa cells in normal media as well as lipoprotein deprived serum (LPDS) media, which are not expected to generate elevated numbers of lipid droplets or cause additional stress. In the FLIM phasor distribution of oleic acid fed HeLa cells, Fig 3.6 (a iii), we could identify populations with NADH (blue cursor) and LLS (red cursor) FLIM signatures. NADH phasor distribution in the imaged cell falls along the metabolic trajectory shown by a blue dotted line in Fig 3.6(a iii). Using the phasor approach to FLIM, we mapped these populations back to the image to visualize the regions of identified lifetime clusters in the phasor plot. The NADH phasor distribution cluster corresponds to the nucleus and cytoplasm of the cell Fig 3.6(a iv). The LLS phasor distribution falls along the line joining the center of NADH distribution and the pure LLS FLIM signature on the universal circle. This oxidative stress trajectory shown by a red dotted line in Fig 3.6(a iii) lies within the triangle formed by the phasors of free NADH, protein bound NADH, and LLS on the phasor plot, as shown in Fig 3.4. When mapped back

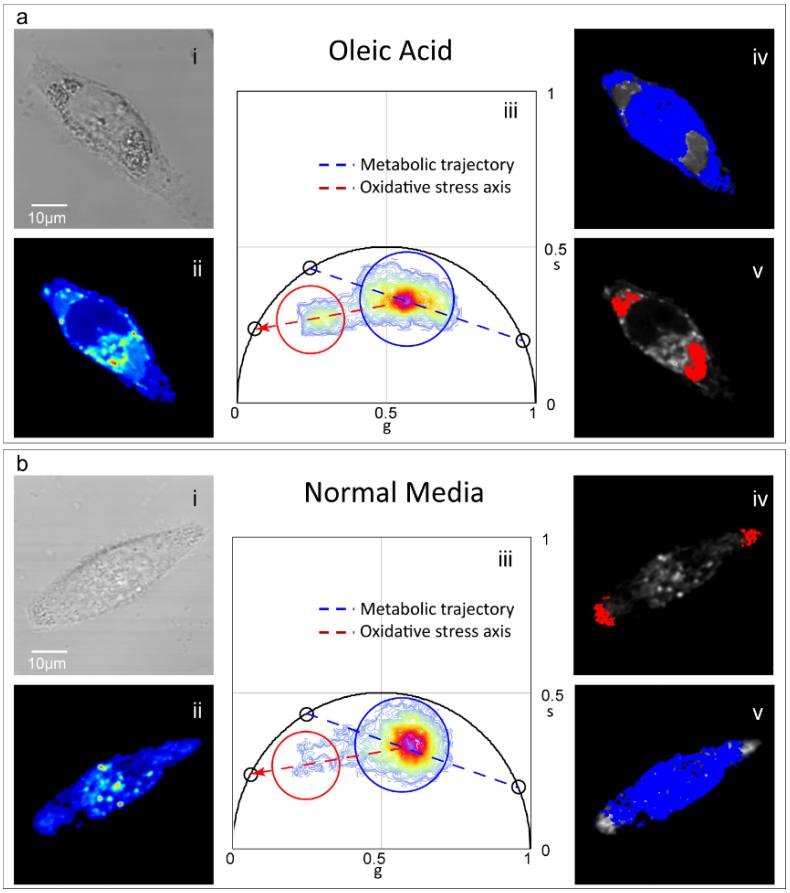

Fig 3.6 Unique LLS FLIM signature and a new oxidative stress axis on phasor plot. FLIM of oleic acid fed HeLa cell. (a) i is the transmission image and a ii is the corresponding fluorescence intensity image with the sample excited with 740nm and emission collected using bandpass filter 480/80 nm. a iii is the resulting phasor distribution from the sample with blue cursor selecting the NADH phasor distribution and red cursor choosing the LLS cluster. Blue dotted line is the metabolic trajectory while red dotted line is the oxidative stress axis. a iv is the NADH map where pixels with lifetime within the blue cursor in a iii are colored blue. a v is the LLS map where pixels with lifetime within the red cursor in a iii are colored red. (b) FLIM of HeLa cell in normal media but exhibiting LLS. bi is the transmission image while b ii is the corresponding fluorescence intensity image using same excitation and emission as a. b iii is the resulting phasor distribution from the sample. The blue and red cursors as well as the metabolic trajectory and the oxidative stress axis are kept at same positions as a iii. B iv is the corresponding NADH map while b v is the LLS map.

regions with long lifetime distribution, chosen by the red cursor, onto the image, these corresponds to the intracellular lipid droplets of the oleic acid treated HeLa cells, Fig 3.6(a v). A small percentage of control HeLa cells cultured in normal media also displayed the LLS

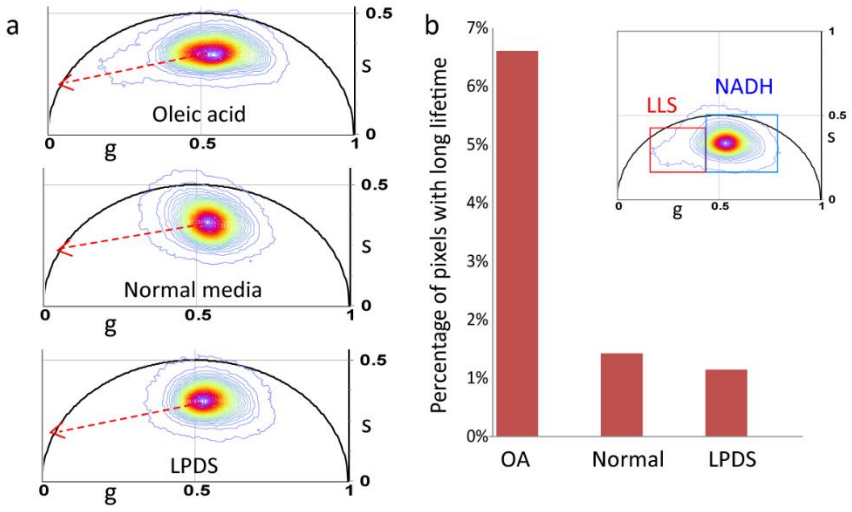

Fig 3.7 Increase in areas with LLS in oleic acid treated HeLa cells. (a) Top panel shows the phasor distribution of HeLa cells treated with 400uM oleic acid for 24 hours. Middle panel shows phasor distribution of HeLa cells in normal media. Bottom panel shows phasor distribution of HeLa cells in lipoprotein deficient serum, LPDS. Red dotted line shows the oxidative stress axis. (b) Inset panel shows binary division of the phasor distribution with LLS window (red square) selecting pixels with longer lifetime and NADH window (blue square) selecting the shorter lifetime distribution. Bar graph showing percentage of pixels within lifetime in the LLS window in the three groups

phasor distribution Fig 3.6(b). However, when the long lifetime species is present, it usually appears in lipid droplets near the cellular membrane

In Fig 3.7 we show FLIM phasor distribution of the three groups of HeLa cells (oleic acid treated, normal media, and LPDS). For each group, FLIM analysis was performed on 12 areas. This included 55 oleic acid fed cells, 58 cells cultured in normal media, and 54 cells in LPDS media. Comparing the individual phasor distribution of the three groups, the LLS population along the oxidative stress axis is found to be markedly pronounced in the oleic acid fed group, while it is negligible in the control groups [Fig 3.7 (a)].

For statistical analysis, the phasor distributions of all three groups were divided into two windows, NADH (blue square) and LLS (red square) as shown in Fig 3.7(b) inset. We calculated the fraction of pixels in all the acquired images with phasors in the NADH window

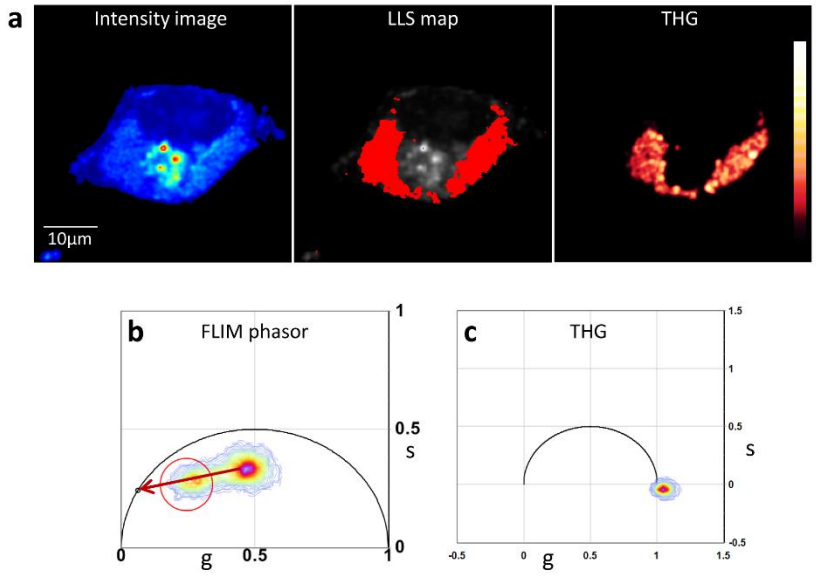

Fig 3.8 Sequential FLIM and THG imaging of oleic acid treated fixed HeLa cell. (a) Left panel is average fluorescence intensity image of treated HeLa cell excited at 740nm. Middle panel is the FLIM map of long lifetime phasor cluster selected by red cursor in the phasor plot (b). Right panel is the THG signal from the same sample excited at 1038nm. (b) FLIM phasor plot with red cursor selecting the long lifetime cluster. (c) THG phasor plot

and the LLS window. These values were normalized to the total number of pixels with phasors in the two windows and converted into percentage. The percentage of pixels in the LLS window in the three groups are plotted in Fig 3.7 (b). The plot shows a 6-fold increase in the lipid droplet associated LLS in HeLa cells treated with oleic acid compared to the control cells in normal media and LPDS media.

3.3.5 Use of label-free techniques to determine the origin of the autofluorescence signal

To further elaborate on our hypothesis that the long lifetime component arises from oxidized lipid associated autofluorescence, we employed THG and CARS imaging along with FLIM of

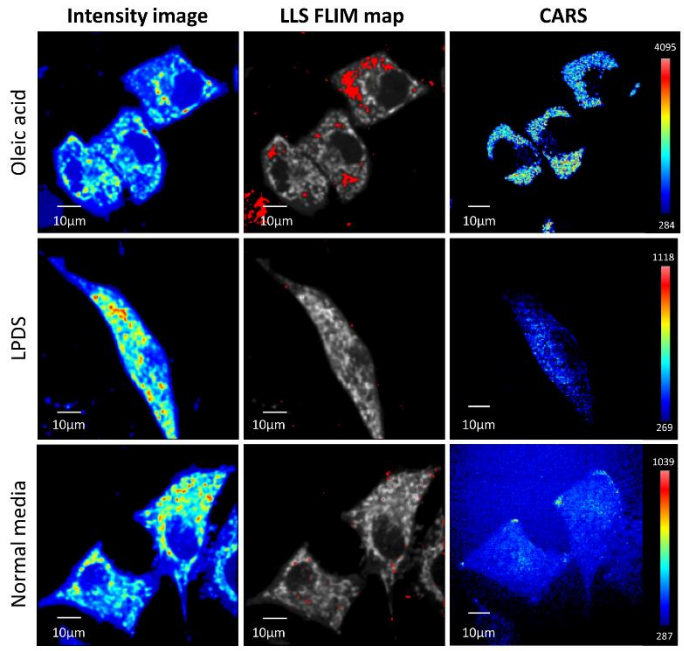

Fig 3.9 FLIM and CARS imaging of oleic acid treated HeLa cells. Top panel is fluorescence intensity image, LLS FLIM map in red and CARS image of oleic acid fed HeLa cells. Bottom panel is fluorescence intensity image, LLS FLIM map in red and CARS image of the control groups of HeLa cells in LPDS media (top row) and in normal media (bottom row).

oleic acid fed HeLA cells. Both these techniques offer additional contrasts for observing lipid structures. Fig 3.8 shows the results of simultaneous FLIM and THG imaging of oleic acid treated fixed HeLa cell. In the phasor plot we identified the LLS cluster along the oxidative stress axis red cursor in the phasor plot as shown in Fig 3.8 (b) and mapped them on the FLIM image (Fig 3.8 (a), middle panel). The area selected by the red cursor falls within the THG signal (Fig 3.8 (a), right panel) arising from lipid droplets.

Further proof for the oxidized lipid origin of LLS was obtained from combined FLIM and CARS imaging. Once again we performed imaging on three groups of HeLa cells - oleic acid treated, LPDS, and normal media. Fig 3.9 shows one representative image from each group. The group treated with oleic acid had much stronger CARS signal revealing abundant and

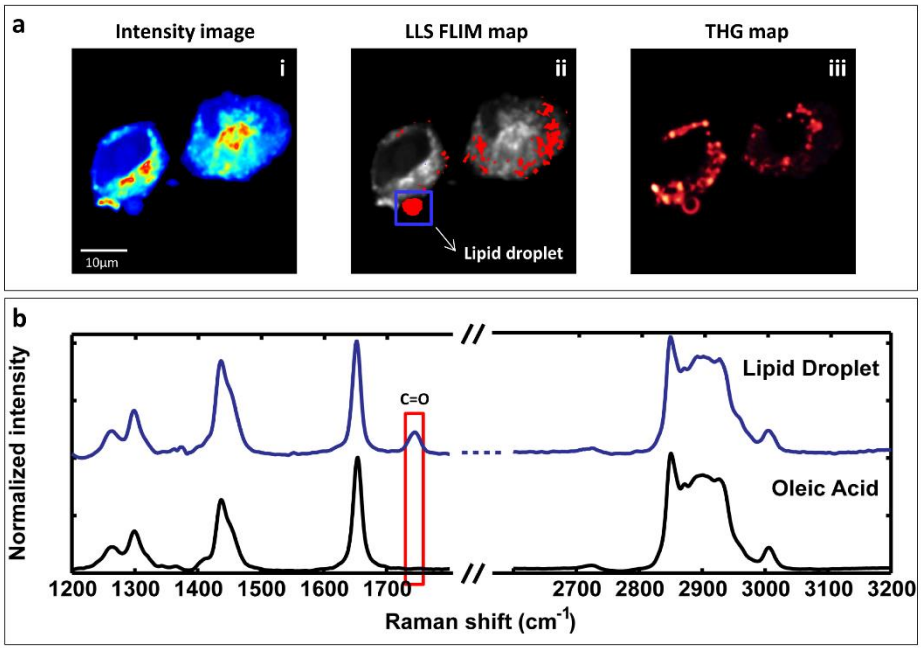

Fig 3.10 Chemical characterization of LLS by Raman spectroscopy. (a) Fluorescence intensity image (a i) of fixed oleic acid fed HeLa cells. a ii is the LLS FLIM map in red. Dotted blue box encloses the lipid droplet with LLS signal from where the Raman spectrum was acquired. a iii is the THG image from the same area. (b) Blue curve is the Raman spectra from the lipid droplet of interest (marked by a blue square in a ii). Black curve is the Raman spectra from 90% pure oleic acid. Red dotted box highlights the additional peak observed in the Raman spectra from biological sample which is not a feature of oleic acid

larger lipid droplets compared to the other two groups. This also correlates with increased areas of oxidized lipid associated autofluorescence in the oleic acid fed group (Fig 3.9, middle column). However, it should be noted that not all lipid droplets, unveiled by CARS signal, exhibit the LLS signature.

3.3.6 Chemical analysis by Raman spectroscopy

For chemical characterization of the oxidized lipid associated species with autofluorescence signal, we obtained Raman spectra at regions of oleic acid loaded HeLa cells that displayed the unique LLS FLIM signature. In Fig 3.10(a ii), the lipid droplet from where Raman spectra were obtained has been indicated by a blue square. This region also had strong THG signal,

Fig 3.10(a iii. The blue curve in Fig 3.10(b) shows the Raman spectra of a lipid droplet in the fingerprint (1200-1800 cm^{-1}) and the CH stretching (2700-3200 cm^{-1}) regions. We also obtained Raman spectra of 90% pure oleic acid (Fig 3.10(b), black curve). The Raman spectra in the CH stretching regions acquired from the LLS containing lipid droplets show the typical vibrational bands of pure oleic acid. There is an additional peak in the fingerprint region at 1746 cm^{-1}, which is assigned to the C=O stretching mode of ester bonds. This bond is formed upon esterification of the fatty acid into neutral triglycerides, which constitute the major component of lipid droplets. For this analysis, Raman spectra were normalized by sections. The fingerprint band data was normalized to the 1646cm^{-1} Raman band, whereas the CH stretching band data was normalized to the 2850cm^{-1} Raman band.

3.4 LLS as biomarker for oxidative stress in cancer

3.4.1 Melanoma

Melanoma, a neoplasm resulting from carcinogenic transformation of melanocyte, has been associated with excess amounts of ROS[122,123]. Melanosomes, the pigment producing structures of melanocytes also functions as a ROS scavenger which are produced in normal cell metabolism and exposure to ultraviolet radiation from sunlight[124]. However, in melanoma, the damaged melanosomes malfunction and generate ROS. Such high levels of ROS cause oxidative stress. Moreover, the free radical promote signaling cascades to protect the tumors cells from death.

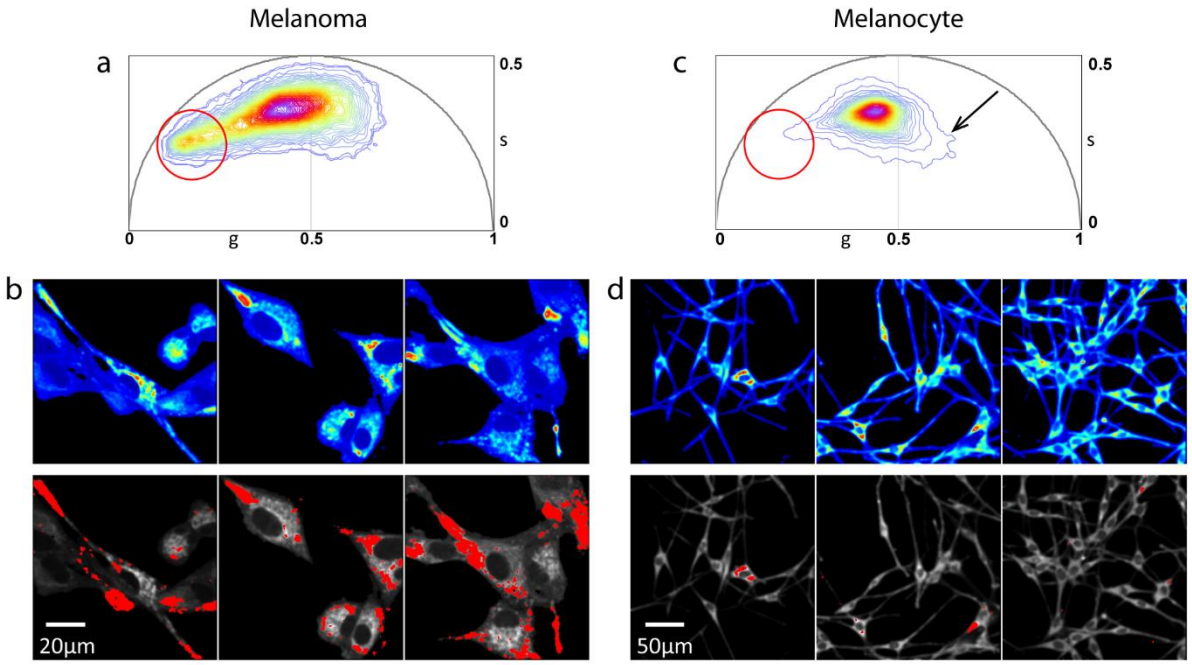

Fig 3.11 LLS in melanoma. (a) FLIM phasor distribution of SK-MEL-28 melanoma cell line. Red cursor selects LLS phasor distribution. (b) Top row shows three different areas of fluorescence intensity images of melanoma cells excited at 740nm. Bottom row shows the corresponding LLS FLIM map in red selected by cursor in a. (c) FLIM phasor distribution of melanocytes. Red cursor in the same position as (a) selects LLS phasor distribution. Black arrow points to short lifetime tail of melanin phasor distribution. (d) Top row shows three different areas of fluorescence intensity images of melanoma cells excited at 740nm. Bottom row shows the corresponding LLS FLIM map in red selected by cursor in (c).

FLIM-phasor of melanoma cell line SK-MEL-28 showed presence long lifetime cluster, Fig 3.11(a). Mapping this phasor distribution selected by red circle revealed coincidence of LLS signal with the granules present in the dendritic extensions on the melanoma cells, shown in red in Fig 3.11 (b) lower panel. FLIM phasor of melanocytes also displayed some LLS lifetime cluster, Fig 3.11 (c) though not as prominent as melanoma cell line. It should be noted that the field of view of the melanocytes are larger, which might pull the LLS cluster towards NADH FLIM phasor cluster. The shorter lifetime tail (pointed by black arrow) in Fig 3.11(c) is probably due to melanin which could be excited at 740nm[110].

3.4.2 Breast cancer

Methionine is an amino acid involved in protein biosynthesis. S-adenosyl methionine (SAM), a derivative of methionine, is a methyl donor and thus involved in methylation of proteins, lipid, DNA and RNA. It is known that majority of cancer cells depend of methionine metabolism for proliferation. This has been referred to as "methionine dependence" or "methionine stress sensitivity"[125,126]. Interestingly this phenomenon is not observed in non-cancer cells. Due to this, while non-cancer cells proliferate in growth media where methionine (Met+) is substituted by homocysteine (Met-Hcy+), which is its immediate metabolic precursor, methionine-stressed cancer cells stop proliferating. To investigate the metabolic changes associated with breast cancer cells cultured in Met-Hcy+ media, breast cancer cell line MDA-MB-468 and its methionine insensitive derivative cell line MDA-MB-468res-R8 was used. One of the important observation of this project was the presence LLS FLIM signal in the breast cancer cells which increased with Met-Hcy+ media replacement. FLIM was performed on MB468 and MB468res-R8 cells cultured in Met-Hcy+ media over the course of 48 hours. Phasor analysis shows a distinct shift along the oxidative stress axis towards the long lifetime on the universal circle [Fig 3.12(a)]. The center of mass of the phasor distribution is strongly shifted towards LLS fingerprint after 48 hours compared to control, especially in case of MB468. The LLS signal appeared to correspond to granular structures in the cytoplasm of the cells [Fig 3.12 (b)]. For quantifying this shift, the fraction of pixel with LLS signal was calculated for each condition. In normal Met+ culturing conditions, the average fraction of LLS in MB468 cells is 7 and 22 % in MB468res-R8 cells (Fig. 3.13). Immediately after media switch to Met-Hcy+, the fraction of LLS increases in MB468 to 25 % at 30 min and continues to increase over time to an average of 36 % at 48 h.

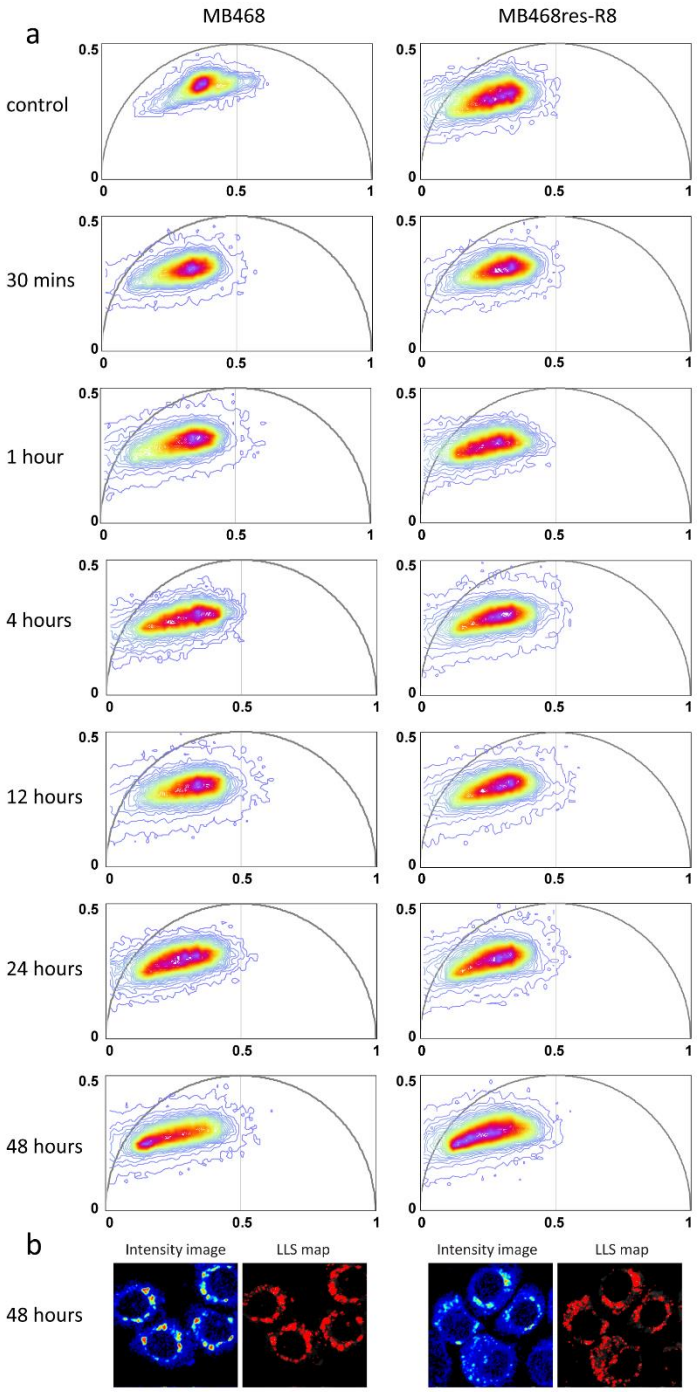

Fig 3.12 Methionine stress induces an increase in oxidative stress in breast cancer cell line MDA-MB-468 (MB468) and its methionine insensitive derivative cell line MDA-MB-468res-R8 (MB468res-R8) in homocysteine media. (a) FLIM phasor distribution of MB468 (left column) and MB468res-R8 (right column) cells in methionine media (control) and homocysteine media over the course of 48 hours. (b) Fluorescence intensity image and corresponding LLS FLIM map in red of MB468 and MB468res-R8 cells cultured in homocysteine media for 48 hours.

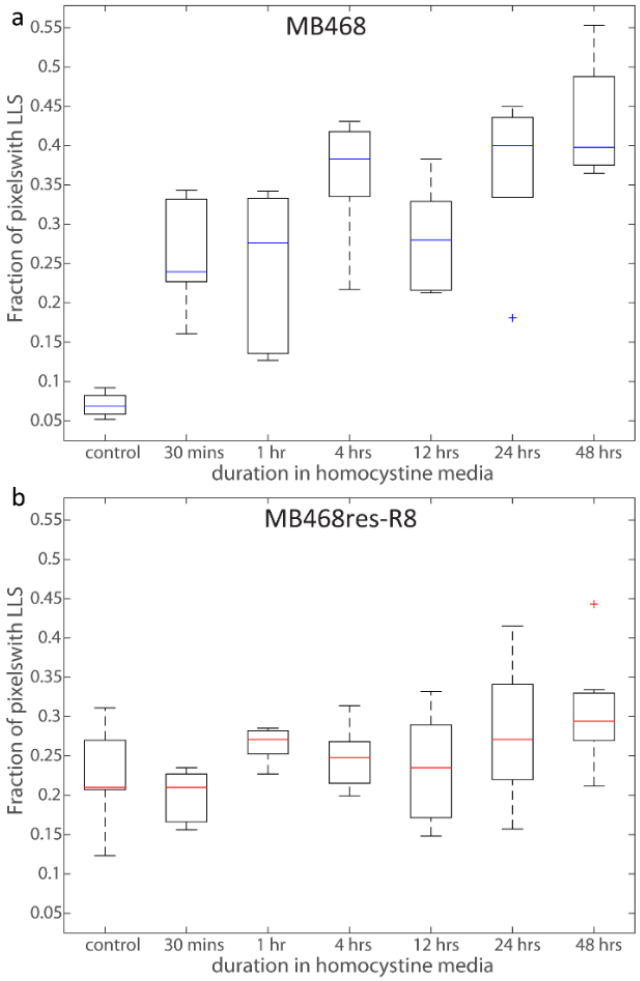

Fig 3.13 A boxplot representing the fraction of pixels with the LLS FLIM signature in MB468 (a) and MB468res-R8 (b) in methionine media (control) and homocysteine media over the course of 48 hours

In contrast, MB468res-R8 cells respond to the media shift with a 5 % average increase to 27 % LLS after 48 h. It is interesting to note the higher level of oxidized lipids in MB468res-R8 cells in Met+ as compared to MB468 cells and yet the striking increase observed in the MB468 cells over time in Met-Hcy+. This oxidative stress associated with Met-Hcy+ media is also supported by increasing levels of glutathione disulfide (GSSG) and a steep increase in

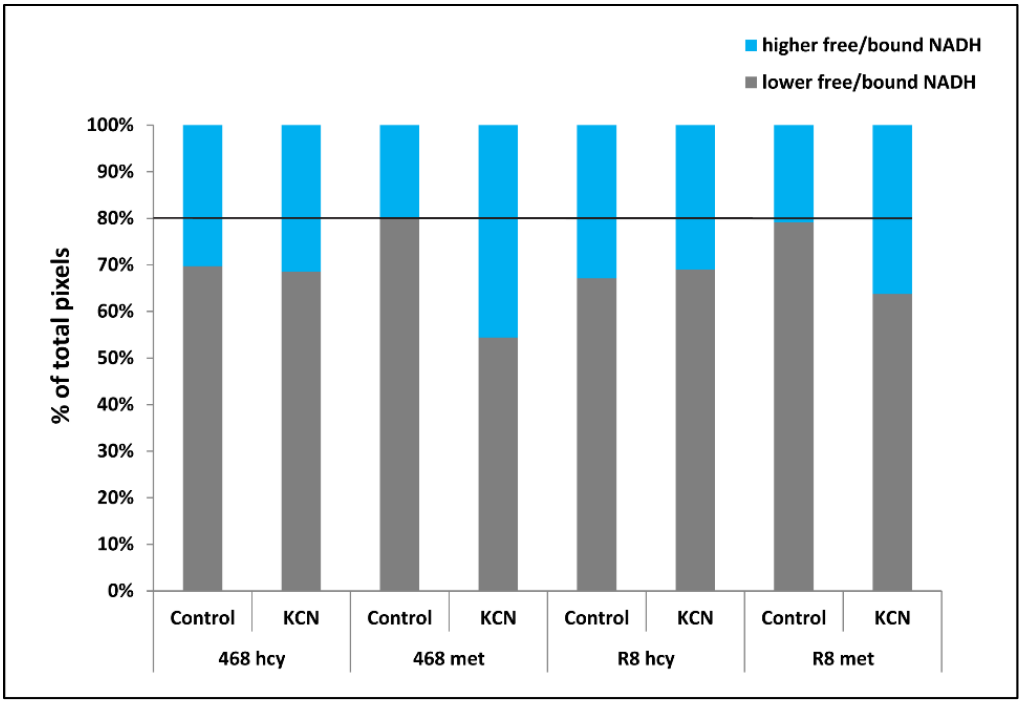

Fig 3.14 Homocysteine media induces a metabolic shift from oxidative phosphorylation to glycolysis. FLIM was performed on MB468 and MB468res-R8 cells cultured in Met+ or Met-Hcy+ for 48 hours with or without 4 mM and the NADH phasor distribution was divided into higher free/bound NADH (cyan) and lower free/bound NADH (grey) groups. Percentage of pixels in each group was calculated from images of each group and plotted. The black line indicates the average percentage of lower free/bound NADH ratios of MB468 (80%) and MB469res-R8 (79%) cells cultured in in Met+, KCN (-).

reduced form of glutathione (GSH). GSH is an antioxidant which is oxidized to GSSG in the process of combating oxidative stress.

Furthermore, FLIM-phasor analysis of NADH revealed 70 % of the MB468 and 64 % of the MB468res-R8 had higher free/bound NADH ratio when Met+ media was replaced with Met-Hcy+ after 48 hours (Fig 3.14). This result indicates decrease in cellular respiration. Similar result was obtained when Met+ cultured cells where treated with mitochondrial inhibitor potassium cyanide (KCN) as shown in Fig 3.14. This down regulation of oxidative phosphorylation in Met-Hcy+ was corroborated by oxygen consumption rate (OCR)

measurements with extracellular flux (XF) analyzer for mitochondrial function analysis as described in Chapter 1, section 1.2[126].

3.5 Discussion

In this work we identified a fluorescent species with unique long lifetime properties (around 7.8ns) which is distinct from the common NADH lifetime in cells (1-2ns). We present results showing autofluorescent long lifetime species (LLS) linked to products of lipid oxidation by ROS, and hence potential biomarkers for oxidative stress. Lipids, per se, are non-fluorescent, however, oxidized lipids can be[127]. We found that most of the fluorescence arises from lipid droplets with granular structure. This long lifetime distribution found in cells represents a species different from free/bound NADH. In this work we grouped both nuclear and cytoplasmic NADH as a single distribution, although phasor analysis can separate NADH from the two sub cellular regions. To identify the source of fluorescence in the LLS, we performed FLIM imaging of freshly excised visceral and subcutaneous WAT from old female mice. We found the LLS phasor distribution from the adipocyte lipid droplets to fall on the universal circle at 7.8ns. This indicates the existence of a pure chemical species in the lipid droplet, as it is known that lifetime distribution of pure species with single exponential decay would lie on the universal circle[82]. This also confirms the existence of a species separate from NADH in our sample. NADH distribution in biological samples generally falls on the metabolic trajectory, the line joining position of pure free NADH (0.4ns) and pure protein bound NADH (3.4 ns)[58]. This metabolic trajectory and the LLS signature on the universal circle form a triangle on the phasor plot. From phasor algebra, a pixel in the image where LLS can coexist with the NADH distribution will have a position inside this triangle. Hence

using the phasor approach, it was possible to distinguish these separate populations and map them back to the images to reveal their spatial locations.

To investigate the unique LLS in cells and their association with lipid droplets, we used HeLa cells fed with oleic acid to stimulate the formation of lipid droplets, and we observed the LLS signal arising precisely from the lipid droplets. In these samples, the linear combination of the long lifetime components due to oxidized lipids species and NADH autofluorescence give rise to a separate, easily identifiable cluster of phasors. This distribution cluster falls along the line joining the center of NADH distribution and LLS FLIM signature (7.8ns) on the universal circle. We propose this line as the new oxidative stress axis on the phasor plot. Mapping the lifetime phasors back onto the images, we observed the lipid droplet with LLS were present in the cytoplasm of the HeLa cells. In rare occasions the LLS were also observed in a few cells grown in normal media. Interestingly, these LLS containing lipid droplets were mostly localized towards the membrane of the cells. We explored the fluorescence emission characteristics of the LLS by employing spectral phasors[93]. By comparing FLIM phasor and spectral phasor analysis of both visceral and subcutaneous WAT, we found the regions with the LLS FLIM signature to have distinct emission spectral properties than NADH. The LLS spectral phasor distribution was centered on 497.4 nm for visceral WAT and 496.2 nm for subcutaneous WAT. These were separable from NADH spectral phasor distribution centered on 487nm for both tissues.

To identify the cellular location of the intrinsic fluorescent species, we imaged tissue and cells using THG microscopy along with FLIM. THG signal arises from the interface between the lipid droplets and their surroundings thus revealing the spatial location of the droplets.

Coupling the two modalities of label-free imaging, we verified the co-localization of LLS within the lipid droplets of adipocytes in visceral WAT. A 3D reconstruction of FLIM and THG images through 72μm depth of visceral WAT exhibited LLS signal throughout the lipid droplets of the adipocytes surrounded by strong THG signal from the periphery of the droplets. This is where the FLIM and THG signals overlapped.

We found less prominent LLS FLIM phasor cluster in brown adipose tissue excised from the same animal. This could be due to the presence of ROS induced oxidative stress associated with accumulated fat WAT, while BAT is known to burn excess fat to prevent obesity.

Additionally, to test the chemical origin of the fluorescence signal we performed FLIM on oleic acid fed HeLa cells followed by CARS imaging of the same cells. This was possible due to the label-free and non-invasive nature of both imaging techniques. CARS images revealed a large amount of lipid droplets in the samples, supporting the increase in LLS phasor distribution along the oxidative stress axis. These results once more substantiate our hypothesis of association of LLS with lipid oxidation products. Interestingly, not all lipid droplets detected both by CARS and THG have the autofluorescence long lifetime signature.

Confocal Raman spectroscopy allowed non-invasive chemical analysis of our biological samples. We employed this technique to analyze the locations where the long lifetime components were detected. Fixed HeLa cells with oleic acid induced lipid droplet were imaged by FLIM, and Raman spectra were acquired subsequently from granules with LLS FLIM signature. The Raman spectra of the regions with LLS displayed the Raman signatures indicative of esterified oleic acid, characteristic from triglycerides in the lipid droplets[115,116 128,129].

Lipid droplet associated autofluorescence has been identified previously. These include lipofuscin granules and retinosomes. Lipofuscin granules are found in human retinal pigment epithelial (RPE) cells, fibroblasts and other types of cells and have also been reported as oxidative stress marker[130,131]. Stringari et al reported existence of long lifetime species (about 8ns) in human embryonic stem cells and co-localized these lipid granules with 4,4-difluoro-1,3,5,7,8-pentamethyl-4-bora-3a,4a-diaza-s-indacene(BODIPY493/503), which is a stain for neutral lipids[58]. They established that the autofluorescent species with long lifetime were not associated to lipofuscin, which has a much shorter lifetime[132]. This ascertains the LLS reported in this study are not related to lipofuscin. Retinosomes are lipid droplet containing retinol, retinoic acid, and retinol ester which are also sources of autofluorescence[133,134]. The lifetime fingerprint of retinoid and retinoic acid with fluorescent lifetime shorter than LSS has been shown to be in a different spatial location of the lifetime phasor plot compared to the lipid droplet associated LLS reported here[90]. Furthermore, retinol and retinoic acid have a very prominent Raman band in the 1590-1600cm^{-1} range that was not observed in our Raman spectra[135].

Even though MPM still has limited application in clinical settings, it improves penetration for deep tissue imaging and in vivo animal models. Furthermore, as shown in this work, we can apply this imaging technique to live cells and freshly excised tissue.

ROS and oxidative stress are related to a myriad of pathological conditions including diabetes mellitus, obesity, inflammation, cancer, cardiovascular diseases, lung diseases and neurodegenerative diseases[102–108] . Its role in pathogenesis has made it an important candidate for research on disease development, diagnosis and treatment routes. Thus a

biomarker for oxidative stress m be used to elucidate pathways of disease development. Autofluorescence of oxidized lipid has the potential to be such a biomarker and in this work we show a unique detection approach by employing FLIM imaging.

Furthermore, we show application of LLS-FLIM to detect oxidative stress associated with cancer. FLIM phasor revealed increased amounts of LLS phasor signature in melanoma cells compared to normal melanocytes. This can be expected as melanoma is essentially a ROS driven cancer. Proto-oncogene pathways in melanoma is activated when ROS inhibits phosphatase and tensin homolog (PTEN) phosphate activity. PTEN is a tumor suppressor and its inhibition by ROS initiates AKT (Protein kinase B) pathway often associated with cancer[124]. Some amount of LLS signal observed in normal melanocyte can be due to the fact that melanocytes have higher amounts of ROS in presence of melanin[122]. LLS signal was also observed in breast cancer which was elevated with 'methionine stress'.

The technique could unveil unprecedented opportunity for *in vivo* oxidative stress detection. The advantages of intrinsic fluorophore, especially for imaging in tissues, cannot be reached by external fluorescent dyes. The probe might not be equally distributed in the cellular location, or might not have reached deep within the tissue. This technique could possibly be further extended to detect oxidative stress in intact mice organs or to monitor stress as a function of time. Perhaps formation of the granules and subsequent expulsion could also be tracked to attain a better understanding of the cell's reaction to stress.

In conclusion, the long lifetime species FLIM signature of oxidized lipids detected using the phasor approach is a promising, non-invasive tool to detect oxidative stress in biological systems. As far as we know, this is the first time a label-free fluorescent technique has been

proposed for this purpose. As shown in this work, phasor analysis of FLIM allows an efficient way to uniquely identify, intrinsic, autofluorescent marker of oxidative stress in cell cultures as well as tissue samples.

3.6 Chapter summary

Presence of reactive oxygen species (ROS) in excess of normal physiological level results in oxidative stress. This can lead to a range of pathological conditions including inflammation, diabetes mellitus, cancer, cardiovascular and neurodegenerative disease. Hence a probe for detecting oxidative stress would be of immense clinical importance. However, there is a dearth of non-destructive techniques to measure oxidative stress *in vivo*. In this chapter we present a spectroscopic method to identify oxidative stress in cells and tissues by fluorescence lifetime imaging. We identified this as fluorescent product of lipid oxidation by ROS. These species with a characteristic long lifetime (LLS) had granular structures and were correlated to lipid droplets in the biological sample being imaged. Recognition of this endogenous biomarker of oxidative stress enables label free imaging. Unlike commercially available ROS-specific fluorescent indicators, this technique circumvents the requirement of administering any external substance into the biological system. To corroborate our hypothesis that these species are products of lipid oxidation by ROS, we correlate the spectroscopic signals arising from lipid droplet by combining FLIM with third harmonic generation (THG) imaging microscopy and coherent anti-Stokes Raman scattering (CARS) microscopy which are established techniques for selective lipid body imaging. Further, we performed spontaneous Raman spectral analysis at single points of the sample which provided molecular vibration information characteristics of lipid droplets. Finally, we show application of this technique to measure oxidative stress associated with cancer. This label-free, non-invasive FLIM-phasor method is a promising imaging technique for oxidative stress detection in biological systems.

Chapter 4

Metabolism and oxidative stress in hiPS cardiomyocytes

Chapter overview: In the previous chapter we established two-photon fluorescence lifetime imaging (FLIM) based technique to detect oxidative stress. In this chapter we combine the powerful label-free technique with metabolic imaging to assess human induced pluripotent stem cell-derived cardiomyocytes (hiPS-CM) and study their response to pathological stimuli.

This work has been published in the following paper:

Datta, R., Heylman, C., George, S. C. & Gratton, E. Label-free imaging of metabolism and oxidative stress in human induced pluripotent stem cell-derived cardiomyocytes. Biomedical Optics Express 7, 1690 (2016).

4.1 Introduction

Many drugs showing promise in preclinical trials fail during clinical development due to the emergence of cardiac side effects[136–138]. The development of in vitro platforms that accurately mimic the biology of human cardiac cells provide a plausible model for high-throughput drug screening to detect potential cardiotoxicity before wide spread human use. The emergence of human induced pluripotent stem cell technology has expanded the possibilities for sourcing human cardiomyocytes [139,140]. However, there is a need for non-destructive techniques to visualize the biology and drug response of such in vitro human induced pluripotent stem cell-derived cardiomyocyte (hiPS-CM) models for drug screening.

Novel microscopy and analysis methods can serve as powerful tools to study and monitor the physiology of such systems. Indices of metabolism and oxidative stress are particularly relevant in cardiac pathologies and response to drugs[141,142]. In this work, we employ two-photon fluorescence lifetime imaging microscopy (FLIM) to assess the metabolic state and oxidative stress in hiPS-CMs.

FLIM of endogenous fluorophores such as reduced Nicotinamide adenine dinucleotide (NADH), collagen, retinol, melanin, and flavins have been employed as convenient, intrinsic, label-free assessment of metabolism and other physiological functions of biological samples[42,43,57]. The advantage of this technique is its non-invasiveness. Use of intrinsic fluorophores circumvents administration of external fluorescent dyes, thus avoiding associated nonspecific binding, toxicity, and interference with the biochemical and physiological functions of the biological system being imaged.

FLIM of autofluorescent NADH can serve as a tool to study metabolism due to the extreme sensitivity of fluorescence lifetime to molecular conformations and the fluorophore's surrounding environment. Also, unlike intensity based imaging, lifetime measurements are independent of concentration. Hence, NADH FLIM is extensively employed as an endogenous biomarker for metabolic imaging [42,43,57,58,99,143–145]. The reduced form of NADH is produced during glycolysis and Krebs cycle. During oxidative phosphorylation, it is oxidized to NAD+ by donating electrons to the electron transport chain, which are ultimately accepted by oxygen[42,43]. In the case of anaerobic glycolysis, NAD+ is converted to NADH and oxidative phosphorylation is diminished. This decreases the oxidation of NADH, resulting in an overall increase of free (not bound to protein) NADH. Thus, the reduction-oxidation pair

NADH:NAD+ serves as an indicator of balance between oxidative phosphorylation and glycolysis. Bird, et al. demonstrated a correlation between the redox ratio NADH:NAD+ and the ratio of free to protein bound NADH, which is advantageous in fluorescent based technique because unlike NADH, NAD+ is not fluorescent[146].

Owing to self-quenching, the fluorescence lifetime of NADH in the free state is significantly lower (~0.4ns) compared to protein bound NADH. For example, the lifetime of NADH bound to lactate dehydrogenase (LDH) is 3.4ns[9]. Hence, FLIM can easily differentiate between free and protein bound forms of NADH. In this work, we exploit these properties to assess metabolic activity of hiPS-CMs by FLIM of NADH. NADH was excited at two-photon excitation (TPE) of 740nm and fluorescence signal was collected between 420 – 500 nm. We used the phasor analysis of FLIM to create a map of free/bound NADH[82]. The phasor approach to FLIM for metabolic imaging has been previously applied for various studies, including cancer metabolism and metabolic shifts associated with stem cell differentiation[58,99]. This method simplifies the analysis of FLIM data, eliminating the requirement for fitting the fluorescence decay at each pixel. The technique has been described in details in Chapter 2. Briefly, data from each pixel are Fourier transformed to obtain the corresponding phasor and the 2-D histogram of the phasor is plotted on the phasor plot. This allows analysis of different lifetime phasor clusters which can be can be mapped back onto the image to create the FLIM map.

Here we employed NADH phasor-FLIM to detect the metabolic response of hiPS-CM to hypoxia. An uninterrupted oxygen supply is essential for cardiac tissue to meet the high metabolic demands and a lack of oxygen can have deleterious effects, leading to numerous

pathological conditions. This has led to a growing interest in the effect of hypoxia[147–149]. Using the phasor approach to FLIM, along with metabolic shifts, we also identified an increase in a long lifetime species (LLS) with characteristic clustering in the lifetime phasor plot. Recently, we showed correlation of LLS to products of lipid oxidation formed by reactive oxygen species (ROS) using techniques like third harmonic generation (THG) imaging microscopy, coherent anti-Stokes Raman scattering (CARS) microscopy, and Raman spectroscopy[9]. To correlate the observed LLS to lipid droplets in hiPS-CMs, we performed stimulated Raman scattering (SRS) imaging microscopy. CH_2 stretching vibrations, which are abundant in fatty acid chains, are easily excited and detected by SRS microscopy making it a useful technique to identify lipid bodies[150]. The LLS species were also detected by FLIM in hiPS-CMs treated with the anti-cancer drug *cis*-Diammineplatinum(II) dichloride (cisplatin) and the antiviral compound 3′-Azido-3′-deoxythymidine (AZT), both of which are known to produce oxidative stress and cardiotoxicity[151,152] .

This study describes the use of a potentially powerful, non-invasive, label-free optical imaging technique for assessing the metabolic status and oxidative stress in cardiomyocytes. We demonstrate the sensitivity of this imaging technique to detect shifts in hiPS-CM metabolism and the generation of LLS in response to stimuli known to induce such effects like hypoxia and cardiotoxic drugs.

4.2 Materials and methods

4.2.1 Instrumentation

FLIM was performed on a Zeiss LSM 710 microscope (Carl Zeiss, Jena, Germany) using a 40x, 1.2 N.A. water immersion objective, (Carl Zeiss, Oberkochen, Germany) coupled to an 80MHz multiphoton excitation laser source, Titanium:Sapphire MaiTai laser (Spectra-Physics, Mountain View, CA). 2PE (2 photon excitation) excitation of NADH and LLS was carried out at 740nm. Image scan speed was 25.21 µs/pixel with an image size of 256 × 256 pixels. A dichroic at 690 nm was employed to separate excitation from emission signal. A bandpass emission filter 460/80nm (Semrock, Rochester, NY) coupled to a photomultiplier tube (H7422P-40, Hamamatsu, Japan) was used as the microscope external detector port photo-sensor unit. FLIM data was acquired using A320 FastFLIM FLIMbox (ISS, Champaign, IL). For each image, 60 - 70 frames were collected and integrated for FLIM analysis. SimFCS software (LFD, Irvine) was used for frequency domain FLIM data acquisition. For calibrating the FLIM system, Rhodamine 110 with known lifetime of 4ns was measured for every experiment. All the (g, s) coordinate system used to mention phasor cursor coordinates in this article used the first harmonic phasor plots at 80Mhz (repetition rate of the laser).

Confocal imaging of ROS indicator CellROX was performed on the same Zeiss LSM 710 microscope (Carl Zeiss, Jena, Germany) and with an excitation of 633nm. Fluorescence signal was collected in the range 640-740 nm. The laser excitation power and detector gain was kept constant for all measurements.

Stimulated Raman scattering (SRS) signals were obtained as previously described here[153]. Briefly, a Stokes beam fixed at ~9400 cm^{-1} and a pump beam tuned to the wavelength of interest (2800 – 3050 cm^{-1}) were overlapped both temporally and spatially and sent into a laser scanner (Fluoview 300, Olympus, Center Valley, Pennsylvania), attached to an inverted microscope (IX71, Olympus). The combined beams were then focused through a 20×, 0.75 NA objective lens (UplanS Apo, Olympus) onto the sample. SRS images were obtained by detecting the stimulated Raman loss of the pump beam with a photodiode (FDS1010; Thorlabs, Newton, New Jersey). The average combined power of Stokes and pump beams at the specimen was kept under 50 mW throughout this study to minimize sample photodamage.

4.2.2 hiPS-CM differentiation and culture

hiPS-CMs were differentiated from the wtc11 line of human induced pluripotent stem (hiPS) cells generously donated by Dr. Bruce Conklin [154]. hiPS cells were differentiated into cardiomyocyte like cells following previously established protocol which entails culture in Roswell Park Memorial Institute (RPMI) medium (Life Technologies, 22400–071) supplemented with B-27 without insulin (Life Technologies, A1895601) [155]. The protocol includes supplementing media with 12 μM CHIR99021 (Selleckchem, S2924) for 24 hours after which it is removed on day 0. Media is supplemented with 5 μM IWP2 (Tocris, 3533) on day 3 which is then removed on day 5. On day 7, the media is supplemented with insulin, and after that day the cells were fed RPMI/B-27 (+) insulin (Life Technologies, 17504–044) every 2–3 days for the duration of the experiment. Approximately between days 12–15, the cells started beating spontaneously. hiPS-CM drug exposure and measurements were

performed on days 22-30. Cells were qualitatively confirmed to be beating throughout differentiation and culture (including post-hypoxia exposure and post-drug exposure)

4.2.3 Cyanide treatment

KCN (Sigma, St. Louis, MO) in phosphate buffered saline (PBS) (Sigma-Aldrich, St. Louis, MO) was added to the cell culture media to reach a final concentration of 4mM. FLIM was performed on the cells before the treatment and the same cells were imaged 2-3 mins after addition. During FLIM measurement temperature of 37º C and 5% CO_2 was maintained.

4.2.4 Hypoxia exposure

For hypoxia, the cells were exposed to a gas mixture (1% O_2, 5% CO_2, 94% N_2) in a hypoxic microchamber (Stem Cell Technologies, Vancouver, BC, Canada) and were incubated at 37º C for either 24 or 48 hours. During FLIM imaging, the cells where quickly transferred to the microscope stage incubation chamber which was flooded with the same gas mixture. A temperature of 37º C was maintained throughout the imaging.

4.2.5 Drug treatments

AZT (Sigma-Aldrich, St. Louis, MO) in nanopore filtered water was added to the hiPS-CMs culture media to reach a final concentration of 50µM. Cisplatin (Sigma-Aldrich, St. Louis, MO) was added to media, also to a final concentration of 50µM. Temperature of 37º C and 5% CO_2 was maintained during imaging.

4.2.6 In vivo staining

To assess the concentration of reactive oxygen species (ROS), hiPS-CMs were stained with ROS indicator, CellROX Deep Red (ThermoFisher Scientific, Waltham, MA), at a final concentration of 5uM after treatment (cisplatin, AZT, or control). Cultures were incubated with CellROX for 30 min at 37º C, then washed 3X with PBS, and imaged immediately.

4.2.7 Data analysis

All the FLIM data was analyzed using SimFCS software developed at the Laboratory for Fluorescence Dynamics (LFD, UC Irvine). For statistical analysis in section 2.2, the Student's t-test was used to determine the significance and considered positive for $p < 0.05$. In section 2.3, statistical significance was determined by an ANOVA with post-hoc Bonferroni correction using MATLAB software.

4.3 Results

4.3.1 Detection of metabolic shift in response to cyanide

Cyanide is known to block the electron transport chain by inhibiting cytochrome oxidase function[156]. This reduces NADH oxidation causing an increase in the redox ratio, NADH/NAD+. An increase in NADH fluorescence has been reported in cardiomyocytes treated with cyanide[157]. To test the sensitivity of the FLIM-phasor technique to detect metabolic shifts in hiPS-CMs, we performed NADH FLIM of hiPS-CM treated with 4mM potassium cyanide (KCN). Fig. 4.1(a) shows the phasor distribution of hiPS-CMs before and after treatment with KCN. The phasor distributions lie along the metabolic trajectory (blue

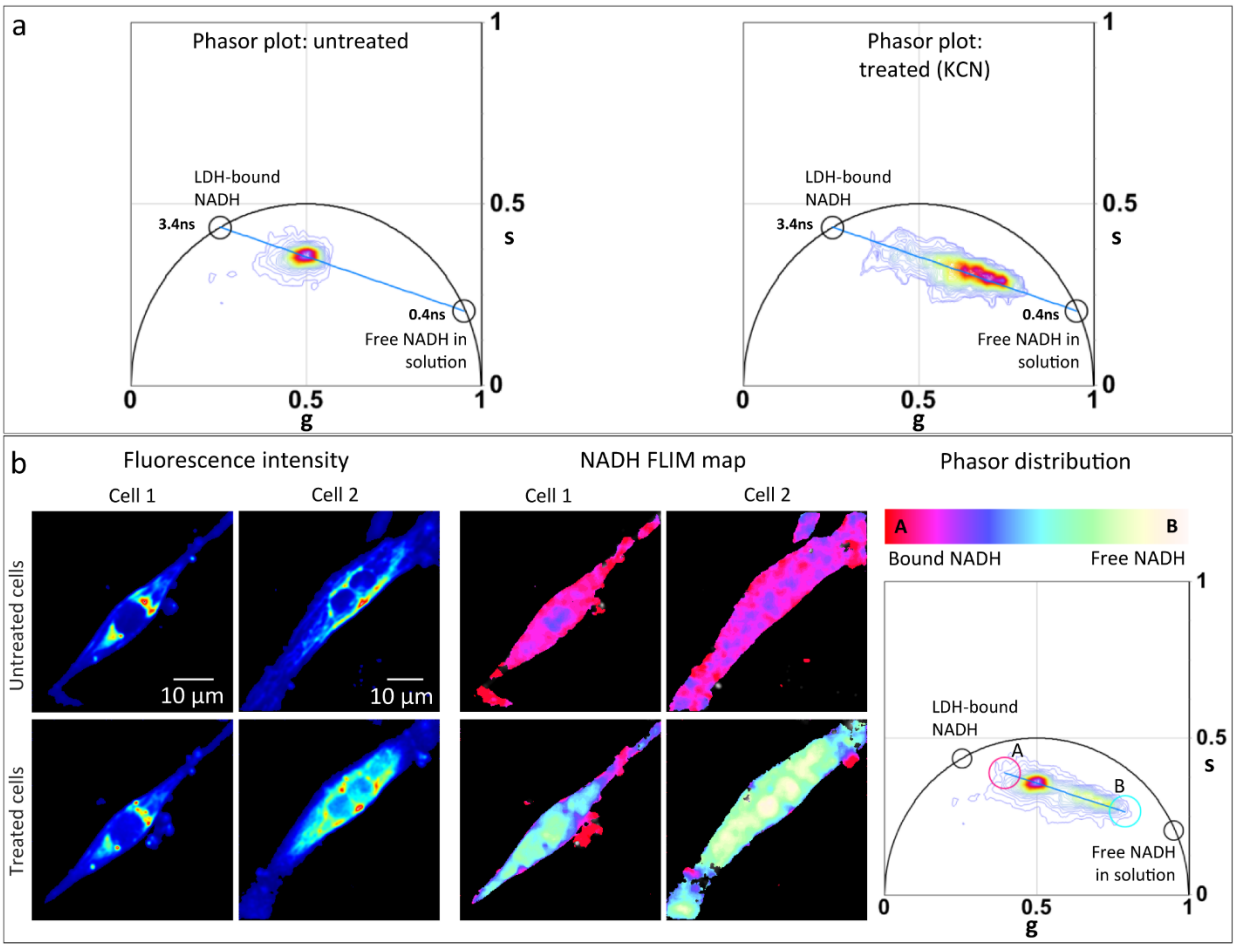

Fig 4.1 FLIM detects shift of metabolism to glycolysis when subjected to potassium cyanide (KCN). (a) Lifetime phasor distribution of untreated (left panel) and 4mM KCN treated (right panel) hiPS-CMs. Black circles show phasor fingerprint of pure free NADH in solution (0.4ns) and protein lactate dehydrogenase bound NADH, 'LDH-bound NADH' (3.4ns). Blue line indicates the metabolic trajectory on phasor plot. (b) Fluorescence intensity image (left panel) of two hiPS-CMs (cell 1 and cell 2) before (top row) and after (bottom row) treatment with 4mM KCN excited at 740nm. Middle panel shows the NADH FLIM map of cell 1 and cell 2 before (top row) and after (bottom row). Right panel shows the total phasor distribution of the treated and untreated cells. The color scale white/yellow to red/pink represents linear increase of free to protein bound NADH ratio. To create the NADH FLIM map, this color scale was applied from point A to B of the phasor distribution, dividing it into 32 levels.

line) extending between the phasor fingerprint of free NADH (0.4ns) and protein (LDH) bound NADH (3.4ns). For all the phasor plots in figure 1, the experimental points lie along the line from the point at 3.4ns to the point at 0.4ns, on the universal circle. According to the law of linear combination of phasors, the two points on the universal circle are the

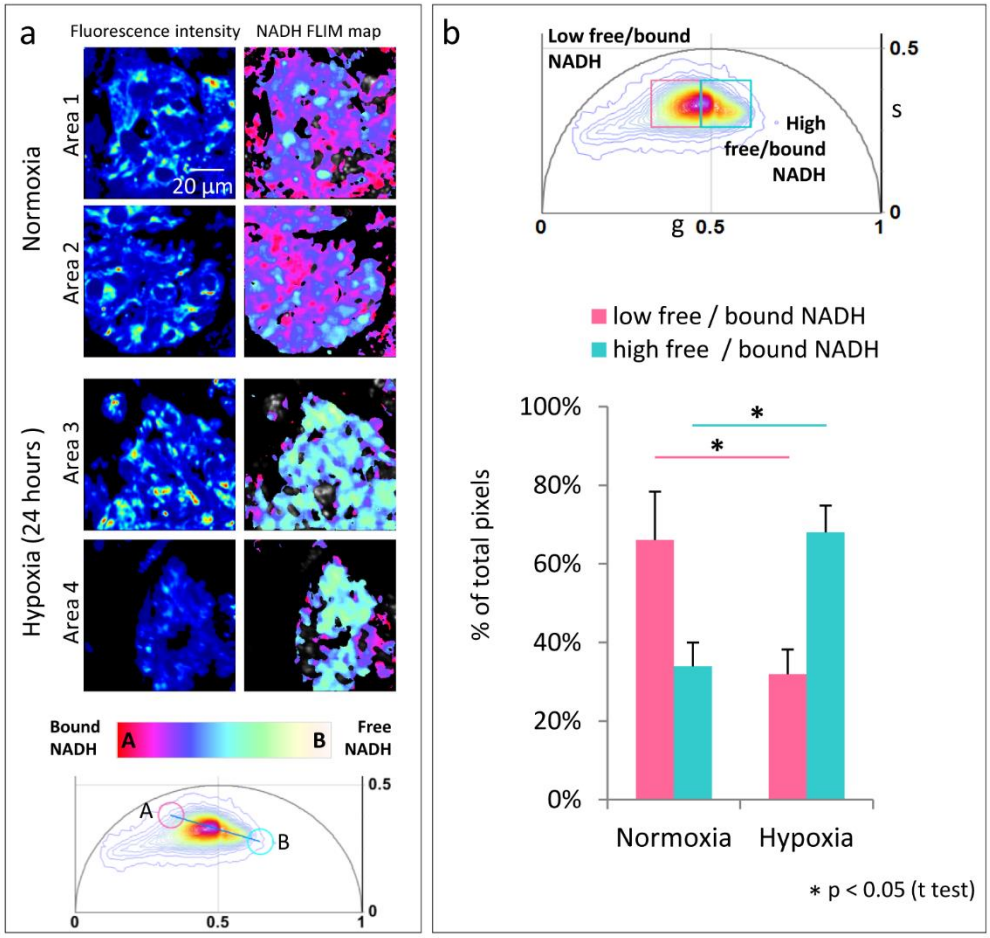

Fig 4.2 Shift in metabolism for 24 hours of hypoxia (a) Fluorescence intensity image (left panel) of clusters of hiPS-CMs under normal 20% oxygen condition (Area 1 and Area 2) and hiPS-CM under hypoxia, 1% oxygen (Area 3 and Area 4). Left panel shows the corresponding NADH FLIM. The color scale white/yellow to red/pink represents linear increase of free to protein bound NADH ratio between position 'A' and 'B' shown on the phasor plot (bottom panel). (b) Quantitative representation of the fraction of pixels with phasors within the 'low free/bound NADH' (pink) window and the 'high free/bound NADH' (cyan) window (top panel) The windows divide the NADH phasor distribution equally at the center of mass of the NADH phasor distribution of the control cells (normoxia). For the statistical analysis, phasor distribution is obtained from 3 three different regions of hiPS-CM clusters about 10 cells each for the two oxygen conditions. The error bars show the standard deviation calculated over average value obtained from each image.

extrapolated single lifetime components for the bound and free NADH forms, respectively. The phasor distribution of the treated cells is shifted towards the position of free NADH, indicating a higher free/bound NADH ratio. Fig. 4.1(b) shows the total phasor distributions of two hiPS-CMs before and after treatment. The linear decrease in free/bound ratio of NADH

has been pseudocolored from white/yellow to red/pink and mapped on the corresponding fluorescence intensity images to create the NADH FLIM map as shown in Fig 4.1(b). The color-scale extends between positions 'A' and 'B' [Fig. 4.1(b)] which represents two extreme positions of the NADH phasor distribution, i.e., phasors with lowest free/bound NADH ratio and highest free/bound NADH ratio from these particular samples. The cells after KCN treatment display yellow-cyan colors in comparison to the pink-red color map before, consistent with an increase in free/bound NADH ratio after treatment. The NADH phasor shift towards position of free NADH fingerprint establishes the sensitivity of the system to detect shifts in the free/bound NADH ratio and thus metabolic changes in cardiomyocytes.

4.3.2 FLIM detects metabolic response to hypoxia

In hypoxic conditions, cells switch to anaerobic glycolysis for energy production. Using the FLIM-phasor technique, we imaged this alteration of cardiac metabolism by subjecting clusters of hiPS-CMs to hypoxia. Fig. 4.2 shows NADH FLIM map of hiPS-CM clusters exposed to normoxia (20% oxygen, normal room oxygen concentration) and hypoxia (1% oxygen) for 24 hours. These oxygen conditions were maintained during FLIM imaging. Fig. 4.2(a) shows the fluorescence intensity and pseudocolored NADH FLIM map of hiPS-CM clusters maintained for 24 hours in normoxia (Area 1 and Area 2) and hypoxia (Area 3 and Area 4). The NADH FLIM map shows distinct difference between hiPS-CM clusters in normoxia and hypoxia with higher free/bound NADH ratio in the latter condition, clearly indicating the glycolytic switch. Fig. 4.2(a) bottom panel shows the corresponding phasor distribution and the positions (A' and B') between which the color scale was applied to divide the phasor distribution into 32 levels. Fig. 4.2(b) top panel shows phasor distribution of three different

regions of hiPS-CM clusters of about 10 cells each for normoxia and hypoxia. For quantitative analysis, the NADH lifetime phasor distribution was divided into two windows: 'high free/bound NADH' (cyan square, center = (0.54, 0.33), side = 0.14) representing higher free/bound NADH ratio while 'low free/bound NADH' (pink square, center = (0.398, 0.33), side = 0.14) representing lower free/bound NADH ratio. The windows divide the NADH phasor distribution at the center of mass of the NADH distribution of the control (normoxia) condition such that each window enclosed 50% of the points. The fraction of pixels in all the acquired images whose corresponding phasor lies within each window was calculated and plotted [Fig. 4.2(b)]. Comparing the two oxygen conditions, we found the increase of pixel percentage in the 'high free/bound NADH' window and decrease in the 'low free/bound NADH' wind ow in hypoxia to be statistically significant.

4.3.3 LLS produced in hypoxia indicating oxidative stress

Interestingly, the phasor analysis of the hiPS-CMs in hypoxia when compared to cells subjected to equal duration of normoxia shows presence of long lifetime species (LLS) with characteristic lifetime phasor fingerprint. LLS is indicative of oxidative stress, as previously described[9]. Fig. 4.3(a) shows hiPS-CMs in normoxia, 24 hours hypoxia, and 48 hours hypoxia. LLS FLIM map (in red) has been created by the LLS window on the phasor plot [Fig. 4.3(b)], which selects phasors with the characteristic LLS lifetime. These areas have granular appearance like lipid droplets similar to the previous observation[9]. Fig. 4.3(a) bottom row shows the corresponding individual phasor distribution. In comparison to normoxia, the long lifetime tail of the phasor distribution moves along the oxidative stress axis shown as

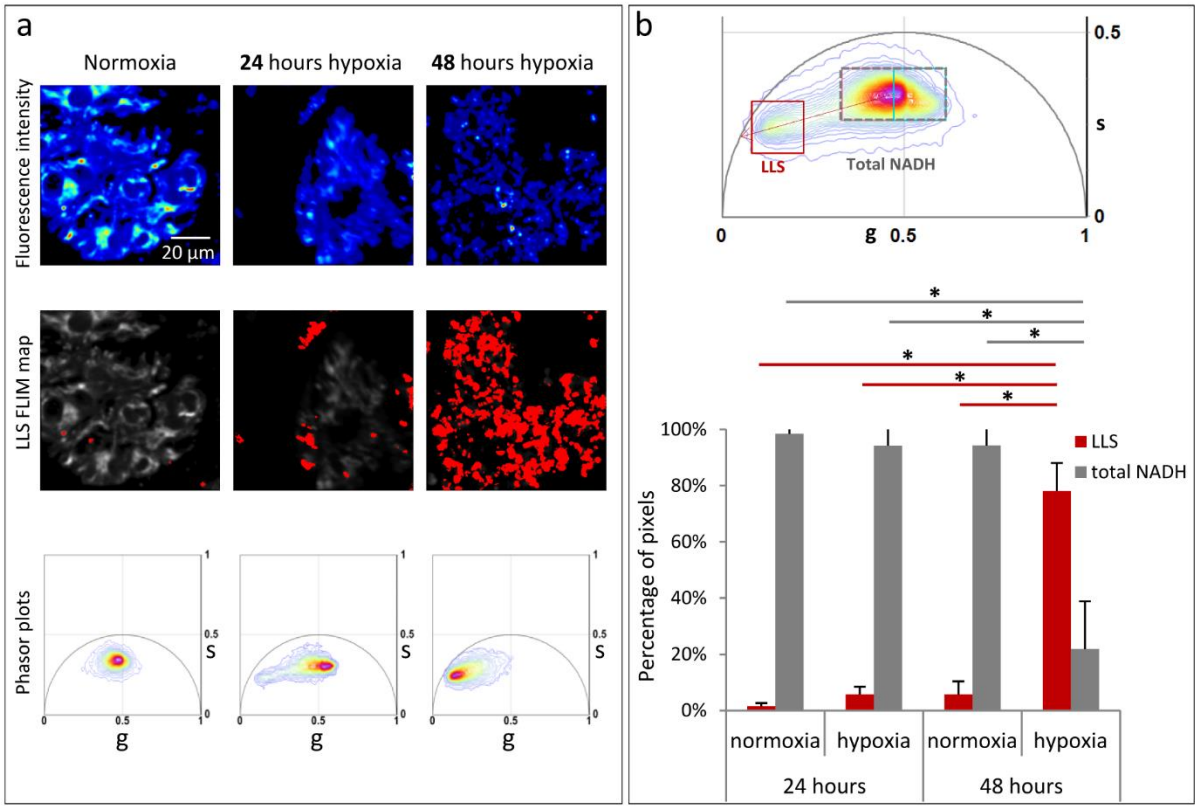

Fig 4.3 Significant increase in long lifetime species (LLS) with hypoxia. (a) Top row panels shows fluorescent intensity image of hiPS-CM clusters under normoxia, 24 hours hypoxia, 48 hours hypoxia. Middle row panels show LLS FLIM map (in red) created by the LLS window in (b) top panel. Bottom row shows the corresponding individual phasor plots. (b) Top panel is the phasor distribution of 3 three different regions of of hiPS-CM clusters about 10 cells each for normoxia, 24 hours hypoxia, 48 hours hypoxia conditions. Gray dotted window selects the total NADH distribution which covers the total area within pink and cyan windows of Fig 2 (b). LLS window (red square) selects the LLS phasor distribution. Red dotted arrow indicated the oxidative stress axis. Bottom panel shows quantitative representation of the percentage pixels with lifetime phasors within the 'Total NADH' window (gray dotted rectangle) and LLS phasor window (red square) of hiPS-CMS under normoxia, 24 hours hypoxia, and 48 hours hypoxia. The error bars show the standard deviation calculated over average value obtained from each image. Statistical significance was computed by ANOVA test with Bonferroni correction.

red dotted line in Fig 4.2(b), towards pure LLS fingerprint on the universal curve (7.8ns) in the hypoxic condition[9].

Fig. 4.3(b) top panel is phasor distribution of three different regions of hiPS-CM clusters of about 10 cells each for the four conditions: 24 hours normoxia, 24 hours hypoxia, 48 hours

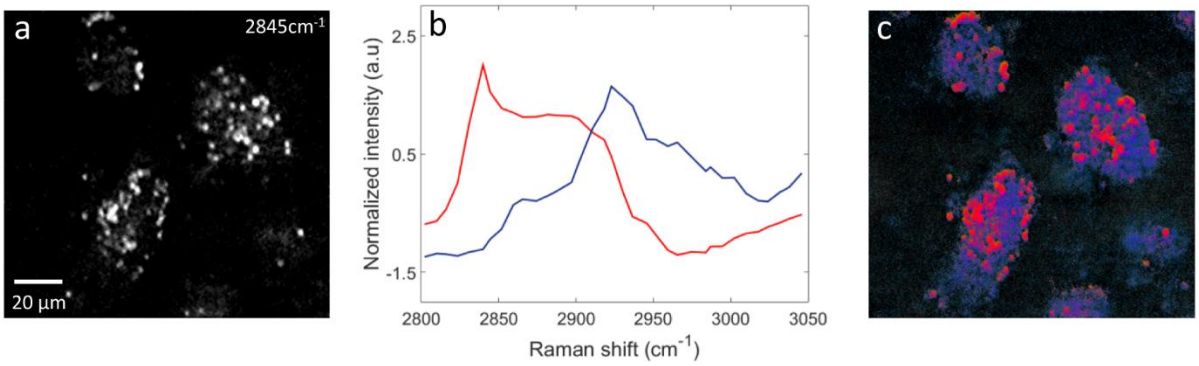

Fig 4.4 Hyperspectral stimulated Raman scattering (SRS) scan covering the CH stretching Raman band (2800 - 3050 cm^{-1}) confirms association to lipid droplets. (a) SRS image at 2845cm^{-1} (CH_2 symmetric stretching) characteristic of lipids. (b) Result of 3 endmember vertex component analysis (VCA). The red and blue show the normalized spectra of the 2 major endmembers retrieved. (c) Pseudo-colored VCA image of the SRS hyperspectral scan. The red spectrum is characteristic of lipids. It co-localizes with the lipid droplets observed in (a). The blue spectra have the features of the protein matrix that fills the cellular cytoplasm.

normoxia and 48 hours hypoxia. For further quantitative analysis, the phasor distribution was divided into 'LLS' window: red square, center (0.151, 0.243), size = 0.14 and 'total NADH' window: gray dotted rectangle, center (0.468, 0.33), size ($\Delta g = 0.28$, $\Delta s = 0.14$). The position of the 'LLS' window was determined by the center of mass of the LLS phasor distribution. The 'total NADH' window corresponds to the position of pink and cyan windows in Fig 4.2(b). Fig. 4.3(b) shows the normalized percentage of pixels in each phasor window for 24 and 48 hours hypoxia and the 24 and 48 hours normoxia controls. An ANOVA with post-hoc

Bonferroni correction indicates a significant increase in LLS for cells exposed to 48 hours hypoxia, in comparison to normoxia controls as well as 24 hours hypoxia [Fig. 4.3(b)].

Though the granular areas had the characteristic long lifetime fingerprint on the phasor plot, we confirmed the association with lipids by performing hyperspectral SRS imaging that covers the CH stretching Raman band (2800 - 3050 cm-1) on the hiPS-CM clusters exposed to 48 hour hypoxia. In the SRS hyperspectral images, the strongest signal was observed at

2845 cm^{-1} (CH2 symmetric stretching Raman mode, characteristic of aliphatic components). Fig. 4.4(a) is the SRS scan at 2845 cm^{-1} showing intense signal from lipid droplet-like granular structures. Hyperspectral SRS spectra were analyzed using vertex component analysis (VCA) with 3 end members as has been previously described[153]. Fig. 4.4(b) shows the two major spectra retrieved from the VCA analysis (shown in red and blue). The third end member spectrum corresponds to background and has not been shown here. Each spectrum shown in Fig. 4.4(b) has been normalized to its maximum. Fig. 4.4(c) is the pseudo-colored VCA image where the colors describe the chemical content of each pixel. The red areas in Fig. 4.4(c) associate with the spectrum in red in Fig. 4.4(b), which is characteristic of lipids[153]. These areas match very well with the granular areas observed Fig. 4.4(a), thus consistent with lipid droplets. The blue areas in Fig. 4.4(c) exhibited spectra typical of cellular protein, represented by the blue curve in Fig. 4.4(b).

4.3.4 Cardiotoxic drugs produce LLS

To further substantiate the sensitivity of the FLIM-phasor technique to detect oxidative stress in the cardiomyocyte, we treated hiPS-CMs with two known cardiotoxic drugs, AZT and cisplatin. FLIM was performed along with simultaneous ROS imaging using the ROS sensitive fluorescent dye, CellROX. Fig. 4.5(a) shows the LLS FLIM map (in red) created by the LLS window (red square, center (0.217, 0.236), side = 0.28) on the phasor plot (middle panel). Again, the position of the LLS window was determined by the center of mass of the LLS phasor distribution. Larger numbers of lipid droplets with LLS signal were observed in the FLIM maps of the treated cells [Fig. 4.5(a)]. For quantitative analysis, the normalized percentage of pixels in each image with phasor in the LLS window was calculated [Fig. 4.5(a)]

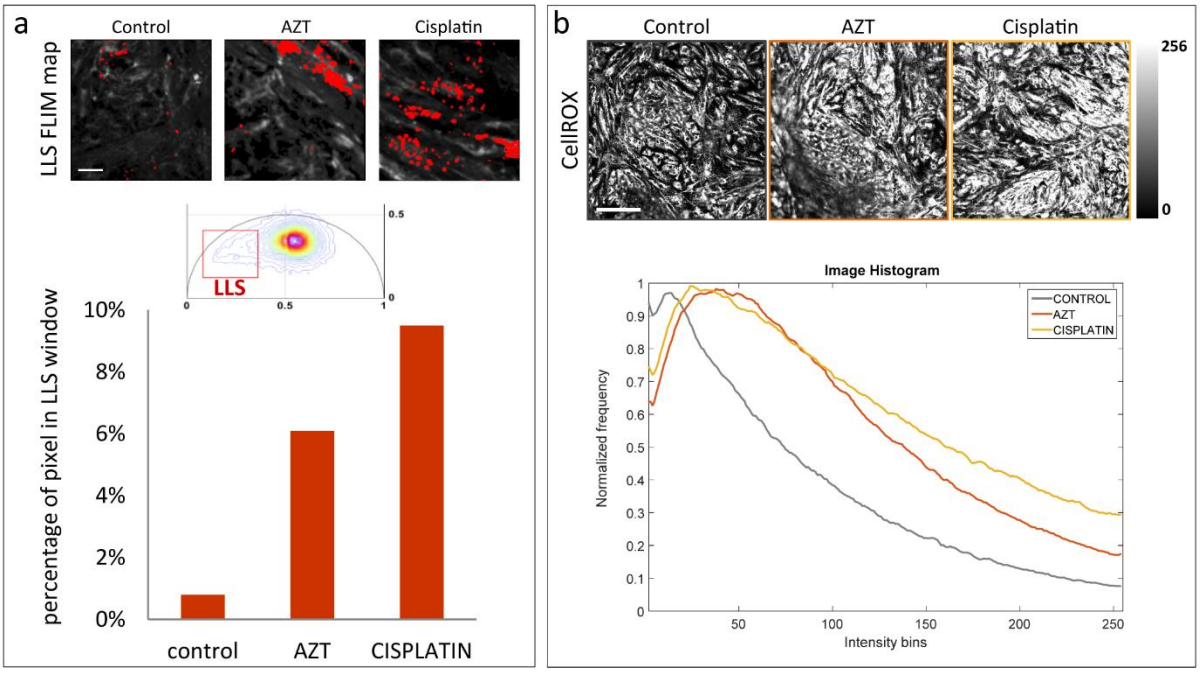

Fig 4.5 LLS produced by cardiotoxic drugs 3′-Azido-3′-deoxythymidine (AZT) and cis-Diamineplatinum(II) dichloride (cisplatin). (a) Top panel shows LLF FLIM map (in red) of hiPS-CM clusters (control, AZT treated and Cisplatin treated). The FLIM map is generated by the LLS window (red square) selecting the characteristic longlifetime on as shown on phasor plot (middle panel). Bottom panel shows the percentage pixels for control, AZT treated and cisplatin treated cells with lifetime phasors within the LLS phasor window. The scale bars are 20μm. (b) Top panel shows confocal image (control, AZT treated and cisplatin treated cells) of ROS indicator CellROX , excited at 633nm and signal collected within 640-740 nm. The scale bars are 200μm. Bottom panel shows the corresponding image intensity histogram.

bottom panel. Fig. 4.5 (b) shows confocal ROS images of control, AZT treated and cisplatin treated cells. Corresponding intensity histograms of the confocal images show more intense CellROX signal in the cells treated with AZT and cisplatin compared to the controls which did not receive any treatment.

4.4 Discussion

In this work, we demonstrate how FLIM imaging can be used to characterize the metabolic state and oxidative stress in hiPS-CMs using phasor analysis of endogenous biomarkers. Our results demonstrate the potential of this technique to detect drug-induced stress and

pathological conditions in hiPS-CMs. We performed NADH FLIM of hiPS-CM treated with KCN, a known poison of mitochondria. Comparing the NADH FLIM phasor of the same cells before and after the treatment, we observe a large shift towards the free NADH fingerprint on the phasor plot, indicating a rise in the free/bound NADH ratio. This correlates with the decrease in oxidative phosphorylation which occurs in the mitochondria. The result shows the capability of the FLIM-phasor technique to detect metabolic changes in hiPS-CMs.

Lack of sufficient oxygen supply to cardiac tissue leads to pathophysiological conditions which might cause cardiac damage[158]. In the electron transport chain, oxygen is the terminal electron acceptor and its deprivation inhibits oxidative phosphorylation. Hence, hypoxia induces alteration of metabolic functions. Cells tend to depend on anaerobic glycolysis for production of ATP. This metabolic switch can be observed in our results. NADH FLIM-phasor analysis of hiPS-CMs subjected to 24 hours hypoxia (1% oxygen) had higher free/bound NADH ratio indicative of glycolysis as compared to the control cells in normoxia. The direction of this shift follows the same trend as observed in response to KCN treatment, although the shift is greater in the latter condition due to the cyanide poisoning by high concentration of KCN. Such increase in free fraction of NADH compared to its bound form upon hypoxia was reported in NADH fluorescence anisotropy studies in brain slices[159].

Another significant observation of FLIM-phasor analysis of hypoxic hiPS-CMs was the presence of LLS in the form of lipid droplets, which we had previously identified as a biomarker of oxidative stress[9]. This indicates the presence of lipid oxidation by ROS in hypoxic conditions. Interestingly, the amount of LLS increased significantly with 48 hours of hypoxia exposure when compared to 24 and 48 hours normoxia and 24 hours hypoxia.

Furthermore, oxidative stress could be injurious to cells ultimately leading to cell death by apoptosis or necrosis [160]. Hence in the 48 hours hypoxia condition, there could be certain degree of cell death causing a loss in metabolism. SRS imaging corroborates the presence of lipid droplets in the cells exposed to 48 hours hypoxia. According to a study by Duranteau et. al. [147] on cardiomyocytes exposed to hypoxia, ROS is generated by the mitochondria which plays the role of oxygen sensor. They hypothesized that in cardiomyocytes, with decrease in oxygen concentration, this ROS signaling elicits adaptive responses like reduced contractile activity and suppressed oxygen consumption. They used an exogenous ROS sensitive dye to show an increase in ROS with a decrease in oxygen concentration which correlates with our observation. Several studies have also attributed generation of ROS during hypoxia or brief periods of ischemia as trigger for cardioprotective preconditioning[148,161]. The stress response initiated by ROS would lead to better adaptation to subsequent prolonged episodes of ischemia and increased chance of survival.

Oxidative stress by ROS was further detected by LLS generation in hiPS-CM treated with known cardiotoxic drugs. LLS were observed in FLIM-phasor analysis of hiPS-CM treated with antiviral drug AZT. Anti-cancer drug cisplatin is often used in ovarian, testicular, gastrointestinal cancer [152] . However, it has been shown to produce oxidative stress and cardiotoxicity. Our results show an increase in LLS in hiPS-CM with cisplatin treatment. In the imaged areas, quantitative analysis shows a 5-fold and 8-fold increase of LLS signal in AZT treated and cisplatin treated cells respectively. Simultaneous confocal ROS imaging employing CellROX dye confirmed the increase in ROS in the treated cells.

In conclusion, our results demonstrate that FLIM-phasor is a robust technique for assessing and indexing features of cardiac metabolism and ROS-induced oxidative stress. This method could prove beneficial for drug development and screening studies, especially for *in vitro* cardiac models derived from stem cell-derived cardiomyocytes. Furthermore, these indices play a major role in the pathogenesis of a myriad of cardiovascular diseases including atherosclerosis, ischemic heart disease, and heart failure. Use of endogenous fluorophores as intrinsic biomarkers of metabolism and oxidative stress makes this technique label-free, creating the possibility of *in vivo* measurements. Additionally, cardiac systems can be monitored over time. Thus, this non-destructive technique will find potential application in *in vitro* cardiac models in drug discovery and safety screening, especially unanticipated cardiotoxic effects of anti-cancer drugs as well as understanding the pathogenesis of cardiac diseases and therapy.

4.5 Chapter Summary

This chapter demonstrates label-free optical imaging technique to assess simultaneous metabolic status and oxidative stress in human induced pluripotent stem cell-derived cardiomyocytes by two-photon fluorescence lifetime imaging of endogenous fluorophores. Our results show the sensitivity of this method to detect shifts in metabolism and oxidative stress in the cardiomyocytes upon pathological stimuli of hypoxia. We quantified the changes in metabolism and increase in oxidative stress with increased duration of hypoxia. We could also quantify oxidative stress response to known cardiotoxic drugs. This non-invasive imaging technique could prove beneficial for drug development and screening, especially for *in vitro* cardiac models created from stem cell-derived cardiomyocytes and to study the pathogenesis of cardiac diseases and therapy. Further, this technique could be extended to other hiPS derived cells or tissue engineered micro organs.

Chapter 5

Metabolic imaging of tissue engineered microphysiological systems

Chapter overview: In the previous chapters we applied fluorescence lifetime imaging to cell lines as well as mice tissue. In this chapter we perform label-free metabolic imaging of tissue engineered 'tumor-on-a chip' in a microfluidic device based platform.

Parts of this chapter has been published in the following paper:

Sobrino A., Phan D., Datta R et al. 3D microtumors in vitro supported by perfused vascular networks. Scientific Reports (2016) 23; 6 : 31589

5.1 Introduction

Microphysiological systems consisting of three-dimensional (3D) tissue engineered organ constructs employing human cells or interacting organoids on a chip unfolds new possibilities for research in the fields of toxicology, medicine, physiology, basic biology and significantly in pharmacology. Two-dimensional (2D) cell cultures using immortalized or primary cell lines nor animal models are completely capable of reproducing the interactions between drugs and organs or between drugs themselves in organ microenvironments[162]. This motivates development of such 3D miscophysiological systems. A large number of drugs showing encouraging results in the preclinical steps of drug trials fail at the clinical study stage making pre-trial assessments unreliable as predictors of drug efficacy and toxicity in humans[137]. The development of such unique 3D microfluidic-device based microphysiological tissue system, which mimics human organs structurally and functionally,

is gaining importance especially in the areas drug development, drug screening, and cancer therapy. For developing such microtissue systems, there is a need for non-destructive techniques for understanding and evaluating these 3D tissue models. In this work we present a non-invasive, label-free imaging technique to study metabolism of a vascularized human "organ-on-a-chip"[163].

The microfluidic device platform is created by standard photolithography from optically clear polydimethyl siloxane (PDMS) as has been described previously[164]. It consists of two outer microfluidic channels that act as arteriole (high pressure) and venule (low pressure), connected by three diamond shaped tissue chambers, into which is injected a slurry of extra cellular matrix (ECM) and cells: fibroblast (normal human lung fibroblast) and human endothelial colony forming cell-derived endothelial cells (ECFC-ECs). Vessel-like fragments appear within 2 to 3 days and over the course of 5 to 7 days endothelial cells (EC) self-assemble into an interconnected network that anastomoses with the outer channels. EC migrate into the outer channels, forming a tight seal, and over time, line the surface of the channel. Flow is generated by a hydrostatic head. Stromal cells are required for proper formation of the vascular networks, and a subset of these consistently envelop the newly-formed vessels, forming tight appositions. This vascularized micro-organ forms the base tissue. The tumor-on-a-chip version of the model consists of tumor cells like breast cancer tumor lines MCF7 and MDA-MB231 and human colorectal cancer (CRC) cell line HCT116, supporting fibroblast and vascular network developed from ECFC-ECs in the tissue chamber. Growth of the microphysiological system can be monitored by incorporating cells expressing fluorescent protein. Time lapse imaging or confocal imaging is employed to evaluate features like vessel length, diameter, and branching, tumor development and volume. Perfusion of

vessels is monitored by flowing FITC-dextran. Immunofluorescent staining can be employed to identify antibodies specific to EC like cluster of differentiation 31 (CD31) or perivascular cells surface proteins like neural/glial antigen 2 (NG2) or beta-type platelet-derived growth factor receptor (PDGFR-β). However, this required fixing the device.

To evaluate the metabolic status of the microtissue system, we employed two photon fluorescence imaging microscopy (FLIM) of reduced nicotinamide adenine dinucleotide (NADH). Cellular metabolism is a potentially powerful biomarker for cellular state and response to drugs. FLIM has been employed to microfluidic devices to monitor temperature, analyze flow kinetics, map molecular diffusion of iodide ions across a microchannel, imaging mixing profile and solvent viscosity and to image DNA–dye interactions within a continuous-flow microfluidic device [165–172]. Fluorescence intensity and lifetime of NADH to evaluate metabolism of engineered tissue has been explored previously. For example, NADH autofluorescence in pancreatic islets loaded in a microfluidic device has been employed to study pyruvate dehydrogenase (PDH) and pyruvate carboxylase (PC) metabolism[173,174].

In this work we used the phasor approach to NADH- FLIM. The details of this technique is described in chapter 2. NADH FLIM allowed non-invasive monitoring of metabolism of the complex tissue engineered 3D organ system at single cell level. Metabolic differences between various cell types which constitute the tumor-on-a-chip could be observed. The non-invasive technique allowed longitudinal survey of metabolic status of the devices over days. Furthermore, response to anticancer and anti-angiogenic drugs could be easily quantifies at cellular level.

5.2 Materials and methods

5.2.1 Cell culture and device seeding

For loading the microfluidic device, fibrinogen solution was prepared by dissolving 70% clottable bovine fibrinogen (Sigma-Aldrich) in 1× Dulbecco's Phosphate Buffered Saline with Ca^{2+}/Mg^{2+} (LifeTechnologies) to a final concentration of 10 mg/mL. Normal human lung fibroblasts (NHLFs) were purchased from Lonza and cultured in DMEM (Corning) containing 10% Fetal Bovine Serum (FBS, Gemini Bio Products), while human endothelial colony forming cell-derived ECs (ECFC-ECs) were isolated from cord blood and expanded on gelatin-coated flasks in EGM-2 (Lonza) with approval from UC Irvine's Institutional Review Board. These cells were harvested and resuspended in fibrinogen solution at a concentration of $5x10^6$ cells/mL respectively. To create a tumor microtissue, cancer cells (colorectal cancer cell lines, HCT116, and breast cancer cell lines MDA-MD-231, and MCF-7 obtained from UC Irvine's Chao Family Comprehensive Cancer Center) were then harvested and resuspended in the mixture at a concentration of 200,000 cells/mL. The final cell-matrix suspension was mixed with thrombin (50 U/mL, Sigma-Aldrich) for a final concentration of 3 U/mL, quickly seeded into the microtissue chambers, and allowed to polymerize in a 37°C incubator for 15 minutes. Laminin (1 mg/mL, LifeTechnologies) was then loaded into the microfluidic channels through medium inlets and incubated at 37°C for an additional 15 minutes to stimulate ECFC-EC anastomosis with the microfluidic channels. After incubation, culture medium (EGM-2, Lonza) was introduced into the microfluidic channels and subsequently medium reservoirs to establish a 5-mm H_2O interstitial pressure across the tissue chambers. Medium in reservoirs was changed and leveled every other day to maintain interstitial flow.

The cells were transduced with lentivirus to express fluorescent proteins mCherry or GFP for identification.

5.2.2 Drug exposure

To assess drug screening experiments, cells in the microfluidic device were exposed to reported *in vivo* plasma concentrations of different FDA approved anti-cancer drugs or a standard dose of 100 nM. 5-Fluoruracil (5-FU), and Sorafenib were obtained from the NIH-MPS Training Compound Collection at Evotec. All compounds were dissolved in dimethyl sulfoxide (DMSO) and added in the medium with less than 0.01% DMSO. For drug exposure, after 5-8 days of cells cultured in the microdevice, media from the device is replaced by media containing the drug at the desired concentration, and delivered through the microfluidic channels using the hydrostatic pressure gradient.

5.2.3 Immunofluorescent staining and imaging for Collagen IV

For immunofluorescent staining, devices were fixed by flowing 4% paraformaldehyde (Sigma-Aldrich) for 2h at room temperature, followed by an overnight PBS wash at 4^{o}C. Blocking, washing, antibody incubation, and nuclei staining steps are also conducted by flowing reagents through the microfluidic channels overnight at 4^{o}C. Collagen IV was observed by staining using rabbit anti-human Collagen IV polyclonal antibody (AbD-Serotec 2150-0150, Bio-Rad) followed by Alexa 408 Donkey anti-rabbit secondary antibody. Confocal imaging of stained collagen IV was performed on Zeiss LSM 710 microscope (Carl Zeiss, Jena, Germany) using a 20x air objective, 0.5 N.A. (EC Plan-Neofluar, Carl Zeiss,

Oberkochen, Germany), excited with 405 nm and emission signal was collected between 410–585 nm.

5.2.4 Fluorescence lifetime image acquisition and analysis

Fluorescence lifetime imaging microscopy (FLIM) of reduced nicotinamide adenosine dinucleotide (NADH) was performed on a Zeiss LSM 710 microscope (Carl Zeiss, Jena, Germany) using a 20x air objective, 0.5 N.A. (EC Plan-Neofluar, Carl Zeiss, Oberkochen, Germany) with two photon excitation of 740 nm (titanium:sapphire MaiTai laser from Spectra-Physics, Mountain View, CA). Image scan speed was 25.21 µs/pixel and image size is 256 × 256 pixels. For NADH FLIM of the whole chambers, a 2 by 2 tile scan was performed. 460/80 nm bandpass filter was employed as emission filter for 'channel 1' (for NADH) and 525/25 nm for 'channel 2' and two photomultiplier tubes (H7422P-40, Hamamatsu, Japan) were used for detection of the two channels. FLIM data was acquired using A320 FastFLIM FLIMbox (ISS, Champaign, IL). For acquisition and FLIM data analysis SimFCS software, developed at the Laboratory for Fluorescence Dynamics (LFD, UC Irvine), was used.

5.2.5 Confocal imaging

Confocal imaging of fluorescence reporters was carried out simultaneously with lifetime imaging in the same microscope system. eGFP was excited with 488 nm and signal collected between 493–581 nm. mCherry was excited with 561nm and emission collected between 578–696 nm. mRFP was excited with 561 and emission collected between 582–754 nm. Azurite Blue was excited at 405nm and emission collected between 410–585 nm. Image acquisition and post processing was done using Zen software (Zeiss, Germany). To reduce

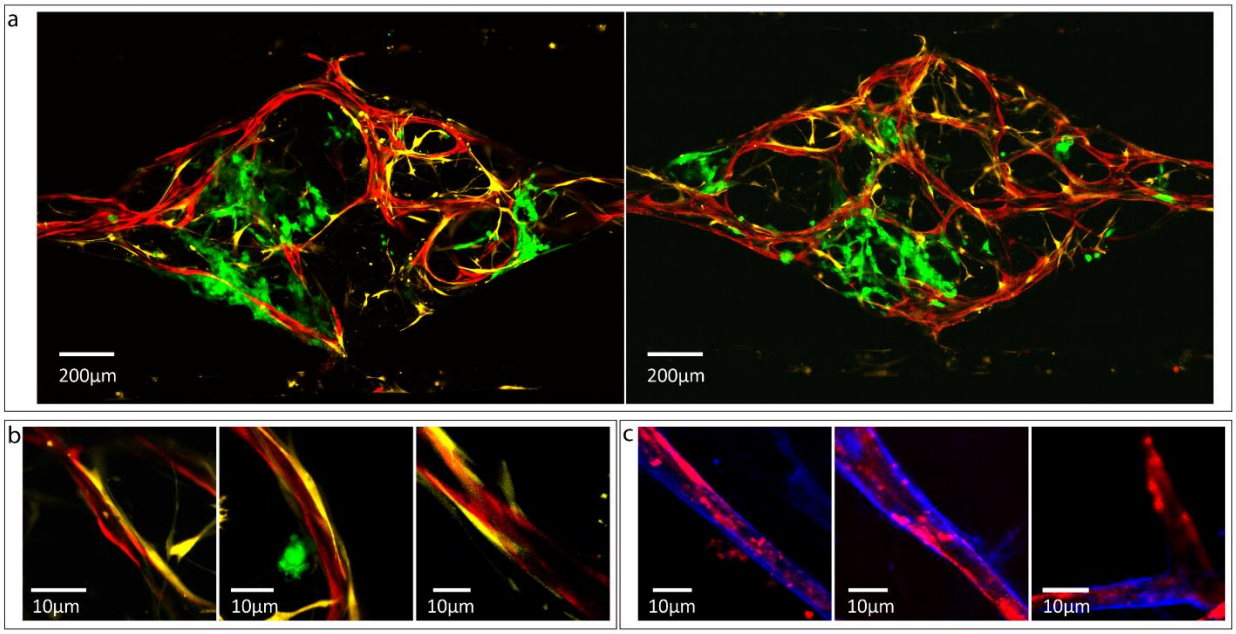

Fig 5.1 Multicolor confocal images reveal interaction between tumor, microvessels and stromal cells. (a) Lentivirally-transduced HCT116 (green), stromal/perivascular cells (yellow) and EC (red) in two tissue chambers visualized by confocal microscopy. (b) Closer look at microvessels reveal fibroblasts (yellow) wrapped around the vessels (red). (c) Collagen IV staining (blue) identifies basement membrane deposition.

confusion, some images have been re-colored to maintain consistent color-coding throughout the chapter. Thus vessels are shown as red and tumor cells as green, although in some cases EC were expressing GFP and the tumor cells were expressing mCherry (or mRFP). We have seen no differences in cell behavior when they express GFP vs mCherry or mRFP.

5.3 Results

5.3.1 Confocal fluorescence imaging to distinguish the different cell types forming the micro-tissue system

We performed confocal fluorescence imaging of tissue chamber seeded with cells that have lentivirally-transduced fluorescent proteins. Multicolor confocal images show interactions

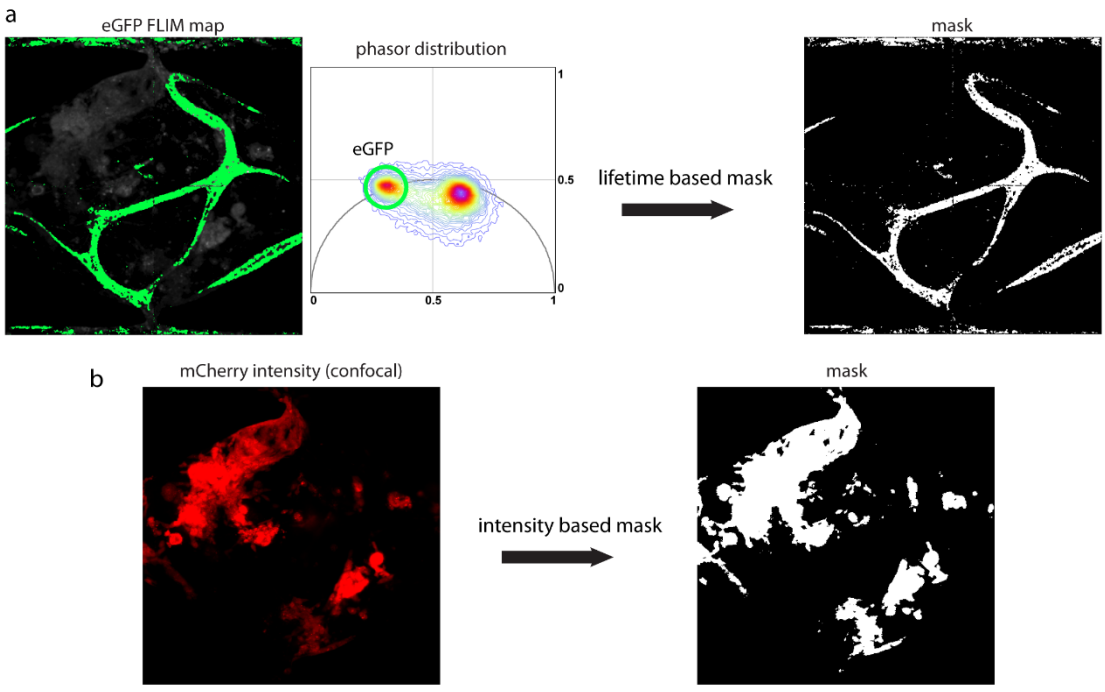

Fig 5.2 Masking to delineate regions of interest. (a) Lifetime based masking where phasor fingerprint of eGFP is used to select cells transfected with eGFP. (b) Intensity based masking where confocal image of mCherry excited at 561nm and emission collected between 578–696 nm, is used to create the mask

between microvessels, stromal cells and tumor. The fluorescent markers helped identify the different cell types in the tissue chamber. Fig 5.1 (a) shows multicolor confocal image of two vascularized diamond shaped tissue chamber with developed vessel network in red, tumor (HCT116) clusters in green and stromal/perivascular cells in yellow. Confocal imaging revealed areas where stromal cells wrapped around the developed vessels mimicking closely the normal physiology [Fig 5.1(b)]. Fig 5.1(c) shows Collagen IV staining (blue) by immunofluorescence labeling, displaying collagen IV-rich basement membrane.

eGFP and mCherry transfection guided us to differentiate the region of interest (tumor, vessel, stroml cells) and analyze and compare their individual phasor distributions. In this work we applied two kinds of masking. For eGFP, we used lifetime phasor distribution of

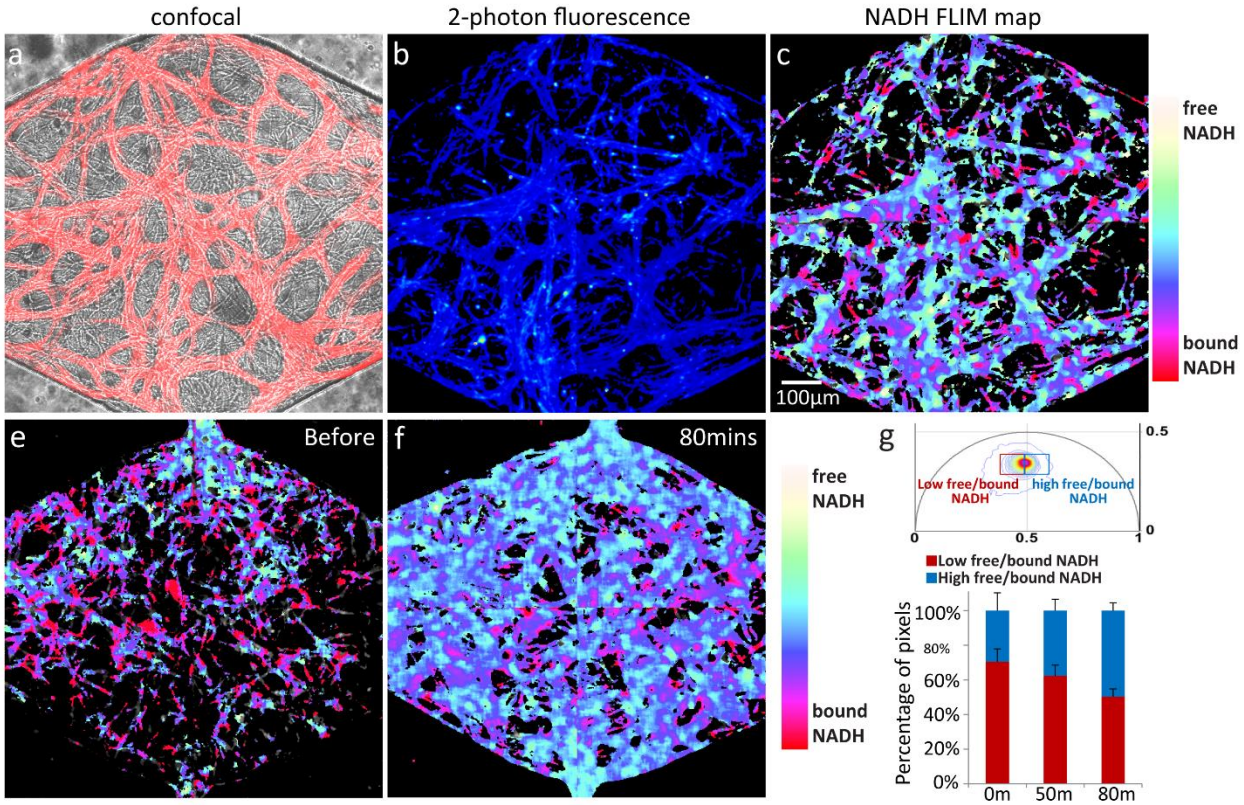

Fig 5.3 FLIM map of whole tissue chamber. (a) Lentivirally-transduced EC (red) overlaid onto the brightfield image. (b) Corresponding two-photon fluorescence intensity. (c) NADH FLIM map. (d –e) Chemical disruption of metabolism. NADH FLIM map of the tissue chamber before (e) and after 80min (e) of KCN exposure. (f) Quantification of the response ofcells to KCN showing poisoning of mitochondrial function by KCN.

'channel 2' (see section 5.5.4) to select areas of eGFP [Fig 5.2(a)]. mCherry mask was created by using the confocal image excited at 561nm and emission collected between 578–696 nm [Fig 5.2(b)]. These masks were then applied the NADH channel to obtain the corresponding phasor distribution of the individual areas of tumor, vessel and tumor microenvironment.

5.3.2 Metabolic response to respiratory inhibitor

To assess the possibility of metabolic imaging of the tissue chamber, we first used FLIM to examine the metabolic profile of the vasculature in tissue chamber. Fig 5.3(a) shows the confocal image with vessels (in red) overlaid on the brightfield image of the tissue chamber.

Fig 5.3(b) shows the two-photon fluorescence intensity image and Fig 5.3(c) shows the corresponding NADH FLIM map of the whole tissue chamber. The linear decrease in the free/bound NADH ratio is colored using color scale white-cyan-blue-pink-red as shown. Next we measured the response of the tissue chamber to potassium cyanide (KCN), a known blocker of the respiratory mitochondrial transport chain. FLIM data were acquired before treatment, as well as 50 mins and 80 mins after treatment. Fig 5.3 (d) shows FLIM map before treatment and Fig 5.3 (e) is one 80 mins after treatment. KCN induced a shift towards higher free to bound NADH ratio, in line with inhibition of oxidative phosphorylation[146]. For quantification, we divided the phasor distribution at the center of mass into two windows [Fig 5.3 (f)] representing high free to bound NADH ratio (blue square) and low free to bound NADH ratio (red square) and plotted the fraction of pixels in each image that belonged to the two groups. The result shows an increase in the pixels within the blue window indicating a shift towards higher free NADH. This result confirms the sensitivity of NADH FLIM of the microtissue system to metabolic changes.

5.3.3 NADH FLIM reveals metabolic differences between ECs and surrounding fibroblasts

A closer look at NADH FLIM map of ECs and fibroblast revealed metabolic differences. Fig 5.4(a) shows confocal image of two representative areas where the red areas are ECs. Fig 5.4(b) shows the corresponding FLIM map of areas within the tissue chamber with vessel and surrounding fibroblast. Once again the same color scale of white-cyan-blue-pink-red was applied on the phasor distribution as shown in Fig 5.4 (c) to represent the linear decrease in the free/bound NADH ratio. Interestingly we found a comparatively higher free/bound NADH ratio in the ECs shown in white/cyan colors [Fig 5.4 (b)]. For further quantification,

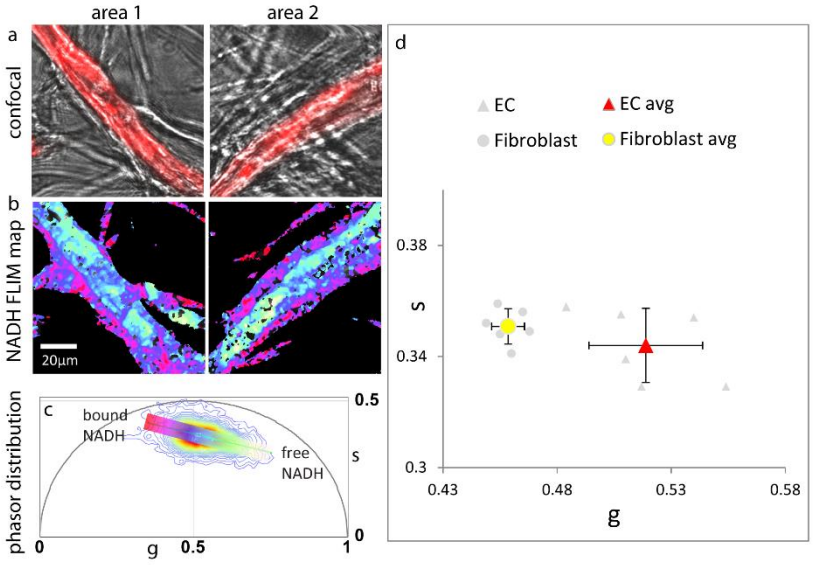

Fig 5.4 NADH FLIM map reveals metabolic differences between ECs and fibroblasts wrapping them. (a) Confocal images of the representative images of two areas. (b) NADH FLIM map distribution using color scale of white-cyan-blue-pink-red. (c) FLIM phasor distribution. (d) Scatter plot distribution of average g and s values of ECs (grey triangle) and fibroblasts (grey solid circles) and the corresponding average phasors for the ECs (red triangle) and the perivascular cells (yellow circle). Error bars show mean ± s.d of 6 replicates (n= 3, $p< 0.05$).

the average g and s coordinates of EC and fibroblast were calculated by using the masking technique described in section 5.5.1 and plotted as a scatter plot shown in Fig 5.4 (d). This plots further supports the right shift of EC phasors. This result suggests that EC are more glycolytic than stromal cells, which is consistent with published reports[175,176]

5.3.4 Metabolic mapping of tumor-on-a-chip

Cellular metabolism is a potentially powerful tumor biomarker. Cancer cells often rely on glycolysis, uncoupled from oxidative phosphorylation and independent of local O_2 concentrations, for energy production known as aerobic glycolysis or the Warburg effect[3]. We next asked whether the FLIM-phasor approach could be used in vascularized micro tumors to interrogate tumor cell metabolism and the response of cells to chemotherapeutic

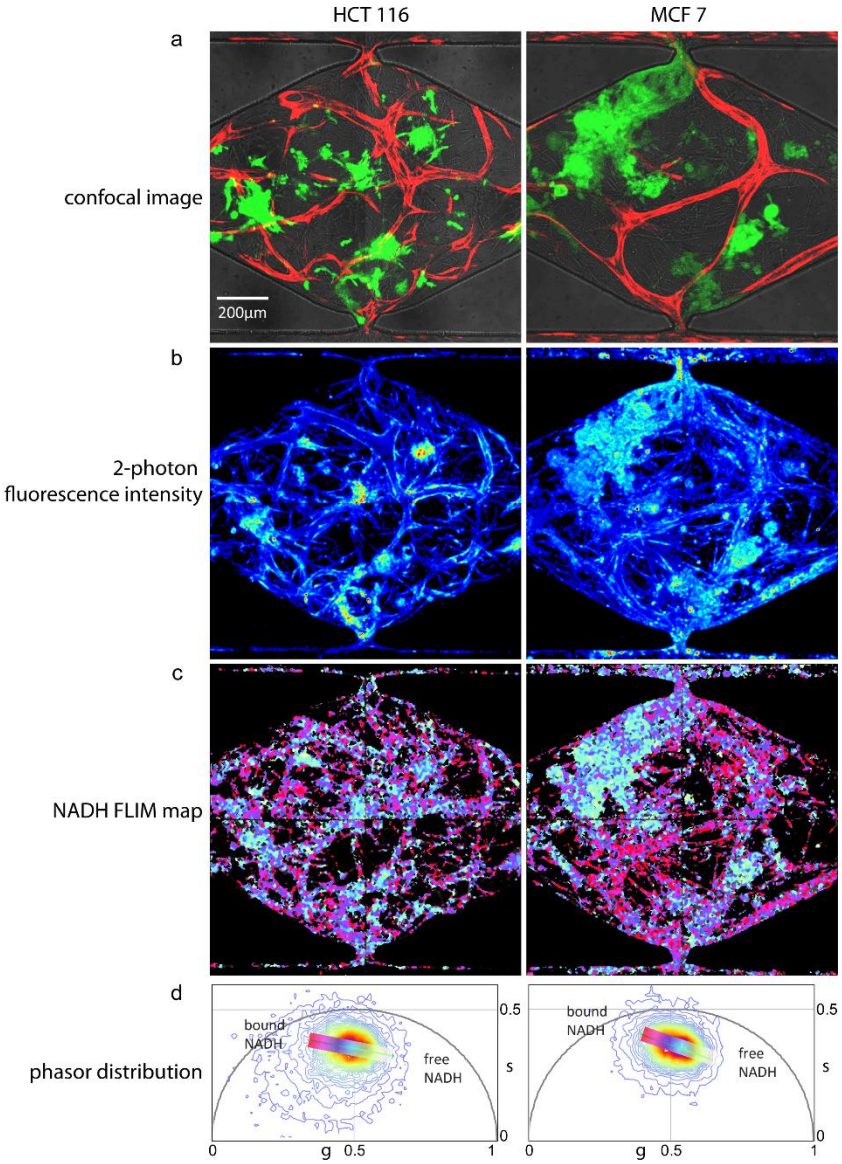

Fig 5.5 Fluorescence Lifetime Imaging Microscopy (FLIM) of 'tumor-on-a-chip'. (a) Confocal images of two tissue chambers loaded with cancer cell line HCT 116 (left) and MCF7 (right) in green and microvessel in red. (b) Corresponding two-photon fluorescence intensity images. (c) NADH FLIM map with the linear decrease in the free/bound NADH ratio is colored using color scale white-cyan-blue-pink-red as shown in the corresponding phasor (d).

challenge. As shown in Fig. 5.5 we found higher NADH free/bound ratios in cancer cells (white/cyan) relative to other cells in the surrounding microenvironment (pink/red), including vascular and stromal cells. This suggests that the tumor cells are more glycolytic

than the surrounding cells, which is consistent with their known preference for aerobic glycolysis.

5.3.5 Metabolic differences between tumor and its microenvironment

To further investigate the metabolic difference between tumor and its microenvironment, we performed NADH FLIM on tissue chambers seeded with four different tumor cells lines - MCF-7, MDA-MB-231, HCT116 and SW620. Masking was applied to separate out regions of tumor from its microenvironment as described in section 5.5.1. Fig 5.6 shows the four scatter plot corresponding the to the four tumor cell lines. Tumor cluster developed from MCF7, MDA-MB-231 and HCT116 displayed higher free/bound NADH ratio compared to its microenvironment. We found this difference to be statistically significant. Interestingly for SW620, although there was a minute overall right shift in the tumor phasor, this difference was not significant.

5.3.6 Response to drugs and media flow cessation

Using this technique, we studied the effect of anti-cancer drug 5-Fluoruracil (5-FU). Confocal images show a much reduced size of tumor in the device where the drug was administered as shown in Fig 5.7 (a-b). Interestingly, we observed a strong metabolic shift in MCF 7 cells after exposure of the tumor microenvironment to 100uM 5-FU for 96 hours [Fig 5.7 (c)] consistent with a slowed glycolytic rate. It should be noted that 5-FU induces apoptosis , which also leads to high levels of bound NADH (red)[177]. Importantly, the metabolic profile of the stroma remained unchanged in response to 5-FU [Fig. 5.7(d)].

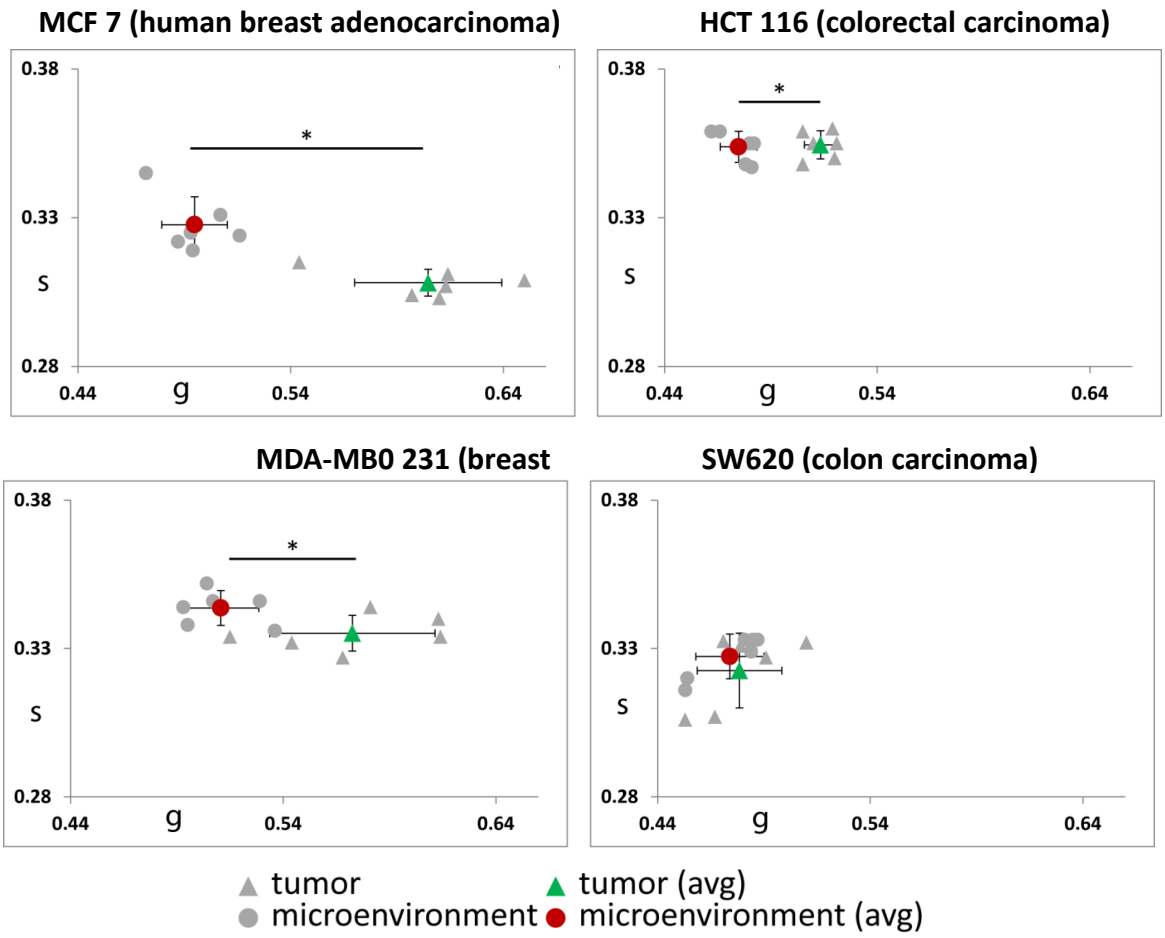

Fig 5.6 Heterogeneity of FLIM signatures between different tumors and their microenvironments. Phasor scatter plots comparing MCF-7, MDA-MB-231, HCT116 and SW620 to their surrounding stroma. Error bars show mean ± s.d ($p < 0.05$).

Active angiogenesis is one of the hallmarks of cancer[178]. During progression of tumor, the otherwise quiescent vasculature continues sprouting new vessel branches. This neovasculature serves to provide nutrient and oxygen to the newly developing tumor and help in metabolic waste removal. The formation of new blood vessels in and around the tumor can be driven by a number of tumor-derived factors, a key family being the VEGFs. Targeting these growth factors and their receptors has proven moderately successful in the treatment of several human cancers, including cervical, glioblastoma, and metastatic CRC,

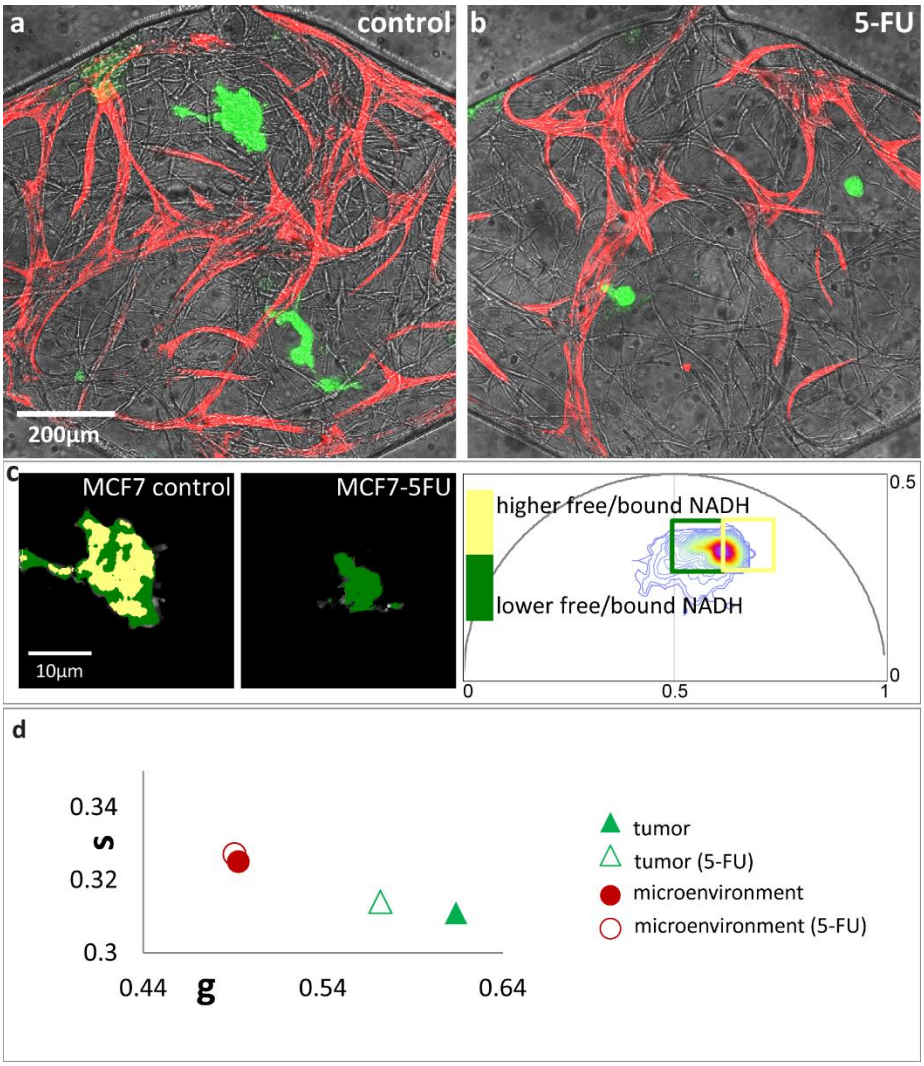

Fig 5.7 NADH FLIM map of MCF7 shows response to anticancer drug. Multicolor confocal images of Control tissue chamber (a) and tissue chamber administered with 100µM 5-Fluoruracil (5-FU) for 96 hours. The tumor clusters in (b) are smaller than the control. (c) right panel shows NADH phasor distribution of tumor clusters areas from each condition divided by two cursors, green and yellow representing lower and higher free/bound NADH ratio respectively. (c) left panel shows the corresponding phasor map. Control tumor has more yellow pixels compared to the treated one with all green pixels. (d) Scatter plot showing the NADH phasors for the treated and non-treated conditions for the tumor and its microenvironment.

especially in combination with more established anti-cancer agents. We therefore examined the effect of sorafenib, a multikinase inhibitor is widely-used as antiangiogenic agent. Fig 5.8 (a-b) shows the confocal images with vessels in red and corresponding NADH FLIM map of devices treated with 10 µM sorafenib for 96 hours. FLIM map shows a strong difference

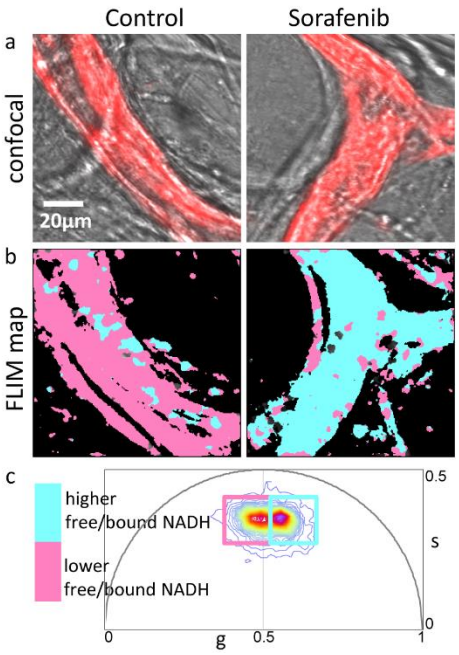

Fig 5.8 Response of EC to anti-angiogenic drug. (a) Confocal image showing EC in red of control and sorafenib treated tissue chambers. (b) corresponding FLIM map. (c) The phasor distribution with pink square selecting lower and cyan square choosing the higher free/bound NADH ratios.

between the two groups with a shift towards lower free to bound NADH ratio after drug treatment [(Fig 5.8(b)]. Masking was applied to separate out only the ECs present in the images and the corresponding average g and s values are plotted for both the groups in Fig 5.8(c).

We also examined the metabolic profile in the presence and absence of flow, which limits nutrient delivery but not oxygen delivery (which diffuses freely through the PDMS). Fig 5.9 (a) shows multicolor confocal images of tissue chamber with flow, and same chamber two days without flow and six days without flow. Fig 5.9(b) shows the corresponding NADH FLIM map. Under no-flow conditions the micro-tissue showed an increase in free NADH, in especially in the tumor suggestive of a shift away towards a higher glycolytic rate perhaps in absence to nutrients. Taken together, these data suggest a hierarchy of free/bound NADH

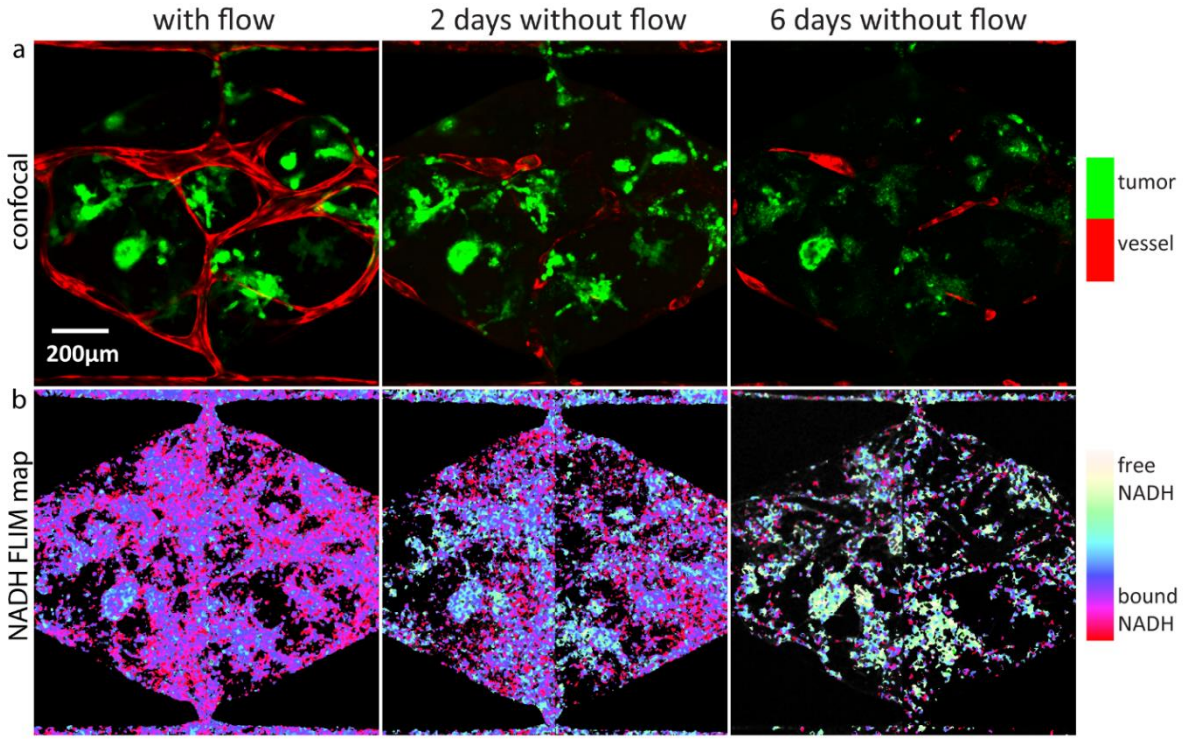

Fig 5.9 Response to flow cessation. (a) Multicolor confocal of tissue chamber with flow and after 2 and 6 days after stopping flow. (b) Corresponding NADH FLIM maps of the tissue chamber.

(and potentially aerobic glycolytic rate) in the cells of the tumor microenvironment, from tumor (highest glycolytic rate/ lowest oxidative phosphorylation profile) to EC (moderate glycolytic rate) to stroma (lowest glycolytic rate / highest oxidative phosphorylation profile), and furthermore suggest that inhibiting glycolysis may be an effective strategy to target tumor cells as well as their associated vasculature.

5.4 Discussion

Development of microfluidic-device based microphysiological tissue system, which mimics human organs structurally and functionally, is gaining importance especially in the areas drug development, drug screening, and other healthcare research. Hence, there is a need for non-destructive techniques for understanding and evaluating such three-dimensional (3D)

tissue models. In this work we present a non-invasive, label-free imaging technique to study metabolism of a vascularized human “tumor-on-a-chip”. The model consists of tumor cells (tumor lines like breast cancer tumor lines MCF7 and MDA-MB231 and human colorectal cancer (CRC) cell line HCT116 and colon cancer cell line SW620), supporting fibroblast and vascular network developed from endothelial cells in the diamond shaped tissue chamber of an optically clear polydimethyl siloxane (PDMS) based microfluidic device. For metabolic imaging we performed 2-photon fluorescence lifetime imaging (FLIM) of intrinsically fluorescent metabolic coenzyme reduced nicotinamide adenine dinucleotide (NADH). We used 2-photon excitation of 740nm and the emission was collected between 420-500nm. Free and protein bound forms of NADH, which are well separated in fluorescence lifetime, are employed as indicators of cellular metabolism, especially glycolysis and oxidative phosphorylation. For analysis of lifetime data, we use the phasor approach to FLIM which a fit-free technique. We generate pseudo-colored FLIM map of the acquired image showing the linear distribution of bound and free fraction of NADH.

NADH FLIM-phasor was sensitive to detect changes of the whole tissue chamber in response to respiratory inhibitor cyanide. More importantly, the results demonstrate NADH FLIM of the 3D complex tissue-engineered structure could distinguish metabolically dissimilar areas at cellular level. We discovered the ECs forming vessels have a higher free to bound NADH ratio compared to the stromal cells and pericytes wrapping around those vessels. This aligns with the previous observation of endothelial cells metabolism being primarily aerobic glycolysis allowing oxygen to diffuse into deeper proliferating tissues [175]. NADH FLIM map of the whole tissue chamber incorporated with tumor cells clearly shows metabolic differences between cancer cells and the surrounding vessels and stromal cells. The breast

cancer cell lines MCF7 and MDA-MB231 and human colorectal cancer cell line HCT116 displayed higher free to bound NADH ratio compared to the ECs and supporting stromal cells in its microenvironment. We quantified this difference to be statistically significant. Interestingly, tumor cluster of colon cancer cell line SW620 did not display distinguishable metabolic map. Hence, this technique not only detected differences between tumor and its microenvironment, but also allowed us to compare the various cancer cells lines to themselves.

These results suggest there is a hierarchy of glycolytic rate from stroma (lowest), through EC, up to tumor (highest). There is a growing awareness of the potential for reducing tumor drug resistance through metabolic targeting[179,180]. Our data support the idea that reducing glycolysis may have some specificity for glycolysis-dependent tumors, and perhaps, their associated vasculature. In support of this, we found that 5-FU, while severely disrupting the NADH free/bound ratio in MCF-7 tumor cells had no effect on the stromal NADH free/bound ratio. Response of blood vessels to antiangiogenic drug was also easily identifiable with decrease in free/bound NADH ratio with drug treatment indicating a switch from its normal glycolytic behavior.

In conclusion, we demonstrate a powerful, non-invasive, label free optical metabolic imaging technique to evaluate three-dimensional tumor microenvironment establishment in a PDMS microfluidic platform. This non-destructive method allows monitoring such a system over time. Further, we could easily observe and quantify metabolic response to anti-cancer, and anti-angiogenic drugs at single cell level.

5.5 Chapter Summary

Development of microfluidic-device based microphysiological tissue system, which mimics human organs structurally and functionally, is gaining importance especially in the areas drug development, drug screening, and other healthcare research. Hence, there is a need for non-destructive techniques for understanding and evaluating such three-dimensional (3D) tissue models. In this work we present a non-invasive, label-free imaging technique to study metabolism of a vascularized human "tumor-on-a-chip". The model consists of tumor cells (tumor lines like breast cancer tumor lines MCF7 and MDA-MB231 and human colorectal cancer (CRC) cell line HCT116), supporting fibroblast and vascular network developed from endothelial cells in the diamond shaped tissue chamber of an optically clear polydimethyl siloxane (PDMS) based microfluidic device. For metabolic imaging we performed 2-photon fluorescence lifetime imaging (FLIM) of intrinsically fluorescent metabolic coenzyme reduced nicotinamide adenine dinucleotide (NADH). We used 2-photon excitation of 740nm and the emission was collected between 420-500nm. Free and protein bound forms of NADH, which are well separated in fluorescence lifetime, are employed as indicators of cellular metabolism, especially glycolysis and oxidative phosphorylation. For analysis of lifetime data, we use the phasor approach to FLIM which a fit-free technique. We generate pseudo-colored FLIM map of the acquired image showing the linear distribution of bound and free fraction of NADH. In the first part of the work, we show the ability to perform NADH FLIM of the microfluidic device tissue chamber and distinguish metabolically dissimilar areas. NADH FLIM map of the whole tissue chamber clearly shows metabolic differences between tumor cells and the surrounding vessels and stromal cells. The tumor cells exhibit higher free to bound NADH ratio pointing towards glycolytic behavior, which follows the

Warburg effect. To identify the different cells types, they were transfected with fluorescent proteins. Further, we could distinguish the more glycolytic vessels from the surrounding stromal cells which wrapped around the vessels. In the second part of this work we show the detection of metabolic response of the tumor microenvironment to drugs. In response to potassium cyanide, which is a known disrupter of respiratory mitochondrial transport chain, NADH FLIM map of the whole tissue chamber showed a shift towards higher free to bound NADH ratio indicating oxidative phosphorylation inhibition. Using this technique, we studied the effect of anti-cancer drug (5-FU). We observed a strong metabolic shift in MCF 7 cells after exposure of the tumor microenvironment to 100uM 5-FU for 96 hours. However, no such change was observed in the stromal cells. Anti-angiogenic drugs are often used in conjunction with anti-cancer drug to suppress the angiogenesis which aid tumor progression. Employing the NADH FLIM phasor technique we could study the effect of anti-angiogenic drugs like Sorafenib on the vasculature. Hence, in this work we demonstrate a powerful, non-invasive, label free optical metabolic imaging technique to evaluate 3D tumor microenvironment establishment in a PDMS microfluidic platform. This non-destructive method allows monitoring such a system over time. Further, we could easily observe and quantify metabolic response to anti-cancer, and anti-angiogenic drugs at single cell level.

Chapter 6

Label free FLIM-phasor fingerprint of clinically relevant bacteria

Chapter overview: In this chapter, while we maintain the theme of the thesis i.e., label-free FLIM, we apply this technique to medically relevant prokaryotes - bacteria. We establish phasor fingerprint of metabolically active bacteria as well as response to stimuli like antibiotic drugs and growth phases.

6.1 Introduction

Fluorescence lifetime imaging microscopy (FLIM) has been extensively exploited for label-free metabolic imaging in mammalian cells. However, FLIM of intrinsic fluorophores in live bacteria has not been explored to similar extents. In this chapter we address this issue and exploit FLIM phasor technique for bacterial metabolic imaging. This could prove important in understanding bacteria related pathology, drug response and therapy as well as emergence of newer drug-resistant bacterial strains, all in a label free manner.

There is a great diversity of bacteria species. They can have different size and shapes depending on their species. Further, they exist not only as single cells but also as clusters, microcolonies or form more complex biofilms. They are capable of adapting to their adverse environmental conditions and nutrient supply and can change their metabolic activity to weather such stresses. Hence, assessment of bacterial metabolism could shed light on their physiological status.

The motivation of the work presented in this chapter lies in the danger that these microorganisms pose to human health. While a large number of bacterial species are deemed beneficial, there is an increasing number of strains associated with pathology, including life threatening diseases. Some of these include tuberculosis, diarrhea, gastroenteritis, meningitis, bacteremia, dermatitis, gonorrhea, cellulitis, typhoid and pneumonia. Moreover, during the last decade, a large number of new infectious strains have been discovered. Treatment and therapy of these disease are often hindered by emergence multi-drug resistant bacterial strains[181,182]. Antibiotic resistance and tolerance are characteristics of the so called 'persister' cells which are often associated with biofilm formation and recurrence of bacterial infections [183–185]. Hence, in this work we asked the following question:

1. Can we identify and separate bacterial metabolic states when subjected to external stress or in their different growth phases?
2. Can we resolve this information at single cell level?
3. And finally, can we identify differences between cells of the same population, which maybe indicates presence of persisters?

To answer these questions non-invasively in the live bacteria within their native environment, we exploit autofluorescence of intrinsic fluorophores. As in the case of mammalian cells, bacteria have a plethora of endogenous fluorescent molecules with distinct spectral characteristics, rendering them as promising probes for identification and characterization. These include amino acids tryptophan, tyrosine and phenylalanine, and metabolic coenzymes reduced nicotinamide adenine dinucleotide (NADH), reduced nicotinamide adenine dinucleotide phosphate (NADPH), flavins and flavin adenine

dinucleotide (FAD)[186,187]. While these fluorophores are common for mammalian cells, some bacteria produce unique fluorescent molecules. For example, *Pseudomonas aeruginosa* strain PA14 produces pyocyanin (PYO), phenazine 1-carboxamide (PCN) and 1-hydroxyphenazine (1OHP). Fluorescence spectroscopy of intrinsic fluorophores has been previously explored in bacteria for detection, differentiating and characterizing different species[187–191]. Leblanc et al. (2002) used spectral signatures of aromatic amino acids + nucleic acids, tryptophan residues and NADH to differentiate between *Lactococcus lactis, Pediococcus pentosaceus, Kocuria varians, Pseudomonas fluorescens* and *Listeria innocua*[192]. Applying principal components analysis (PCA) technique to intrinsic fluorescence spectra, Giana et al. (2003) identified and separated the three bacterial species - *Escherichia coli*, *Enterococcus faecalis* and *Staphylococcus aureus* [193] , while Tourkya et al. (2009) demonstrated some separation between pseudomonads (Pseudomonas-like bacteria)[188]. Moreover, fluorescence emission from dipicolinic acid produced during spore formation could separate spore forming *Bacillus subtilis* from *Staphylococcus aureus*, a nonspore-forming bacteria[194].

Fluorescence spectroscopy of NADH in bacteria was published as early as the 1950s, roughly the same when the preliminary results on NADH fluorescence was demonstrated by Chance (details in Chapter 1). Using fluorescence spectrophotometry, Duysen et al. (1957) measured the fluorescence spectra of NADH in *Photobacterium phosphoreum*, *Photobacterium splendidum* and *Chlorella*[195]. Relation of metabolic state to NADH levels in bacteria were also investigated[196]. Harrison et al. reported oscillation of NADH fluorescence in *Klebsiella aerogenes* under certain conditions[197]. Wimpenny et al. investigated NAD and NADH levels in cultures of *Klebsiella aerogenes*, *Escherichia coli*, and *Staphylococcus albus* and demonstrated the relation of NAD/NADH ratio to growth, aerobiosis and anaerobiosis. De

Graef et al. too demonstrated the increase in ratio NADH/NAD in anaerobic condition as well as with decrease of dissolved oxygen tension[198]. NADH fluorescence to measure metabolic activity of bacteria has also been employed in water science research[199–201]. It is important to note that all the mentioned research was performed on bacterial cell suspensions and depicts results from the whole population.

As mentioned in the previous chapters, fluorescence lifetime measurements not only add another dimension to the data, it has several advantage over fluorescence intensity measurements. Importantly, it is independent of fluorophore's concentration, while at the same time dependent on its environment like temperature, pH, viscosity, and binding state. Hence, in this work we propose FLIM of bacterial NADH autofluorescence to study metabolic activity at single cell level in order to answer the questions posed at the beginning of this section. Some fluorescence lifetime measurement on bacteria have been previously reported with an attempt to detect and differentiate various bacterial species. Fluorescence lifetimes of bacteria *Staphylococcus epidermidis*, *Pseudomonas fluorescens*, *Enterobacter cloacae*, *Escherichia coli*, and *Bacillus subtilis* were measured with excitation wavelengths 340, 365, 405, 430 and 460 nm and emission detected at 430, 487, and 514 nm and reported in a series of publications[202–204]. The measurements were done in bacterial cell suspension using laser fluorometer. Kinkennon et al. reported autofluorescence lifetime profiles of *Pseudomonas fluorescens*, *Escherichia coli*, *Bacillus subtilis*, and *Staphylococcus epidermidis* employing multiharmonic Fourier transform phase-modulation fluorometer with excitation at 325, 364, and 442 nm. Fluorescence lifetime of tryptophan and NADH was employed recently for identification and classification of *Staphylococcus aureus*, *Pseudomonas aeruginosa*, *Salmonella typhi* and *Klebsiella pneumoniae*[205,206].

NADH FLIM phasor, as previously mentioned, has been extensively employed in metabolic imaging of mammalian cells including cancer metabolism, stem cell differentiation, cardiomyocyte metabolism and metabolic fingerprint of macrophage types[56,58,87,207]. FLIM phasor approach has also been applied to *Lactobacillus acidophilus*[208]. In this work we employ NADH FLIM-phasor to perform real-time metabolic imaging of clinically relevant bacteria, namely *Escherichia coli (E. coli)*, *Salmonella typhi (S. typhi), Pseudomonas aeruginosa (P. aeruginosa), Bacillus subtilis (B. subtilis),* and *Staphylococcus epidermidis (S. epidermidis)*. The first three are gram negative bacteria while the last two are gram positive. Some additional characteristic of these bacteria has been listed in Table 6.1. For the first time we show the lifetime phasor fingerprint of these bacteria with two-photon excitation of 740nm and emission collected at 460/80nm. Details of the phasor approach to FLIM has been discussed in chapter 2.

Our technique is sensitive to metabolic response of the bacteria when subjected to the two classes of antibiotics: bacteriostatic and bactericidal. Moreover, the FLIM phasor show reverse response upon drug recovery. We also defined metabolic fingerprint associated with the different growth phases in the bacteria. Finally, we demonstrate the metabolic shifts when growth is resumed from the stationary phase.

Our method is advantageous due to the fact that we can study metabolic state of bacteria at single cell level. We can obtain information about individual cells in the imaging plane and observe changes temporally and spatially. Differences between cells in the same population can also be identified, perhaps directing towards bacterial cells which might be persisters. This technique gives powerful insights about the microorganism's metabolic diversity due

Table 6.1 Characteristics of bacteria explored in this thesis

Species name	**Group by Gram staining**	**Shape**	**Related disease**
Escherichia coli	Gram negative	rod-shaped	virulent stains cause gastroenteritis, diarrhea, septicemia, meningitis
Salmonella typhimurium	Gram negative	rod-shaped	typhoid or enteric fever, food poisoning, gastroenteritis
Pseudomonas aeruginosa	Gram negative	rod-shaped	opportunistic infection, pneumonia, urinary tract infection
Bacillus subtilis	Gram positive	rod-shaped	non-pathogenic, pathogenic *Bacillus* organism include Bacillus *cereus, Bacillus licheniformis* and Bacillus anthracis
Staphylococcus epidermis	Gram positive	sphere-shaped	nosocomial infections in catheters and implants, prosthetic valves, cerebrospinal fluid shunts, joint prosthesis, vascular prostheses

to its excellent sensitivity and selectivity. Further, owing to its nondestructive nature, bacterial metabolic states can be probed in their native environment.

6.2 Material and methods

6.2.1 FLIM acquisition

FLIM was performed on a Zeiss LSM 710 microscope (Carl Zeiss, Jena, Germany) using a 40x, 1.2 N.A. water immersion objective, (Carl Zeiss, Oberkochen, Germany) coupled to an 80MHz multiphoton excitation laser source, Titanium:Sapphire MaiTai laser (Spectra-Physics, Mountain View, CA). 2PE (2 photon excitation) excitation of NADH and LLS was carried out at 740nm. Image scan speed was 25.21 µs/pixel with an image size of 256 × 256 pixels. A

dichroic at 690 nm was employed to separate excitation from emission signal. A bandpass emission filter 460/80nm (Semrock, Rochester, NY) coupled to a photomultiplier tube (H7422P-40, Hamamatsu, Japan) was used as the microscope external detector port photo-sensor unit. FLIM data was acquired using A320 FastFLIM FLIMbox (ISS, Champaign, IL). For each image, 60 - 70 frames were collected and integrated for FLIM analysis. SimFCS software (LFD, Irvine) was used for frequency domain FLIM data acquisition. For calibrating the FLIM system, Rhodamine 110 with known lifetime of 4ns was measured for every experiment. All the (g, s) coordinate system used to mention phasor cursor coordinates in this article used the first harmonic phasor plots at 80Mhz (repetition rate of the laser).

6.2.2 Sample

Five bacterial species were used for this project namely: *Escherichia coli* (MC4100), *Salmonella typhimurium* (AJB52), *Pseudomonas aeruginosa* (PA14 WT), *Bacillus subtilis* and *Staphylococcus epidermidis*. All strains were revived from frozen stocks by streaking on Lysogeny broth (LB) agar plates. 1.5% agar was used. Shaking cultures of bacterial strains were grown in 2 ml LB for 5 hours unless stated otherwise.

For imaging, the samples were prepared by mixing LB shaking cultures with 1% agarose in 3:7 ratios. 100 μl of the solution was dropped on a glass coverslip and spin coated at 500 rpm for 10 seconds.

6.2.3 Growth curve measurement

Optical densities (OD) of 1 ml bacterial shaking was measured every hour to generate a growth curve. The OD was measure at 600nm wavelength of light using a Biowave CO8000 cell density meter (Biochrom, Holliston, MA).

6.2.4 Data analysis

FLIM data was analyzed using the SimFCS software developed at the Laboratory of Fluorescence Dynamics (LFD, UC Irvine) was used. Additional data processing was performed on MATLAB.

6.3 Results

6.3.1 Bacterial fluorescence lifetime phasor fingerprint

We investigated two photon FLIM of five clinically relevant species of bacteria - *Escherichia coli (E. coli), Salmonella typhimurium (S. typhimurium), Pseudomonas aeruginosa (P. aeruginosa), Bacillus subtilis (B. subtilis), and Staphylococcus epidermidis (S. epidermidis)*. Each species was imaged at an early logarithmic phase of growth, deemed to be metabolically active. Fig 6.1 shows the phasor fingerprint of the bacterial species (n=10). The position of the bacteria phasor defines the phasor fingerprint of metabolically active state of the bacteria. This might represent corresponding degree of free to bound NADH ratios in that particular time of growth. A comparative analysis of all the phasor coordinates of each bacteria shows variation in position along both g and s axes of the phasor plot [Fig 6.1 (c)]. The distribution of coordinates generated by the bacterial phasors indicate greater variation along the g axis (between 0.3 to 0.45) than the s axis on the phasor plot.

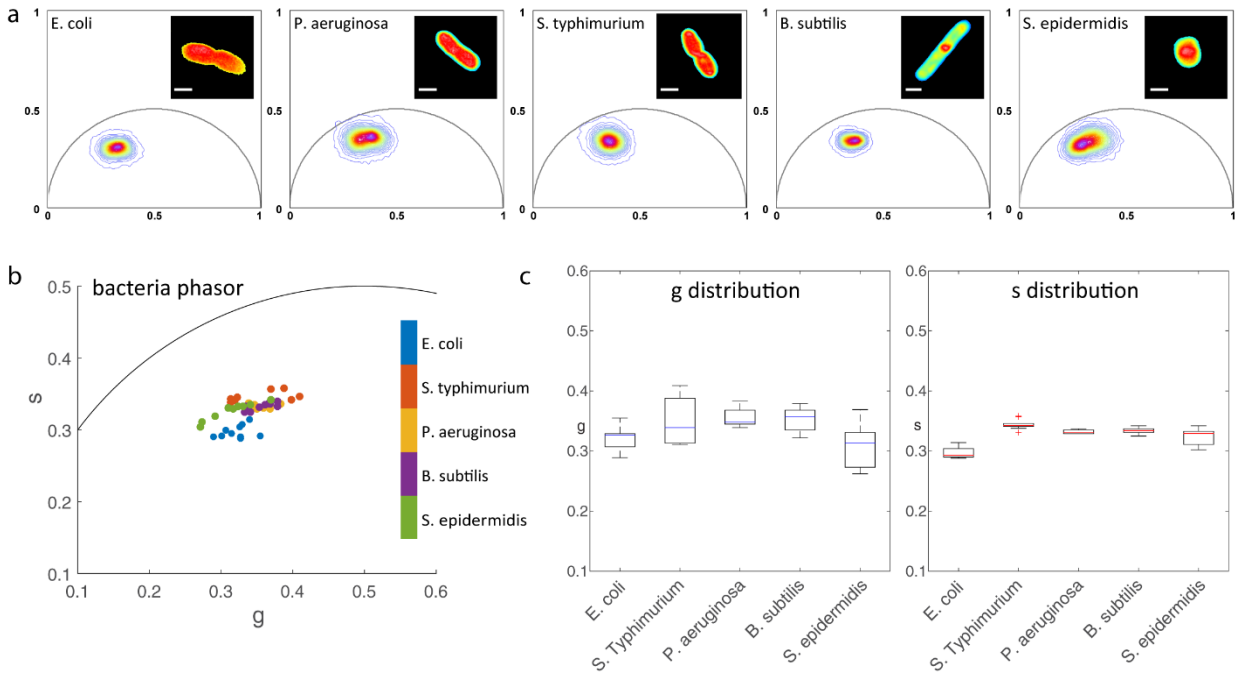

Fig 6.1 Bacterial phasor fingerprint. (a) Phasor distribution of *Escherichia coli* (*E. coli*), *Salmonella typhimurium (S. typhimurium), Pseudomonas aeruginosa (P. aeruginosa), Bacillus subtilis (B. subtilis)*, and *Staphylococcus epidermidis (S. epidermidis*). Inset panels are representative fluorescence intensity images of each bacterium with 2-photon excitation of 740nm. Scale bar is 1µm. (b) Bacteria phasor fingerprint, n=10. (c) Boxplot representation of g and s distribution.

6.3.2 Response to bacteriostatic antibiotic and recovery

After establishing bacterial phasor fingerprint we examined the response of the bacteria when exposed to antibiotic drugs. We chose *E. coli* for this experiment as it is considered to be the model organism. Fig6.2 (a) is the phasor distribution of control and *E. coli* subjected to of 50µM, 100µM, 200µM, 300µM and 500µM nalidixic acid, a bacteriostatic drug. Each exposure was for 30mins. Two distinct phasor clusters were observed. The longer lifetime cluster is chosen by green cursor. This selection corresponds to the control and a few bacteria in the 50 µM treated group [Fig 6.2 (b)]. The right shifted phasor cluster is chosen by the red cursor which corresponds to the nalidixic acid treated

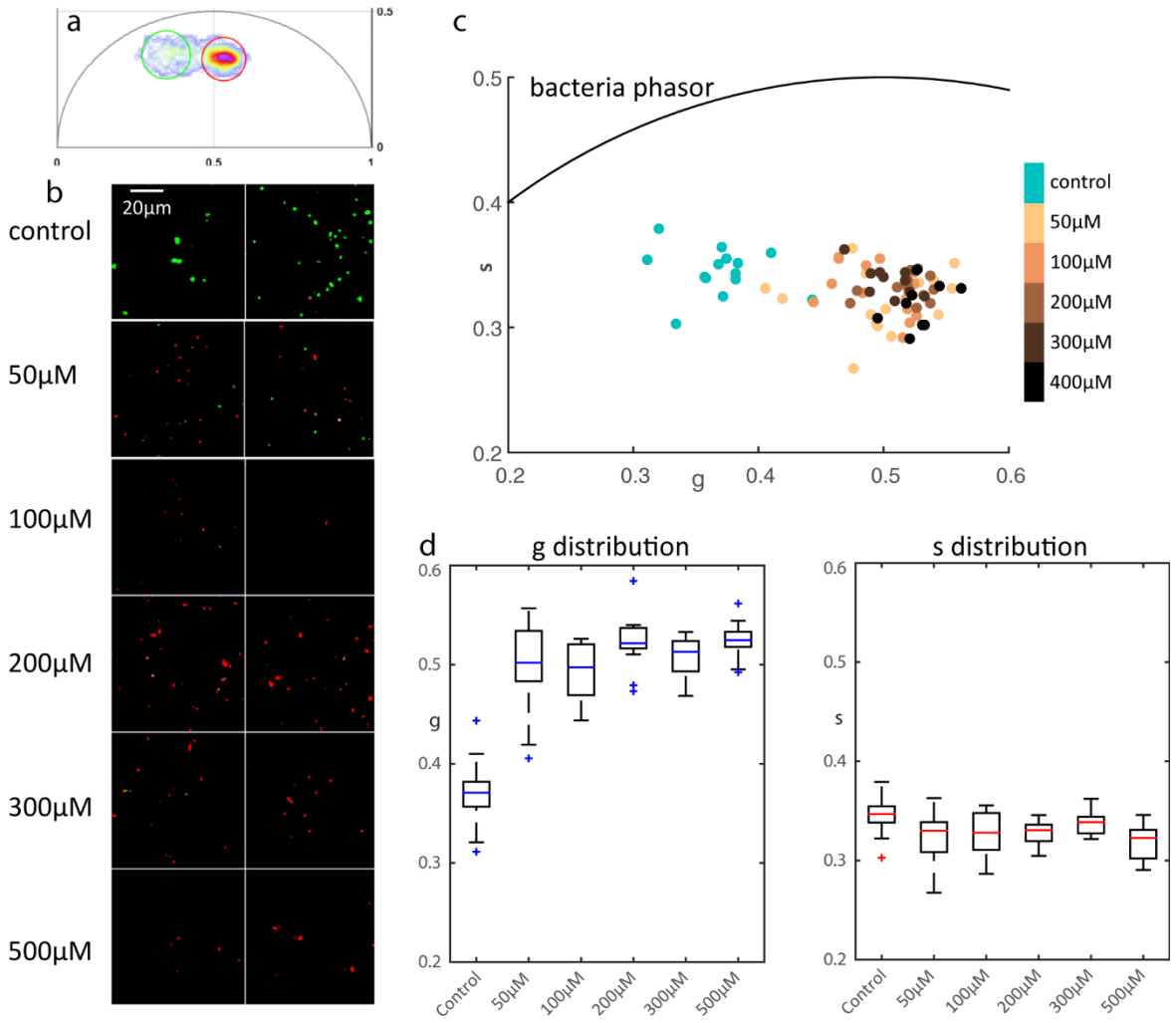

Fig 6.2 Response to bacteriostatic treatment. (a) Phasor distribution of *E. coli* control and treated with 50μM, 100μM, 200μM, 300μM and 500μM nalidixic acid. Green cursor selects phasor distribution on the left while red cursor selects that on the right. (b) FLIM map created by red and green cursors in (a). (c) Bacteria phasor in each condition. (d) g and s distribution of bacterial phasor in each condition

groups. Fig 6.2 (c) shows the average g and s value of each individual bacteria with green dots representing bacteria in control group and the bacteria subjected to increasing concentrations of nalidixic acid is represented by light to darker shades of brown. The phasor fingerprint shifted towards right when logarithmic growth phase *E. coli* cells were exposed to the bacteriostatic antibiotic nalidixic acid. The progressive right shift was dose dependent, i.e., increasing shift towards the free NADH phasor position was observed with

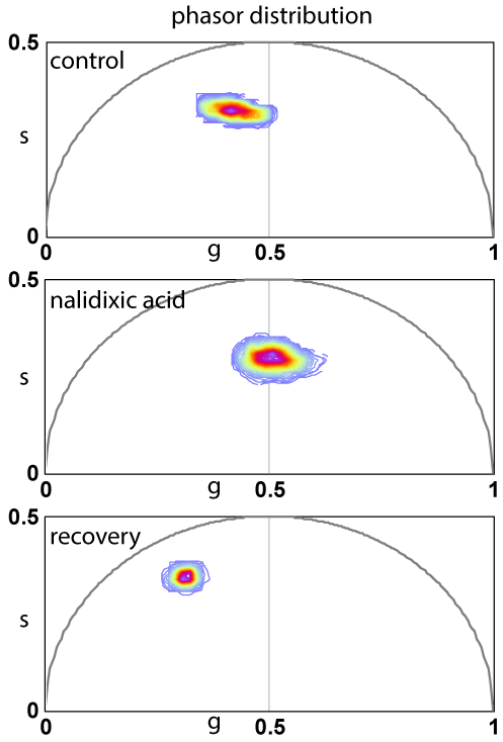

Fig 6.3 Bacteriostatic antibiotic recovery. Phasor distributions *of E. coli, E. coli* treated with 200µM nalidixic acid of 30mins and resuspended in normal media for 30mins

increasing concentration of nalidixic acid as seen in Fig 6.2 (c). Fig 6.2 (d) shows the distribution of the phasor coordinates along the g and s axes as a function of concentration of nalidixic acid. The g distribution had an increasing mean value while that along s axis was fairly constant as a function concentration.

A bacteriostatic antibiotic inhibits growth of the bacterium which can be restored upon removal of unfavorable conditions. To investigate if the bacterial phasor recovers from the exposure to a bacteriostatic antibiotic, *E. coli* was subjected to 200µM nalidixic acid for 30 minutes and imaged. Following this, the exposed *E. coli* cells were washed and incubated in growth media for 30mins and imaged again. Fig 6.3 shows the phasor distribution of control, treated, and drug removed groups. As observed in the previous experiment, drug exposure

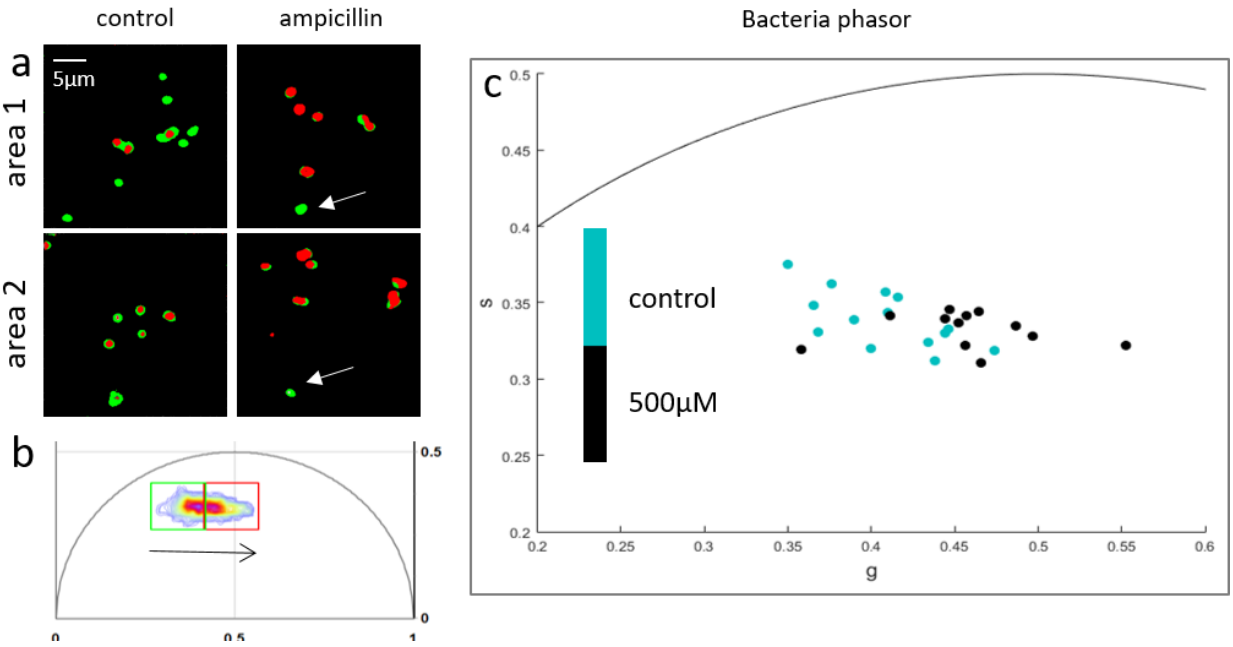

Fig 6.4 Response to bactericidal antibiotic. (a) FLIM map of two areas of *E. coli* control and 500μM ampicillin created by the square cursor in the phasor plot (b). Red and green cursors divide the phasor distribution at the center. Black arrow shows the direction of shift after drug administration. (c) Single bacteria phasor.

shifts the phasor to the right indicating higher free/bound NADH ratio. The phasor distribution of bacteria when the drug was removed shifts back towards the left indicating lower free to bound NADH ratio. Exposure of *E. coli* to antibiotics showed greater shifts along the g axis of the phasor plot. Hence the recovery upon drug removal could be identified by FLIM phasor shifts. It is interesting to note that the phasor distribution along the g axis is wider for control and treated groups, representing more diversity in metabolic states of bacteria within the same group. However, in the recovered group, this variation is much reduced as indicated by a narrower phasor distribution. Perhaps the treatment reset the metabolic state of all the cells to a similar starting point.

6.3.3 Response to bactericidal antibiotic

The encouraging results of FLIM phasor sensitivity to bacteriostatic antibiotic treatment led us to expose *E. coli* to another class of drug called the bactericidal antibiotic. Once again, we could detect response of the bacteria to the antibiotic. Fig 6.4 (a) shows the FLIM map, color coded according to the cursor selections on the phasor plot in Fig 6.4 (b). The bacteria with green pixels have phasor selected by green cursor with lower g values than the red pixels that have their corresponding phasor inside the red cursor. Thus, NADH FLIM phasor for *E. coli* exposed to a bactericidal antibiotic, ampicillin shows a similar shift towards higher free to bound NADH ratio. The direction and extent of the shifts are similar to NADH FLIM phasor of *E. coli* cells exposed to bacteriostatic antibiotics. Fig 6.4 (c) shows single bacteria phasor of the two groups. This technique revealed the response of each bacterium to the drug. In the exposed group, we found bacteria which does not show a shift like the rest of the group (indicated by white arrows in Fig 6.4 (a)). Perhaps these are persister like cells which were resistant to the antibiotics.

6.3.4 NADH FLIM of Bacterial Growth Curves

To track the change in phasor position at different growth stages in bacteria we imaged 4 different species of bacteria, *Escherichia coli (E. coli), Salmonella typhimurium (S. typhimurium), Pseudomonas aeruginosa* (*P. aeruginosa*), and *Bacillus subtilis* (*B. subtilis*), Fig 6.5 (a-b). The growth stages of these bacterial cultures were tracked in parallel using the traditional optical density (OD) measurements, Fig 6.5 (c). The initial direction of the shift with increase in growth of the bacterium was towards a higher free to bound ratio of NADH. From the lag phase till the log phase (from 2 hours to about 8 hours), we observed a right

shift of phasors till the phasor position of the metabolically bacteria fingerprint (i.e., g in the range of 0.3 to 0.5). From the onset of stationary phase, the phasor started shifting left towards higher lifetimes in an oscillatory fashion. Different extends of this oscillatory trend in phasor shifts was observed in growth curves of all the 4 species of bacteria, though the oscillations were slightly reduced in case of *P. aeruginosa* Fig 6.5 (b).

6.3.5 Growth curve recovery

To investigate if the oscillatory shifts retrace the same path back, *E. coli* cells grown for 15 h, 24 h, 48 h and 307 h (13 days). Each were divided into two groups. One group continued to grow in the same old culture media for 2 more hours. The second group was washed and resuspended in equal amount of fresh growth media and allowed to grow at 37° C for 2 hours. Fig 6.6 shows the bacteria phasor of each group. Cyan points represent individual bacteria growing in old culture while black points indicate bacteria from the same group resuspended in fresh media. We observed an increase in NADH free to bound ratio in the groups resuspended in fresh media when compared to its corresponding old culture media group. This was shown by a right shift in the bacteria phasors of the recovered groups towards the phasor fingerprint of metabolically active bacteria fingerprint position (i.e, g between 0.35 to 0.5). However, there was a decrease in the extent of this change with increase in growth time indicating less and less ability of the bacteria to recover. *E. coli* cells grown for 307 h did not show any recovery from the NADH FLIM phasor position. Decreasing amount of recovery as well as a right shift within 17h, 26h, 50h, and 13 days might be due to the fact that these groups contain survivor bacteria which are more metabolically active while the weaker cells of the groups are already dead and do not contribute to the data

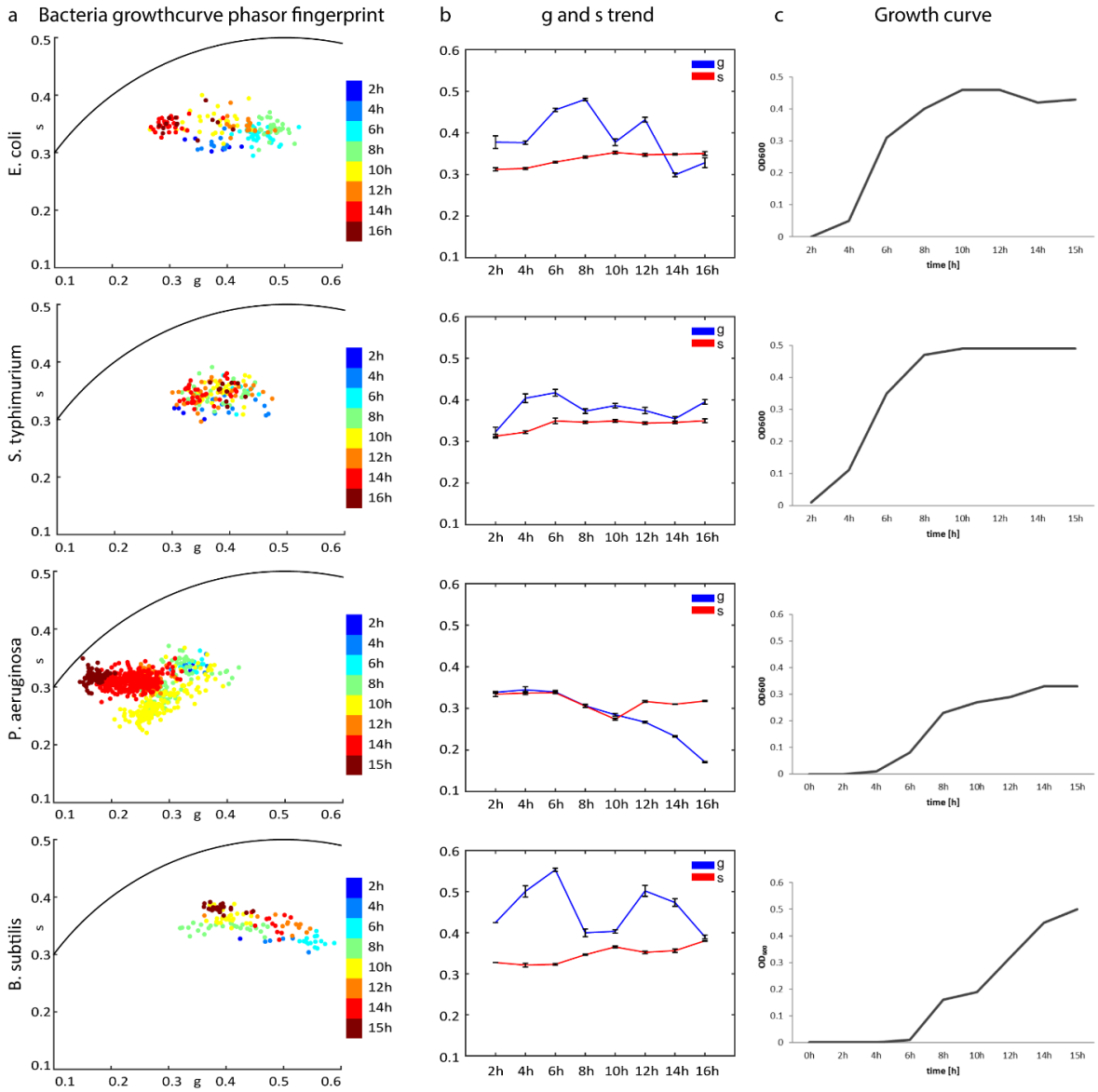

Fig 6.5 Growth curve phasor fingerprint. (a) bacteria phasor *of Escherichia coli (E. coli), Salmonella typhimurium (S. typhimurium), Pseudomonas aeruginosa (P. aeruginosa), and Bacillus subtilis (B. subtilis*) at different stages of the growth curve color coded by rainbow scale. (b) g and s trend of the 4 bacterial species. (c) Growth curve by optical density (OD) measurements.

6.4 Discussion

In this work we employ label-free NADH FLIM to characterize fluorescence lifetime fingerprint of bacteria with cellular resolution. The phasor approach to FLIM proves to be a powerful tool to elucidate metabolic states of bacteria species and correlate them with stress

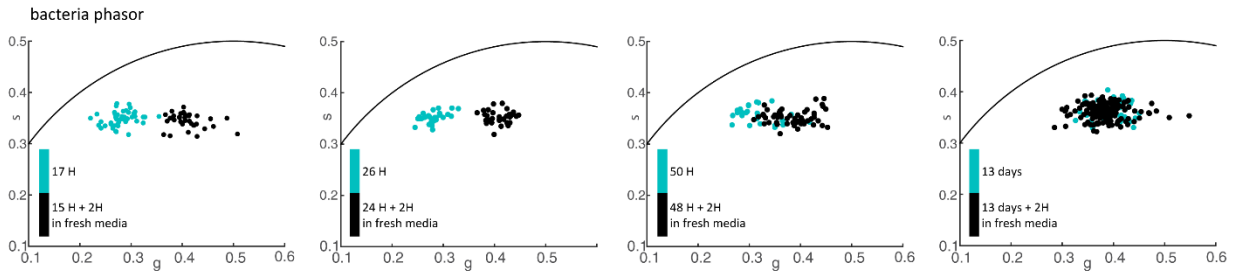

Fig 6.6 Growth recovery. Bacteria phasor of *E. coli* in 17 hours, 26 hours, 50 hours and 13 days culture compared to 15 hours 24 hours, 48 hours and 13 days culture resuspending in fresh growth media for 2 hours.

response and cell death. Mid log phase bacterial cells of *E. coli, P. aeruginosa, B. subtilis, S. typhimurium* and *S. epidermis* were used to generate the bacterial species fingerprint phasor as that phase represents a high metabolic activity. The lifetime phasor fingerprint varies within different species of bacteria and also within a population of same species. This supports previous literature indicating differing metabolic pathways of different species of bacteria[209–211]. Diversity in metabolism results in different ratios of NAD/NADH and enzyme complexes of NADH which perhaps account for the differences of phasor position among different species of bacteria[197,198,212,213]. Bacterial cells within a population of the same species can be at different metabolic states of growth, resulting in formation of different NADH enzyme complexes within the population. This might account for the diversity of phasor position of each bacteria of the same species.

Bacteria encounter various stresses in their natural environments and they elicit specific and highly regulated responses via changes in their metabolism[183,185,214,215]. We probed the metabolic response of *E. coli*, which is considered as a model organism to antibiotic treatment. Administration of both bacteriostatic drug (nalidixic acid) and bacteriocidal drug (ampicillin) caused a right shift of the lifetime phasor distribution. This shift of the NADH phasor position towards shorter lifetimes in response to different antibiotics and

bactericidal compounds appears to be characteristic of exposure to such high stress environment and may be indicative of cell death. The shift of the phasor is towards higher free NADH fraction may be due to shutting down of cellular metabolism at higher concentrations of antibiotics. In the event of cell death such state is irreversible; however bacterial cells are known to recover from a state of static growth and dormancy induced by bacteriostatic compounds[215–219]. We observed a return of the phasor distribution, represented as a left shift, when *E. coli* cells where exposed to lower concentration of nalidixic acid followed by washing off the drug with media and resuspension in nutrient medium. This observation further corroborates that a shift of the phasor position towards free NADH lifetime is characteristic of bacterial stress response leading to cell death. Moreover, the distribution of the recovered bacteria was much tighter than the control and treated population. This decrease in variation probably indicates similar metabolic state of all the bacteria subjected to the treatment as opposed to control cells which might be at varying metabolic states. The response of a bacterial cell in a high stress environment depend on a range of factors like rate of cell division, metabolic state and so on[215,220]. Such factors direct the fate of part of the cell population towards persister or dormant state and the rest towards death. This results in a wide spread of the phasor distribution of the bacterial cell.

A bacterial growth curve defines the metabolic state of a population of particular species of bacteria over time[221,222]. In the case of most aerobically grown bacteria, this depends on the type of nutrient source, temperature of growth, rate of aeration and so on, and is characterized measuring optical density at 600nm wavelength of light using a spectrophotometer[223]. The bacterial growth curve extends further than the commonly

described lag, log (or exponential) and stationary phases of growth[221,222,224]. Most importantly each bacterium within population experiences differential rates of growth and this information cannot be obtained using optical density or counting CFU characterization techniques. The growth curve beyond the stationary phase is complicated by persister cells and growth advantage in stationary phase (GASP) phenotype formation, changes in gene expression and morphology, programmed cell deaths occurring in a culture[225–227]. Effects of these events have been characterized over long periods of time using optical density measurements. However, cells begin to starve at the onset of the stationary phase when nutrition from growth media begin to decrease and the cell microenvironment is no longer favorable. We employed NADH FLIM phasor to characterize the metabolic state of 4 bacterial species at different time point of growth. From lag phase to exponential phase we identified a right shift of the phasor distribution reaching the fingerprint position of metabolically active species. Subsequently, at later stages of exponential phase into the stationary phase we observed an oscillation of the phasor positions. Bacterial cultures display an oscillatory behavior of cell density in the culture with rise and fall during the stationary phase[220,224–227]. This has been explained by the GASP phenomenon where dead populations provide nutrients to their living counterparts increasing the cell density for a small period of time. This phenomenon continues until all cells in a culture are dead. The growth curve phasors show a general trend where they move towards longer lifetimes at the onset of the stationary phase. The observed trend in the growth curves at the onset of stationary phase may be due to GASP phenomenon in the cultures where cells receive nutrients due to death of a sub-population of cells. Interestingly, the phasor positions of older cultures (15hours, 24 hours and 48 hours) recover back to that of a metabolically active bacteria phasor fingerprint when

resuspended in fresh media. Moreover, this recovery becomes less evident with increasing culture time. Cells in 13 days old culture did not show any recovery indicating that most cells are dead and there is no nutrient available.

In conclusion, we demonstrate label free two-photon fluorescence lifetime microscopy of bacteria. We create a lifetime phasor fingerprint of clinically relevant bacteria. To the best of our knowledge, this is the first time two-photon phasor fingerprinting of bacteria species Escherichia *coli, Pseudomonas aeruginosa, Salmonella Typhimurium, Bacillus subtilis* and *Staphylococcus epidermis* have been demonstrated. Our technique could detect response of bacteria to external stress at single cell level. Further we show the lifetime phasor trajectories of bacterial growth curve phases. This technique gives powerful insights about the microorganism's metabolic behavior due to its excellent sensitivity and selectivity. Owing to its nondestructive nature, bacterial metabolic states could be probed in their native environment.

6.5 Chapter Summary

In this chapter we demonstrate label free two-photon fluorescence lifetime microscopy of bacteria. We create a lifetime phasor fingerprint of clinically relevant bacteria. To our knowledge, this is the first time two-photon phasor fingerprinting of bacteria species *Escherichia coli*, *Pseudomonas aeruginosa*, *Salmonella* Typhimurium, *Bacillus subtilis* and *Staphylococcus epidermis* have been demonstrated. Different bacterial species utilize different metabolic pathways under varying environmental conditions. This results in differences in metabolic states which could be depicted by NADH FLIM phasor. We were able to show differences not only between species but also within the same species at single cell level. Next, we examined response of the model organism, *Escherichia coli*, to antibiotic treatment. When subjected to both bacteriostatic and bactericidal antibiotic, we observed right shift towards free NADH phasor fingerprint on the phasor, from the position of control bacteria with high metabolic activity. Recovery of the bacteria treated upon resuspension in normal media was indicated by a left shift. This lead us to believe the right shift is characteristic of exposure to high stress environment and may be indicative of cell death. Interestingly, we noticed some cells whose phasor position did not change with antibiotic exposure, perhaps indicating 'persistence' nature. Hence, our technique could to detect response of bacteria to external stress at the single cell level. Further, we show the lifetime phasor trajectories of bacterial growth curve which is defined by the metabolic state of a population of particular species of bacteria over time. From the lag phase till the log phase, we observed a right shift of phasors till the phasor position of the metabolically bacteria fingerprint. From the onset of stationary phase, the phasor shifted left towards longer lifetimes in an oscillatory fashion. We also show recovery of resuspended bacteria. This

technique gives powerful insights about the microorganism's metabolic behavior due to its excellent sensitivity and selectivity. Owing to its nondestructive nature, bacterial metabolic states could be probed in their native environment. Interestingly, the phasor positions of older cultures (15hours, 24 hours and 48 hours) recover back to that of a metabolically active bacteria phasor fingerprint when resuspended in fresh media. Cells in 13 days old culture did not show any recovery indicating that most cells are dead and there is no nutrient available. Hence we demonstrate a powerful non-invasive imaging technique to study bacterial metabolism and characterize the phasor fingerprint of bacteria under various conditions.

Chapter 7

Conclusion and future direction

Chapter overview: This is the concluding chapter of the thesis which summarizes the work discussed in this thesis followed by suggestions on future directions that could be pursued.

7.1 Conclusion

Understanding cellular metabolism, its regulation, and its influence on normal and pathological cell physiology coupled with investigation of oxidative stress in pathogenesis of these human diseases is an important area of biomedical research. In this thesis frequency – domain fluorescence lifetime imaging microscopy (FLIM) was employed to probe biological systems exploiting naturally occurring fluorophores. The FLIM technique has existed in the field of biomedical optics for the past several decades, yet much is left to be explored. The purpose of the work was to effectively utilize this powerful label-free, non-invasive tool to study metabolism and stress in a wide range of biological samples.

In Chapter 3, we established for the first time, a novel oxidative stress detection technique by FLIM of an endogenous fluorophore with unique fluorescence lifetime. In this work, FLIM-phasor served as a tool of discovery of this intrinsic species with characteristic long lifetime (LLS). We hypothesized the origin of this FLIM signal was due to lipid oxidation by reactive oxygen species (ROS) and we went on to prove it by exploiting non-linear optical microscopy techniques already well established for lipid imaging - Third harmonic generation (THG) imaging microscopy and coherent anti-Stokes Raman scattering (CARS) microscopy. All of these

techniques have the advantage of being label-free and non-invasive and could be correlated to the results of FLIM. We went one step further to characterize the chemical nature of this discovered species by classical Raman spectral analysis. We also show an application of this technique to detect cancer related oxidative stress. Moreover, we demonstrate its sensitivity to oxidative stress imaging in live tissue samples. This technique could prove tremendously advantageous, especially for *in vivo* measurement as it relies completely on intrinsic fluorophores.

Chapter 4 demonstrated for the first time, simultaneous label-free metabolic and oxidative stress imaging in human induced pluripotent stem cell derived cardiomyocytes (hiPS-CM) upon application of pathological stimuli of hypoxia and cardiotoxic drugs. NADH FLIM-phasor could detect metabolic response of hiPS-CMs to respiratory inhibitor drugs and hypoxic conditions. Moreover, we detected long lifetime species (LLS), indicating oxidative stress in the cells, the amount of which increased with the duration of hypoxia. This method could prove beneficial for drug development and screening studies, especially for *in vitro* cardiac models derived from stem cell-derived cardiomyocytes.

Currently, tissue engineered organs-on-a-chip is one of the most promising avenues of biomedical research. However, development of such models requires non-invasive assessment and evaluation of the physiology. Moreover, application of these models as platforms for drug discovery and drug screening requires non-destructive readouts. In Chapter 5 we take a big leap closer to this goal by demonstrating metabolic imaging of a vascularized three-dimensional tumor microenvironment in a microfluidic based platform. We could identify metabolically dissimilar regions within the tissue chamber arising from tumors, microvessels formed by endothelial cells, as well the surrounding stromal cells.

NADH FLIM-phasor displayed excellent sensitivity towards detecting metabolic response to anticancer and anti-angiogenic drug administration, all of which could be quantified.

In the last chapter, equipped with our efficient tools for label-free fluorescence lifetime imaging, we knocked on the doors of a different organism – the prokaryotes. FLIM of intrinsic fluorophores in live bacteria has not been explored as extensively compared to mammalian cells. Hence, in Chapter 6, we exploit FLIM phasor technique for bacterial metabolic imaging. This could prove important in understanding bacteria related pathology, drug response and therapy as well as emergence of newer drug-resistant bacterial strains, all in a label free manner. We created lifetime phasor fingerprint of five clinically relevant bacteria at their metabolically active phase of growth. We also tracked trajectories of bacterial phasors at different stages of growth from lag phase to stationary phase. We discovered interesting trajectories with initial linear nature till onset of stationary phase followed by oscillatory behavior. Moreover, FLIM phasors exhibited shifts with treatment with antibiotics which was retraced back upon drug recovery. Another potential advantage of this technique was the single cell resolution. Bacterial cells with diverse metabolic states were easily identified with wide phasor distribution. Further, specific cells which were resistant to antibiotics treatment could be immediately identified from the population. Thus in this chapter we demonstrate a powerful non-invasive imaging technique to study bacterial metabolism and characterize the phasor fingerprint of bacteria under various conditions.

7.2 Future directions

The results and discoveries unfolded in thesis exposed several future directions and opportunities to be explored using label-free fluorescence lifetime imaging microscopy

(FLIM). While we demonstrated the novel oxidative stress imaging technique, this is just at its infancy. A number of research areas that could be probed include detection of melanoma in live animal, investigation of adipocytes in obesity related diseases like diabetes, oxidative stress related to embryogenesis, and neurodegenerative diseases. Recently we demonstrated the capability of NADH-FLIM to differentiate between macrophage types[207]. This could be extended along with lipid oxidation detection in atherosclerotic plaque and to study its development. We demonstrated application in freshly excised adipose tissue, however, this can be translated to in vivo imaging. Current techniques of ROS measurement especially with exogenous fluorescent dyes do not provide the same richness of information. Moreover, certain characteristics of the dye including its solubility in lipid versus aqueous environment, ability to cross biological membranes, sample preparation and required time for incubation, influences of physiological conditions like temperature and pH, and so on, are essential determinants of usefulness of the fluorescent dye[109]. Moreover, there is always the difficulty of the dye being equally distributed in all the cellular location inside the tissue. If trapped in certain pockets, it might not give the true picture of oxidative stress in the tissue of interest.

From technical point of view, a better understanding of the origin of the fluorophore is required. Destructive chemical analysis techniques like mass spectrometry might not be accurate for this application since we discovered the presence of the long lifetime species (LLS) in only a subset lipid droplet. Matrix-Assisted Laser Desorption Ionization (MALDI) imaging mass spectrometry offers chemical analysis while preserving spatial location[228]. This technique could be explored with simultaneous FLIM for precise identification of LLS

location in the sample, but the spatial resolution is not sufficient to resolve single lipid droplets.

We demonstrated metabolic imaging of tissue engineered tumor-on-a-chip model. These promising results could be extended further in tissue engineering to study metabolic changes during angiogenesis, tumor cell migration, as well as multi-tissue co-cultures. For example, we could study the simultaneous effect of anticancer drug on tumor and cardiotoxicity of the same drug in a cardiac microenvironment employing a dual tissue chamber model[229]. Robust metabolic imaging in complex 'human-on-a-chip' models[230] can be possible due to the ease with which this two-photon microscopy technique can be applied to complex 3D structures. Simultaneous second harmonic generation (SHG) and third harmonic generation concomitant with FLIM could give us real time information in a nondestructive manner.

Finally, we investigated the FLIM-phasor technique in metabolic fingerprinting of bacteria. This unveils opportunities to study and understand bacterial pathogenesis. Real time imaging of bacterial infection, including simultaneous metabolic response of bacteria as well as host cells could be easily performed. Moreover, recently we extended this technique to bacterial biofilm which displayed phasor fingerprint distinct from the single cell stage. Bacterial biofilm formation and detection in biomedical implant infections a prominent subject of research[231,232]. The label-free nature of FLIM phasor could have great potential in biofilm research.

In conclusion, label free metabolic and oxidative stress imaging employing FLIM is a promising technique in the field of biomedical optics and can bring about tremendous progress in biology, biomedicine as well as translational medicine.

Bibliography

1. DeBerardinis, R. J. & Thompson, C. B. Cellular metabolism and disease: what do metabolic outliers teach us? *Cell* **148,** 1132–44 (2012).

2. Vander Heiden, Matthew G., Cantley, Lewis C., and Thompson, C. B. Understanding the Warburg Effect: The Metabolic Requirements of Cell Proliferation. *Science (80-.).* **324,** 1029–1033 (2009).

3. Warburg, O. On the Origin of Cancer Cells On the Origin of Cance. *Source Sci. New Ser.* **123,** 309–314 (1956).

4. Metallo, C. M. & Vander Heiden, M. G. Understanding metabolic regulation and its influence on cell physiology. *Mol. Cell* **49,** 388–98 (2013).

5. Khairallah, M., Danialou, G., Petrof, B. J., Rosiers, C. Des & Bouchard, B. Profiling substrate fluxes in the isolated working mouse heart using 13 C-labeled substrates : focusing on the origin and fate of pyruvate and citrate carbons. **1,** (2004).

6. Cairns, R. a, Harris, I. S. & Mak, T. W. Regulation of cancer cell metabolism. *Nat. Rev. Cancer* **11,** 85–95 (2011).

7. Cantor, J. R. & Sabatini, D. M. Cancer cell metabolism: one hallmark, many faces. *Cancer Discov.* **2,** 881–98 (2012).

8. Almendro, V., Marusyk, A. & Polyak, K. Cellular heterogeneity and molecular evolution in cancer. *Annu. Rev. Pathol.* **8,** 277–302 (2013).

9. Datta, R., Alfonso-García, A., Cinco, R. & Gratton, E. Fluorescence lifetime imaging of endogenous biomarker of oxidative stress. *Sci. Rep.* **5,** 9848 (2015).

10. Harman, D. Aging: A Theory Based on Free Radical and Radiation Chemistry. *J. Gerontol.* **11,** 298–300 (1956).

11. D'Autréaux, B. & Toledano, M. B. ROS as signalling molecules: mechanisms that generate specificity in ROS homeostasis. *Nat. Rev. Mol. Cell Biol.* **8,** 813–24 (2007).

12. Finkel, T. Signal transduction by reactive oxygen species. *J. Cell Biol.* **194,** 7–15 (2011).

13. Dröge, W. Free radicals in the physiological control of cell function. *Physiol. Rev.* **82,** 47–95 (2002).

14. Alonso, A., Marsal, S. & Julià, A. Analytical methods in untargeted metabolomics: state of the art in 2015. *Front. Bioeng. Biotechnol.* **3,** 23 (2015).

15. Griffin, J. L. & Shockcor, J. P. Metabolic profiles of cancer cells. *Nat. Rev. Cancer* **4,** 551–61 (2004).

16. Ishikawa, T.-O. *et al.* Positron emission tomography imaging of DMBA/TPA mouse skin

multi-step tumorigenesis. *Mol. Oncol.* **4,** 119–25 (2010).

17. Smyth, E. C. & Shah, M. a. Role of ^{18}F 2-fluoro-2-deoxyglucose positron emission tomography in upper gastrointestinal malignancies. *World J. Gastroenterol.* **17,** 5059–74 (2011).

18. Qu, W. *et al.* Synthesis of optically pure 4-fluoro-glutamines as potential metabolic imaging agents for tumors. *J. Am. Chem. Soc.* **133,** 1122–33 (2011).

19. Golman, K., in 't Zandt, R. & Thaning, M. Real-time metabolic imaging. *Proc. Natl. Acad. Sci. U. S. A.* **103,** 11270–5 (2006).

20. Salabei, J. K., Gibb, A. A. & Hill, B. G. Comprehensive measurement of respiratory activity in permeabilized cells using extracellular flux analysis. *Nat Protoc* **9,** 421–438 (2014).

21. Ferrick, D. A., Neilson, A. & Beeson, C. Advances in measuring cellular bioenergetics using extracellular flux. *Drug Discov. Today* **13,** 268–274 (2008).

22. Dikalov, S. I. & Harrison, D. G. Methods for Detection of Mitochondrial and Cellular Reactive Oxygen Species. doi:10.1089/ars.2012.4886

23. Zielonka, J., Lambeth, J. D. & Kalyanaraman, B. On the use of L-012, a luminol-based chemiluminescent probe, for detecting superoxide and identifying inhibitors of NADPH oxidase: A re-evaluation. doi:10.1016/j.freeradbiomed.2013.09.017

24. Lee, D. *et al.* In vivo imaging of hydrogen peroxide with chemiluminescent nanoparticles. *Nat. Mater.* **6,** 765–769 (2007).

25. Elas, M., Ichikawa, K. & Halpern, H. J. Oxidative stress imaging in live animals with techniques based on electron paramagnetic resonance. *Radiat. Res.* **177,** 514–23 (2012).

26. Maulucci, G. *et al.* Imaging Reactive Oxygen Species-Induced Modifications in Living Systems. *Antioxid. Redox Signal.* **24,** 939–58 (2016).

27. Wang, X. *et al.* Imaging ROS signaling in cells and animals. *J. Mol. Med. (Berl).* **91,** 917–27 (2013).

28. Hung, Y. P. & Yellen, G. *Live-cell imaging of cytosolic NADH-NAD+ redox state using a genetically encoded fluorescent biosensor*. *Methods in Molecular Biology* **1071,** 83–95 (2014).

29. Hanson, G. T. *et al.* Investigating mitochondrial redox potential with redox-sensitive green fluorescent protein indicators. *J. Biol. Chem.* **279,** 13044–53 (2004).

30. Fang, H. *et al.* Imaging superoxide flash and metabolism-coupled mitochondrial permeability transition in living animals. *Cell Res.* **21,** 1295–304 (2011).

31. Guo, H., Aleyasin, H., Dickinson, B. C., Haskew-Layton, R. E. & Ratan, R. R. Recent

advances in hydrogen peroxide imaging for biological applications. *Cell Biosci.* **4,** 64 (2014).

32. Cameron, W. D. *et al.* Apollo-NADP+: a spectrally tunable family of genetically encoded sensors for NADP+. *Nat. Methods* **13,** 352–358 (2016).

33. Cambronne, X. A. *et al.* Biosensor reveals multiple sources for mitochondrial NAD^+. *Science* **352,** 1474–7 (2016).

34. Mayevsky, A. & Chance, B. Oxidation-reduction states of NADH in vivo: From animals to clinical use. *Mitochondrion* **7,** 330–339 (2007).

35. CHANCE, B., BALTSCHEFFSKY, H. & Baltscheffsky~, H. Respiratory Enzymes in Oxidative Phosphorylation VII. binding of intramitochondrial reduced pyridine nucleotide. *J. Biol. Chem.* **233,** 736–9 (1958).

36. Scott, T. G., Spencer, R. D., Leonard, N. J. & Weber, G. Emission Properties of NADH. Studies of Fluorescence Lifetimes and Quantum Efficiencies of NADH, AcPyADH, and Simplified Synthetic Models'.

37. Ramanujam, N. Fluorescence Spectroscopy of Neoplastic and Non-Neoplastic Tissues. *Neoplasia* **2,** 89–117 (2000).

38. LEENDERS, R., KOOIJMAN, M., HOEK, A., VEEGER, C. & VISSER, A. J. W. G. Flavin dynamics in reduced flavodoxins. A time-resolved polarized fluorescence study. *Eur. J. Biochem.* **211,** 37–45 (1993).

39. Berezin, M. Y. & Achilefu, S. Fluorescence Lifetime Measurements and Biological Imaging. *Chem. Rev* **110,** 2641–2684 (2010).

40. Chorvatova, A. & Chorvat, D. Tissue fluorophores and their spectroscopic characteristics. doi:10.1201/b17018-5

41. Zucker, S. D., Goessling, W., Bootle, E. J. & Sterritt, C. Localization of bilirubin in phospholipid bilayers by parallax analysis of fluorescence quenching. *J. Lipid Res.* **42,** 1377–88 (2001).

42. Heikal, A. A. Intracellular coenzymes as natural biomarkers for metabolic activities and mitochondrial anomalies. *Biomark. Med.* **4,** 241–63 (2010).

43. Georgakoudi, I. & Quinn, K. P. Optical imaging using endogenous contrast to assess metabolic state. *Annu. Rev. Biomed. Eng.* **14,** 351–67 (2012).

44. Bird, D. K. *et al.* Metabolic mapping of MCF10A human breast cells via multiphoton fluorescence lifetime imaging of the coenzyme NADH. *Cancer Res.* **65,** 8766–73 (2005).

45. Boyer, P. D., Theorell, H., Pokras, L., Sillén, L. G. & Thorell, B. The Change in Reduced Diphosphopyridine Nucleotide (DPNH) Fluorescence upon Combination with Liver Alcohol Dehydrogenase (ADH). *Acta Chem. Scand.* **10,** 447–450 (1956).

46. Winer, A. D., Schwert, G. W. & Millar, D. B. S. Lactic Dehydrogenase VI. Fluorimetric Measurements of the complex of enzymes and reduced diphosphopyridine nucleotide. *J Biol Chem* **234,** 1149–1154 (1958).

47. Britton Chance and G. R. Williams. Respiratory Enzymes in Oxidative Phosphorylation. *J Biol Chem* **217,** 409–428 (1955).

48. Chance, B., Cohen, P., Jobsis, F. & Schoener, B. Intracellular Oxidation-Reduction States in Vivo: The microfluorometry of pyridine nucleotide gives a continuous measurement of the oxidation state. *Science (80-.).* **137,** 499–508 (1962).

49. Scholz, R., Thurman, R. G., John, R. & Chance, Britton, Bucher, T. Flavin and Pyridine Nucleotide Oxidation-Reduction Changes in Perfused Rat Liver. *J. BIOLOQICAL Chem.* **244,** 2317–2324 (1969).

50. Rocheleau, J. V., Head, W. S. & Piston, D. W. Quantitative NAD(P)H/Flavoprotein Autofluorescence Imaging Reveals Metabolic Mechanisms of Pancreatic Islet Pyruvate Response. *J. Biol. Chem.* **279,** 31780–31787 (2004).

51. Huang, S., Heikal, A. A. & Webb, W. W. Two-Photon Fluorescence Spectroscopy and Microscopy of NAD(P)H and Flavoprotein. *Biophys. J.* **82,** 2811–2825 (2002).

52. Skala, M. & Ramanujam, N. Multiphoton redox ratio imaging for metabolic monitoring in vivo. *Methods Mol. Biol.* **594,** 155–62 (2010).

53. Quinn, K. P. *et al.* Quantitative metabolic imaging using endogenous fluorescence to detect stem cell differentiation. *Sci. Rep.* **3,** 3432 (2013).

54. Skala, M. C. *et al.* In vivo multiphoton microscopy of NADH and FAD redox states, fluorescence lifetimes, and cellular morphology in precancerous epithelia. *Proc. Natl. Acad. Sci. U. S. A.* **104,** 19494–9 (2007).

55. Lakowicz, J. R., Szmacinski, H., Nowaczyk, K. & Johnson, M. L. Fluorescence lifetime imaging of free and protein-bound NADH. *Proc. Natl. Acad. Sci. U. S. A.* **89,** 1271–5 (1992).

56. Datta, R., Heylman, C., George, S. C. & Gratton, E. Label-free imaging of metabolism and oxidative stress in human induced pluripotent stem cell-derived cardiomyocytes. *Biomed. Opt. Express* **7,** 1690 (2016).

57. Skala, M. C. *et al.* In vivo multiphoton fluorescence lifetime imaging of protein-bound and free nicotinamide adenine dinucleotide in normal and precancerous epithelia. *J. Biomed. Opt.* **12,** 024014

58. Stringari, C., Sierra, R., Donovan, P. J. & Gratton, E. Label-free separation of human embryonic stem cells and their differentiating progenies by phasor fluorescence lifetime microscopy. *J. Biomed. Opt.* **17,** 046012 (2012).

59. Vergen, J. *et al.* Metabolic imaging using two-photon excited NADH intensity and

fluorescence lifetime imaging. *Microsc. Microanal.* **18,** 761–70 (2012).

60. Walsh, A. J. *et al.* Optical metabolic imaging identifies glycolytic levels, subtypes, and early-treatment response in breast cancer. *Cancer Res.* **73,** 6164–74 (2013).

61. Gratton, E. *Measurements of Fluorescence Decay Time by the Frequency Domain Method*. 67–80 (Springer International Publishing, 2016). doi:10.1007/4243

62. Van Munster, E. B., Theodorus, ·., Gadella, W. J. & Gadella, T. W. J. *Fluorescence Lifetime Imaging Microscopy (FLIM)*. 143–175 (Springer Berlin Heidelberg, 2005). doi:10.1007/b102213

63. Lakowicz, J. R. *Frequency-Domain Lifetime Measurements*. *Principles of Fluorescence Spectroscopy* 157–204 (Springer US, 2010). doi:10.1016/0925-4005(96)80051-7

64. Lakowicz, J. R. *Time-Domain Lifetime Measurements*. *Principles of Fluorescence Spectroscopy* **1,** 97–155 (Springer US, 2006).

65. Gratton, E., Breusegem, S., Sutin, J., Ruan, Q. & Barry, N. Fluorescence lifetime imaging for the two-photon microscope: time-domain and frequency-domain methods. *J. Biomed. Opt.* **8,** 381–90 (2003).

66. Ross, J. A. *et al.* Time-resolved methods in biophysics. 8. Frequency domain fluorometry: applications to intrinsic protein fluorescence. *Photochem. Photobiol. Sci.* **7,** 1301 (2008).

67. Becker, W. *et al.* Fluorescence Lifetime Imaging by Time-Correlated Single-Photon Counting. *Microsc. Res. Tech* **63,** 58–66 (2004).

68. Elson, D. *et al.* Time-domain fluorescence lifetime imaging applied to biological tissue. *Photochem. Photobiol. Sci.* **3,** 795 (2004).

69. Minami, T., Kawahigashi, M., Sakai, Y., Shimamoto, K. & Hirayama, S. Fluorescence lifetime measurements under a microscope by the time-correlated single-photon counting technique. *J. Lumin.* **35,** 247–253 (1986).

70. Gaviola, E. Ein Fluorometer. Apparat zur Messung von Fluoreszenzabklingungszeiten. *Zeitschrift für Phys.* **42,** 853–861 (1927).

71. Venetta, B. D. Microscope Phase Fluorometer for Determining the Fluorescence Lifetimes of Fluorochromes. *Cit. Rev. Sci. Instruments J. Chem. Phys. Rev. Sci. Instrum. Rev. Sci. Instrum. 10–9 Sec Rev. Sci. Instrum. J. Chem. Phys* **301,** 24907–841 (1959).

72. Spencer, R. D. & Weber, G. Measurements of Subnanosecond Fluorescence. *Ann. New York Acad. Sci.* **158,** (1969).

73. Peter T C So, Todd E French, Weiming Yu, Keith M Berland, Chen-Yuan Dong, and E. G. in *Fluorescence Imaging Spectroscopy and Microscopy* (ed. Wang, XF and B Herman, B.) 351–374 (John Wiley & Sons, 1996).

74. Colyer, R. A., Lee, C. & Gratton, E. A novel fluorescence lifetime imaging system that optimizes photon efficiency. *Microsc. Res. Tech.* **71,** 201–213 (2008).

75. Lee, C. Y.-C. FLIMBox: A novel fluorescence lifetime approach for the confocal microscope. *ProQuest Diss. Theses; Thesis (Ph.D.)--University California, Irvine, 2007.; Publ. Number AAI3296268; ISBN 9780549411000; Source Diss. Abstr. Int. Vol. 69-01, Sect. B, page 0467.; 113 p.* (2007).

76. Feddersen, B. A., Piston, D. W. & Gratton, E. Digital parallel acquisition in frequency domain fluorimetry. *Rev. Sci. Instrum.* **60,** 2929 (1989).

77. Colyer, R. A., Lee, C. & Gratton, E. A Novel Fluorescence Lifetime Imaging System that Optimizes Photon Efficiency. *Microsc Res Tech* **71,** 201–213 (2008).

78. Gafni, A., Modlin, R. L. & Brand, L. Analysis of fluorescence decay curves by means of the Laplace transformation. *Biophys. J.* **15,** 263–80 (1975).

79. Pelet, S., Previte, M. J. R., Laiho, L. H. & So, P. T. C. A fast global fitting algorithm for fluorescence lifetime imaging microscopy based on image segmentation. *Biophys. J.* **87,** 2807–17 (2004).

80. Siegel, J. *et al.* Application of the stretched exponential function to fluorescence lifetime imaging of biological tissue.

81. Jo, J. A., Fang, Q., Papaioannou, T. & Marcu, L. Fast model-free deconvolution of fluorescence decay for analysis of biological systems. *J. Biomed. Opt.* **9,** 743 (2004).

82. Digman, M. a, Caiolfa, V. R., Zamai, M. & Gratton, E. The phasor approach to fluorescence lifetime imaging analysis. *Biophys. J.* **94,** L14–6 (2008).

83. Digman, M. A. & Gratton, E. The phasor approach to fluorescence lifetime imaging: Exploiting phasor linear properties. doi:10.1

84. Jameson, D. M., Gratton, E. & Hall, R. D. The Measurement and Analysis of Heterogeneous Emissions by Multifrequency Phase and Modulation Fluorometry. *Appl. Spectrosc. Rev.* **20,** 55–106 (1984).

85. Clayton, A. H. A., Hanley, Q. S. & Verveer, P. J. Graphical representation and multicomponent analysis of single-frequency fluorescence lifetime imaging microscopy data. *J. Microsc.* **213,** 1–5 (2004).

86. Redford, G. I. & Clegg, R. M. Polar Plot Representation for Frequency-Domain Analysis of Fluorescence Lifetimes. *J. Fluoresc.* **15,** 805–815 (2005).

87. Stringari, C., Pate, K. T., Edwards, R. a., Waterman, M. L. & Gratton, E. Metabolic Imaging of Colon Cancer Tumors In Vivo by Phasor Fluorescence Lifetime Microscopy of NADH. *Biophys. J.* **104,** 342a–343a (2013).

88. Wright, B. K. *et al.* Phasor-FLIM analysis of NADH distribution and localization in the nucleus of live progenitor myoblast cells. *Microsc. Res. Tech.* **75,** 1717–22 (2012).

89. Stringari, C., Nourse, J. L., Flanagan, L. a & Gratton, E. Phasor fluorescence lifetime microscopy of free and protein-bound NADH reveals neural stem cell differentiation potential. *PLoS One* **7,** e48014 (2012).

90. Stringari, C. *et al.* Phasor approach to fluorescence lifetime microscopy distinguishes different metabolic states of germ cells in a live tissue. *Proc. Natl. Acad. Sci. U. S. A.* **108,** 13582–7 (2011).

91. Sanchez, S., Bakás, L., Gratton, E. & Herlax, V. Alpha Hemolysin Induces an Increase of Erythrocytes Calcium: A FLIM 2-Photon Phasor Analysis Approach. *PLoS One* **6,** e21127 (2011).

92. James, N. G., Ross, J. A., Štefl, M. & Jameson, D. M. Applications of phasor plots to in vitro protein studies. *Anal. Biochem.* **410,** 70–76 (2011).

93. Golfetto, O., Hinde, E. & Gratton, E. Laurdan fluorescence lifetime discriminates cholesterol content from changes in fluidity in living cell membranes. *Biophys. J.* **104,** 1238–47 (2013).

94. Scipioni, L., Gratton, E., Diaspro, A. & Lanzanò, L. Phasor Analysis of Local ICS Detects Heterogeneity in Size and Number of Intracellular Vesicles. *Biophys. J.* **111,** 619–629 (2016).

95. Ranjit, S., Lanzano, L. & Gratton, E. Mapping Diffusion in a Living Cell via the Phasor Approach. *Biophys. J.* **107,** 2775–2785 (2014).

96. Stringari, C. *et al.* Metabolic trajectory of cellular differentiation in small intestine by Phasor Fluorescence Lifetime Microscopy of NADH. *Sci. Rep.* **2,** 568 (2012).

97. Wright, B. K. *et al.* NADH distribution in live progenitor stem cells by phasor-fluorescence lifetime image microscopy. *Biophys. J.* **103,** L7–9 (2012).

98. Stringari, C. *et al.* In Vivo Single-Cell Detection of Metabolic Oscillations in Stem Cells ratio correlates with a higher proportion of stem cells in S phase In Vivo Single-Cell Detection of Metabolic Oscillations in Stem Cells. *CellReports* **10,** 1–7 (2014).

99. Pate, K. T. *et al.* Wnt signaling directs a metabolic program of glycolysis and angiogenesis in colon cancer. *EMBO J.* **33,** 1454–73 (2014).

100. Golfetto, O., Hinde, E. & Gratton, E. in 273–290 (2015). doi:10.1007/978-1-4939-1752-5_19

101. Fereidouni, F., Bader, A. N. & Gerritsen, H. C. Spectral phasor analysis allows rapid and reliable unmixing of fluorescence microscopy spectral images. *Opt. Express* **20,** 12729 (2012).

102. Maritim, a C., Sanders, R. a & Watkins, J. B. Diabetes, oxidative stress, and antioxidants: a review. *J. Biochem. Mol. Toxicol.* **17,** 24–38 (2003).

103. Furukawa, S. *et al.* Increased oxidative stress in obesity and its impact on metabolic

syndrome. *J. Clin. Invest.* **114,** 1752–61 (2004).

104. Matsuzawa-Nagata, N. *et al.* Increased oxidative stress precedes the onset of high-fat diet-induced insulin resistance and obesity. *Metabolism.* **57,** 1071–7 (2008).

105. Reuter, S., Gupta, S. C., Chaturvedi, M. M. & Aggarwal, B. B. Oxidative stress, inflammation, and cancer: how are they linked? *Free Radic. Biol. Med.* **49,** 1603–16 (2010).

106. Dhalla, N. S., Temsah, R. M. & Netticadan, T. Role of oxidative stress in cardiovascular diseases. *J. Hypertens.* **18,** 655–73 (2000).

107. Park, H. S., Kim, S. R. & Lee, Y. C. Impact of oxidative stress on lung diseases. *Respirology* **14,** 27–38 (2009).

108. Uttara, B., Singh, A. V, Zamboni, P. & Mahajan, R. T. Oxidative stress and neurodegenerative diseases: a review of upstream and downstream antioxidant therapeutic options. *Curr. Neuropharmacol.* **7,** 65–74 (2009).

109. Gomes, A., Fernandes, E. & Lima, J. L. F. C. Fluorescence probes used for detection of reactive oxygen species. doi:10.1016/j.jbbm.2005.10.003

110. Krasieva, T. B. *et al.* Two-photon excited fluorescence lifetime imaging and spectroscopy of melanins in vitro and in vivo. *J. Biomed. Opt.* **18,** 31107 (2013).

111. Stringari, C., Cinquin, A., Cinquin, O., Donovan, P. & Gratton, E. In Vivo Identification of Changes in Metabolic State as Stem Cells Differentiate, by Phasor Analysis of Fluorescence Lifetime Imaging. *Biophys. J.* **100,** 183a (2011).

112. Débarre, D. *et al.* Imaging lipid bodies in cells and tissues using third-harmonic generation microscopy. *Nat. Methods* **3,** 47–53 (2006).

113. Nan, X., Cheng, J.-X. & Xie, X. S. Vibrational imaging of lipid droplets in live fibroblast cells with coherent anti-Stokes Raman scattering microscopy. *J. Lipid Res.* **44,** 2202–8 (2003).

114. Krafft, C., Dietzek, B. & Popp, J. Raman and CARS microspectroscopy of cells and tissues. *Analyst* **134,** 1046–57 (2009).

115. Fu, D. *et al.* In vivo metabolic fingerprinting of neutral lipids with hyperspectral stimulated Raman scattering microscopy. *J. Am. Chem. Soc.* **136,** 8820–8 (2014).

116. Yen, K. *et al.* A comparative study of fat storage quantitation in nematode Caenorhabditis elegans using label and label-free methods. *PLoS One* **5,** (2010).

117. Crosignani, V., Jahid, S., Dvornikov, A. S. & Gratton, E. A deep tissue fluorescence imaging system with enhanced SHG detection capabilities. *Microsc. Res. Tech.* **77,** 368–73 (2014).

118. Rohwedder, A., Zhang, Q., Rudge, S. A., Michael, J. O. & Wakelam, M. J. O. Lipid droplet

formation in response to oleic acid in Huh-7 cells is a fatty acid receptor mediated event . Accepted manuscript. *J. Cell Sci.* **127,** 3104–15 (2014).

119. Fujimoto, Y. *et al.* Long-chain fatty acids induce lipid droplet formation in a cultured human hepatocyte in a manner dependent of Acyl-CoA synthetase. *Biol. Pharm. Bull.* **29,** 2174–2180 (2006).

120. Gremmels, H. *et al.* Oleic acid increases mitochondrial reactive oxygen species production and decreases endothelial nitric oxide synthase activity in cultured endothelial cells. *Eur. J. Pharmacol.* (2015). doi:10.1016/j.ejphar.2015.01.005

121. WOJTCZAK, L. & SCHONFELD, P. Effect of fatty acids on energy coupling processes in mitochondria. *Biochim. Biophys. Acta - Bioenerg.* **1183,** 41–57 (1993).

122. Meierjohann, S. Oxidative stress in melanocyte senescence and melanoma transformation. *European Journal of Cell Biology* **93,** 36–41 (2014).

123. Venza, M. *et al.* Cellular Mechanisms of Oxidative Stress and Action in Melanoma. *Oxidative Medicine and Cellular Longevity* **2015,** 481782 (2015).

124. Fruehauf, J. P. & Trapp, V. Reactive oxygen species: an Achilles' heel of melanoma? *Expert Rev. Anticancer Ther.* **8,** 1751–1757 (2008).

125. Booher, K., Lin, D.-W., Borrego, S. L. & Kaiser, P. Downregulation of Cdc6 and pre-replication complexes in response to methionine stress in breast cancer cells. *Cell Cycle* **11,** 4414–23 (2012).

126. Borrego, S. L. *et al.* Metabolic changes associated with methionine stress sensitivity in MDA-MB-468 breast cancer cells. *Cancer Metab.* **4,** 9 (2016).

127. Dillard, C. J. & Tappel, A. L. in *Methods in Enzymology* **Volume 105,** 337–341 (1984).

128. Matthäus, C. *et al.* Noninvasive imaging of intracellular lipid metabolism in macrophages by Raman microscopy in combination with stable isotopic labeling. *Anal. Chem.* **84,** 8549–56 (2012).

129. Lambert, J. *Introduction to organic spectroscopy*. (Macmillan, 1987).

130. Katz, M., Eldred, G. & Jr, W. R. Lipofuscin autofluorescence: evidence for vitamin A involvement in the retina. *Mech. Ageing Dev.* **39,** (1987).

131. Sitte, N., Merker, K., Grune, T. & von Zglinicki, T. Lipofuscin accumulation in proliferating fibroblasts in vitro: an indicator of oxidative stress. *Exp. Gerontol.* **36,** 475–86 (2001).

132. Schweitzer, D. *et al.* Time-resolved autofluorescence imaging of human donor retina tissue from donors with significant extramacular drusen. *Invest. Ophthalmol. Vis. Sci.* **53,** 3376–86 (2012).

133. Orban, T., Palczewska, G. & Palczewski, K. Retinyl ester storage particles (retinosomes)

from the retinal pigmented epithelium resemble lipid droplets in other tissues. *J. Biol. Chem.* **286,** 17248–58 (2011).

134. Blaner, W. S. *et al.* Hepatic stellate cell lipid droplets: a specialized lipid droplet for retinoid storage. *Biochim. Biophys. Acta* **1791,** 467–73 (2009).

135. Failloux, N., Bonnet, I., Baron, M.-H. & Perrier, E. Quantitative Analysis of Vitamin A Degradation by Raman Spectroscopy. *Appl. Spectrosc.* **57,** 1117–1122 (2003).

136. Colombo, A., Cipolla, C., Beggiato, M. & Cardinale, D. Cardiac toxicity of anticancer agents. *Curr. Cardiol. Rep.* **15,** 362 (2013).

137. Heylman, C., Sobrino, A., Shirure, V. S., Hughes, C. C. & George, S. C. A strategy for integrating essential three-dimensional microphysiological systems of human organs for realistic anticancer drug screening. *Exp. Biol. Med. (Maywood).* **239,** 1240–54 (2014).

138. Albini, A. *et al.* Cardiotoxicity of anticancer drugs: the need for cardio-oncology and cardio-oncological prevention. *J. Natl. Cancer Inst.* **102,** 14–25 (2010).

139. Mordwinkin, N. M., Burridge, P. W. & Wu, J. C. A review of human pluripotent stem cell-derived cardiomyocytes for high-throughput drug discovery, cardiotoxicity screening, and publication standards. *J. Cardiovasc. Transl. Res.* **6,** 22–30 (2013).

140. Zeevi-Levin, N., Itskovitz-Eldor, J. & Binah, O. Cardiomyocytes derived from human pluripotent stem cells for drug screening. *Pharmacol. Ther.* **134,** 180–8 (2012).

141. Hafstad, A. D., Nabeebaccus, A. A. & Shah, A. M. Novel aspects of ROS signalling in heart failure. *Basic Res. Cardiol.* **108,** 359 (2013).

142. Burgoyne, J. R., Mongue-Din, H., Eaton, P. & Shah, A. M. Redox signaling in cardiac physiology and pathology. *Circ. Res.* **111,** 1091–106 (2012).

143. Walsh, A. J., Cook, R. S., Arteaga, C. L. & Skala, M. C. Optical metabolic imaging of live tissue cultures. **8588,** 858820–858820–6 (2013).

144. Vergen, J. *et al.* Metabolic imaging using two-photon excited NADH intensity and fluorescence lifetime imaging. *Microsc. Microanal.* **18,** 761–70 (2012).

145. Ghukasyan, V. V. & Kao, F.-J. Monitoring Cellular Metabolism with Fluorescence Lifetime of Reduced Nicotinamide Adenine Dinucleotide †. *J. Phys. Chem. C* **113,** 11532–11540 (2009).

146. Bird, D. K. *et al.* Metabolic mapping of MCF10A human breast cells via multiphoton fluorescence lifetime imaging of the coenzyme NADH. *Cancer Res.* **65,** 8766–73 (2005).

147. Duranteau, J. Intracellular Signaling by Reactive Oxygen Species during Hypoxia in Cardiomyocytes. *J. Biol. Chem.* **273,** 11619–11624 (1998).

148. Vanden Hoek, T. L., Becker, L. B., Shao, Z., Li, C. & Schumacker, P. T. Reactive Oxygen

Species Released from Mitochondria during Brief Hypoxia Induce Preconditioning in Cardiomyocytes. *J. Biol. Chem.* **273,** 18092–18098 (1998).

149. Semenza, G. L. Hypoxia-inducible factor 1 and cardiovascular disease. *Annu. Rev. Physiol.* **76,** 39–56 (2014).

150. Wang, M. C., Min, W., Freudiger, C. W., Ruvkun, G. & Xie, X. S. RNAi screening for fat regulatory genes with SRS microscopy. *Nat. Methods* **8,** 135–8 (2011).

151. Varga, Z. V, Ferdinandy, P., Liaudet, L. & Pacher, P. Drug-induced mitochondrial dysfunction and cardiotoxicity. *Am. J. Physiol. - Hear. Circ. Physiol.* **309,** ajpheart.00554.2015 (2015).

152. Deavall, D. G., Martin, E. a., Horner, J. M. & Roberts, R. Drug-Induced Oxidative Stress and Toxicity. *J. Toxicol.* **2012,** 1–13 (2012).

153. Alfonso-García, A., Pfisterer, S. G., Riezman, H., Ikonen, E. & Potma, E. O. D38-cholesterol as a Raman active probe for imaging intracellular cholesterol storage. *J. Biomed. Opt.* **21,** 61003 (2016).

154. Okita, K. *et al.* A more efficient method to generate integration-free human iPS cells. *Nat. Methods* **8,** 409–412 (2011).

155. Lian, X. *et al.* Directed cardiomyocyte differentiation from human pluripotent stem cells by modulating Wnt/β-catenin signaling under fully defined conditions. *Nat. Protoc.* **8,** 162–75 (2013).

156. O'Rourke, B., Cortassa, S. & Aon, M. A. Mitochondrial ion channels: gatekeepers of life and death. *Physiology (Bethesda).* **20,** 303–15 (2005).

157. Griffiths, E. J., Lin, H. & Suleiman, M. S. NADH Fluorescence in Isolated Guinea-Pig and Rat Cardiomyocytes Exposed to Low or High Stimulation Rates and Effect of Metabolic Inhibition with Cyanide. *Biochem. Pharmacol.* **56,** 173–179 (1998).

158. Giordano, F. J. Oxygen, oxidative stress, hypoxia, and heart failure. *J. Clin. Invest.* **115,** 500–508 (2005).

159. Vishwasrao, H. D., Heikal, A. a., Kasischke, K. a. & Webb, W. W. Conformational dependence of intracellular NADH on metabolic state revealed by associated fluorescence anisotropy. *J. Biol. Chem.* **280,** 25119–25126 (2005).

160. Ryter, S. W. *et al.* Mechanisms of cell death in oxidative stress. *Antioxid. Redox Signal.* **9,** 49–89 (2007).

161. Zhou, X., Zhai, X. & Ashraf, M. Direct evidence that initial oxidative stress triggered by preconditioning contributes to second window of protection by endogenous antioxidant enzyme in myocytes. *Circulation* **93,** 1177–84 (1996).

162. Wikswo, J. P. The relevance and potential roles of microphysiological systems in biology and medicine. *Exp. Biol. Med. (Maywood).* **239,** 1061–72 (2014).

163. Sobrino, A. *et al.* 3D microtumors in vitro supported by perfused vascular networks. *Sci. Rep.* **6,** 31589 (2016).

164. Moya, M., Tran, D. & George, S. C. An integrated in vitro model of perfused tumor and cardiac tissue. **4,** 1–6 (2013).

165. Ebert, S., Travis, K., Lincoln, B. & Guck, J. Fluorescence ratio thermometry in a microfluidic dual-beam laser trap. *Opt. Express* **15,** 15493 (2007).

166. Schaerli, Y. *et al.* Continuous-flow polymerase chain reaction of single-copy DNA in microfluidic microdroplets. *Anal. Chem.* **81,** 302–6 (2009).

167. Matthews, S. M. *et al.* Quantitative kinetic analysis in a microfluidic device using frequency-domain fluorescence lifetime imaging. *Anal. Chem.* **79,** 4101–9 (2007).

168. Magennis, S. W., Graham, E. M. & Jones, A. C. Quantitative Spatial Mapping of Mixing in Microfluidic Systems. *Angew. Chemie Int. Ed.* **44,** 6512–6516 (2005).

169. Elder, A. D. *et al.* The application of frequency-domain Fluorescence Lifetime Imaging Microscopy as a quantitative analytical tool for microfluidic devices. *Opt. Express* **14,** 5456 (2006).

170. Robinson, T. *et al.* Three-dimensional molecular mapping in a microfluidic mixing device using fluorescence lifetime imaging. *Opt. Lett.* **33,** 1887 (2008).

171. Benninger, R. K. P. *et al.* Time-resolved fluorescence imaging of solvent interactions in microfluidic devices. *Opt. Express* **13,** 6275 (2005).

172. Benninger, R. K. P. *et al.* Fluorescence-Lifetime Imaging of DNA–Dye Interactions within Continuous-Flow Microfluidic Systems. *Angew. Chemie Int. Ed.* **46,** 2228–2231 (2007).

173. Sun, M. Y. *et al.* Autofluorescence Imaging of Living Pancreatic Islets Reveals Fibroblast Growth Factor-21 (FGF21)-Induced Metabolism. *Biophys. J.* **103,** 2379–2388 (2012).

174. Rocheleau, J. V. & Piston, D. W. Chapter 4 Combining Microfluidics and Quantitative Fluorescence Microscopy to Examine Pancreatic Islet Molecular Physiology. *Methods Cell Biol.* **89,** 71–92 (2008).

175. Peters, K. *et al.* Changes in human endothelial cell energy metabolic capacities during in vitro cultivation. the role of aerobic glycolysis and proliferation. *Cell. Physiol. Biochem.* **24,** 483–492 (2009).

176. Harjes, U., Bensaad, K. & Harris, A. Endothelial cell metabolism and implications for cancer therapy. *Br. J. Cancer* **107,** 1207–1212 (2012).

177. Wang, H.-W. *et al.* Differentiation of apoptosis from necrosis by dynamic changes of reduced nicotinamide adenine dinucleotide fluorescence lifetime in live cells. *J. Biomed. Opt.* **13,** 054011 (2008).

178. Hanahan, D. & Weinberg, R. A. Hallmarks of cancer: The next generation. *Cell* **144,** 646–674 (2011).

179. Ganapathy-Kanniappan, S. & Geschwind, J.-F. H. Tumor glycolysis as a target for cancer therapy: progress and prospects. *Mol. Cancer* **12,** 152 (2013).

180. Bost, F., Decoux-Poullot, A.-G., Tanti, J. F. & Clavel, S. Energy disruptors: rising stars in anticancer therapy[quest]. *Nat. Publ. Gr.* **4,** e183– (2016).

181. Nuermberger, E. L. & Bishai, W. R. Antibiotic resistance in Streptococcus pneumoniae: what does the future hold? *Clin. Infect. Dis.* **38 Suppl 4,** S363–S371 (2004).

182. Nikaido, H. Multidrug Resistance in Bacteria. (2009). doi:10.1146/annurev.biochem.78.082907.145923

183. Smith, P. A. & Romesberg, F. E. Combating bacteria and drug resistance by inhibiting mechanisms of persistence and adaptation. *Nat. Chem. Biol.* **3,** 549–56 (2007).

184. Shah, D. *et al.* Persisters: a distinct physiological state of E. coli. doi:10.1186/1471-2180-6-53

185. Dhar, N. & Mckinney, J. D. Microbial phenotypic heterogeneity and antibiotic tolerance. doi:10.1016/j.mib.2006.12.007

186. Ammor, M. S. Recent Advances in the Use of Intrinsic Fluorescence for Bacterial Identification and Characterization. (2007). doi:10.1007/s10895-007-0180-6

187. Estes, C. *et al.* Reagentless detection of microorganisms by intrinsic fluorescence. *Biosens. Bioelectron.* **18,** 511–519 (2003).

188. Tourkya, B., Boubellouta, T., Dufour, E. & Leriche, F. Fluorescence spectroscopy as a promising tool for a polyphasic approach to pseudomonad taxonomy. *Curr. Microbiol.* **58,** 39–46 (2009).

189. Dartnell, L. R., Roberts, T. A., Moore, G., Ward, J. M. & Muller, J.-P. Fluorescence Characterization of Clinically-Important Bacteria. *PLoS One* **8,** (2013).

190. Sullivan, N. L., Tzeranis, D. S., Wang, Y., So, P. T. C. & Newman, D. Quantifying the dynamics of bacterial secondary metabolites by spectral multiphoton microscopy. *ACS Chem. Biol.* **6,** 893–899 (2011).

191. Ammor, S., Yaakoubi, K., Chevallier, I. & Dufour, E. Identification by fluorescence spectroscopy of lactic acid bacteria isolated from a small-scale facility producing traditional dry sausages. *J. Microbiol. Methods* **59,** 271–281 (2004).

192. Leblanc, L. & Dufour, E. Monitoring the identity of bacteria using their intrinsic fluorescence. *FEMS Microbiol. Lett.* **211,** 147–153 (2002).

193. Giana, H. E., Silveira, L., Zângaro, R. A., Tadeu, M. & Pacheco, T. Rapid Identification of Bacterial Species by Fluorescence Spectroscopy and Classification Through Principal

Components Analysis. *J. Fluoresc.* **13,** (2003).

194. Alimova, A. *et al.* Native fluorescence and excitation spectroscopic changes in Bacillus subtilis and Staphylococcus aureus bacteria subjected to conditions of starvation. *Appl. Opt.* **42,** 4080 (2003).

195. Duysens, L. N. M. & Amesz, J. Fluorescence spectrophotometry of reduced phosphopyridine nucleotide in intact cells in the near-ultraviolet and visible region. *Biochim. Biophys. Acta* **24,** 19–26 (1957).

196. Rao, G. & Mutharasan, R. Applied Microbiology Biotechnology NADH levels and solventogenesis in Clostridium acetobutylicum: new insights through culture fluorescence. *Appl Microbiol Biotechnol* **30,** 59–66 (1989).

197. Harrison, D. E. F. Undamped oscillations of pyridine nucleotide and oxygen tension in chemostat cultures of klebsiella aerogenes. *J. Cell Biol.* **45,** 514–521 (1970).

198. Wimpenny, J. W. T. & Firth, A. Levels of Nicotinamide Adenine Dinucleotide and Reduced Nicotinamide Adenine Dinucleotide in Facultative Bacteria and the Effect of Oxygen. *J. BACTROLOGY* **111,** 24–32 (1972).

199. Wos, M. & Pollard, P. Sensitive and meaningful measures of bacterial metabolic activity using NADH fluorescence. *Water Res.* **40,** 2084–2092 (2006).

200. Wos, M. L. & Pollard, P. C. Cellular nicotinamide adenine dinucleotide (NADH) as an indicator of bacterial metabolic activity dynamics in activated sludge. *Water Sci. Technol.* **60,** 783–791 (2009).

201. Armiger, W. B. & Schwegler, B. R. Control of bnr processes by regulation of the VFA/M ratio. *Sci. Tech* **28,** 303–314 (1993).

202. Dalterio, R. A. *et al.* The Steady-State and Decay Characteristics of Primary Fluorescence From Live Bacteria. *Appl. Spectrosc.* **41,** 234–241 (1987).

203. Brahma, S. K. *et al.* The Rapid Identification of Bacteria Using Time-Resolved Fluorescence and Fluorescence Excitation Spectral Methods. *Appl. Spectrosc.* **39,** 869–872 (1985).

204. Dalterio, R. A. *et al.* Steady-State and Decay Characteristics of Protein Tryptophan Fluorescence from Bacteria. *Appl. Spectrosc.* **40,** 86–90 (1986).

205. Awad, F., Ramprasath, C., Mathivanan, N., Aruna, P. R. & Ganesan, S. Steady-state and fluorescence lifetime spectroscopy for identification and classification of bacterial pathogens. *Biomed. Spectrosc. Imaging* **3,** 381–391 (2014).

206. Awad, F. *et al.* Optical Fiber-Based Steady State and Fluorescence Lifetime Spectroscopy for Rapid Identification and Classification of Bacterial Pathogens Directly from Colonies on Agar Plates. *Int. Sch. Res. Not.* **2014,** 1–7 (2014).

207. Alfonso-García, A. *et al.* Label-free identification of macrophage phenotype by

fluorescence lifetime imaging microscopy. *J. Biomed. Opt.* **21,** 046005 (2016).

208. Torno, K. *et al.* Real-time analysis of metabolic activity within lactobacillus acidophilus by phasor fluorescence lifetime imaging microscopy of NADH. *Curr. Microbiol.* **66,** 365–367 (2013).

209. Chubukov, V., Gerosa, L., Kochanowski, K. & Sauer, U. Coordination of microbial metabolism. *Nat. Publ. Gr.* **12,** (2014).

210. Jurtshuk, P. *Bacterial Metabolism*. *Medical Microbiology* (University of Texas Medical Branch at Galveston, 1996).

211. Ouzounis, C. A. & Karp, P. D. Global properties of the metabolic map of Escherichia coli. *Genome Res.* **10,** 568–576 (2000).

212. London, J. & Knight, A. M. Concentrations of Nicotinamide Nucleotide Coenzymes in Micro-Organisms. *J. gen. Microb.* **44,** 241–254 (1966).

213. de Graef, M. R., Alexeeva, S., Snoep, J. L. & Teixeira de Mattos, M. J. The steady-state internal redox state (NADH/NAD) reflects the external redox state and is correlated with catabolic adaptation in Escherichia coli. *J. Bacteriol.* **181,** 2351–7 (1999).

214. Lobritz, M. A. *et al.* Antibiotic efficacy is linked to bacterial cellular respiration. *Proc. Natl. Acad. Sci.* **112,** 8173–8180 (2015).

215. Poole, K. Bacterial stress responses as determinants of antimicrobial resistance. *J. Antimicrob. Chemother.* dks196 (2012). doi:10.1093/jac/dks196

216. Blair, J. M. A., Webber, M. A., Baylay, A. J., Ogbolu, D. O. & Piddock, L. J. V. Molecular mechanisms of antibiotic resistance. *Nat. Rev. Microbiol.* **13,** 42–51 (2015).

217. Lobritz, M. A. *et al.* Antibiotic efficacy is linked to bacterial cellular respiration. *Proc. Natl. Acad. Sci.* **112,** 8173–8180 (2015).

218. Orman, M. A. & Brynildsen, M. P. Dormancy Is Not Necessary or Sufficient for Bacterial Persistence. *Antimicrob. Agents Chemother.* **57,** 3230–3239 (2013).

219. Pankey, G. A. & Sabath, L. D. Clinical Relevance of Bacteriostatic versus Bactericidal Mechanisms of Action in the Treatment of Gram-Positive Bacterial Infections. *Clin. Infect. Dis.* **38,** 864–870 (2004).

220. Pletnev, P., Osterman, I., Sergiev, P., Bogdanov, A. & Dontsova, O. Survival guide: Escherichia coli in the stationary phase. *Acta Naturae* **7,** 22–33 (2015).

221. Zwietering, M. H., Jongenburger, I., Rombouts, F. M., Van ' A. K. & Riet, T. Modeling of the Bacterial Growth Curve. *Appl. Environ. Microbiol.* 1875–1881 (1990).

222. Monod, J. The Growth of Bacterial Cultures. *Annu. Rev. Microbiol.* **3,** 371–394 (1949).

223. Widdel, F. Theory and Measurement of Bacterial Growth A. Basic and practical aspects.

224. Navarro Llorens, J. M., Tormo, A. & Martínez-García, E. Stationary phase in gram-negative bacteria. *FEMS Microbiol. Rev.* **34,** 476–495 (2010).

225. Zambrano, M. M. & Kolter, R. GASPing for Life in Stationary Phase. *Cell* **86,** 181–184 (1996).

226. Bacun-Druzina, V., Cagalj, Z. & Gjuracic, K. The growth advantage in stationary-phase (GASP) phenomenon in mixed cultures of enterobacteria. (2006). doi:10.1111/j.1574-6968.2006.00515.x

227. Farrell, M. J. & Finkel, S. E. The Growth Advantage in Stationary-Phase Phenotype Conferred by rpoS Mutations Is Dependent on the pH and Nutrient Environment. *J. Bacteriol.* **185,** 7044–7052 (2003).

228. Aichler, M. & Walch, A. MALDI Imaging mass spectrometry: current frontiers and perspectives in pathology research and practice. *Lab. Investig.* **95,** 422–431 (2015).

229. Wang, X. *et al.* An on-chip microfluidic pressure regulator that facilitates reproducible loading of cells and hydrogels into microphysiological system platforms. *Lab Chip* **16,** 868–876 (2016).

230. Huh, D., Hamilton, G. A. & Ingber, D. E. From 3D cell culture to organs-on-chips. *Trends Cell Biol.* **21,** 745–754 (2011).

231. Flemming, H.-C. *et al.* Biofilms: an emergent form of bacterial life. *Nat. Publ. Gr.* **14,** (2016).

232. Costerton, J. W., Montanaro, L. & Arciola, C. R. Biofilm in implant infections: its production and regulation. *Int. J. Artif. Organs* **28,** 1062–8 (2005).